POLYMER SURFACES ON SMALL LENGTH- AND SHORT TIME-SCALES

DISSERTATION

zur Erlangung des Grades

„Doktor der Naturwissenschaften"

am Fachbereich Chemie, Pharmazie und Geowissenschaften

der Johannes-Gutenberg-Universität in Mainz

vorgelegt von

Franz Albert Giselher <u>Tassilo</u> Kaule

geboren in Stuttgart

Mainz, den 15. Oktober 2012

Die vorliegende Arbeit wurde in der Zeit von Juni 2009 bis Oktober 2012 unter der Betreuung von Dr. Rüdiger Berger und Prof. Dr. Hans-Jürgen Butt am Max-Planck-Institut für Polymerforschung in Mainz durchgeführt.

Tag der mündlichen Prüfung: 14.11.2012

Dekan: Prof. Dr. D.Sc. h.c. Wolfgang Hofmeister

1. Berichterstatter: Prof. Dr. H.-J. Butt
2. Berichterstatter: Prof. Dr. A. Kühnle

Zusammenfassung

Das Verhalten von Polymeren hängt von der Längenskala und Zeitskala, auf der sie untersucht werden, sowie der Temperatur, bei der die Untersuchung stattfindet, ab. Diese Arbeit beschreibt meine Untersuchungen von Polymeroberflächen mittels Rasterkraftmikroskopie mit heizbaren Spitzen. Mit diesen Spitzen kann man Oberflächen im Bereich von Quadrat-Nanometern innerhalb von Sekunden bis zu Mikrosekunden aufheizen. Ich stelle Experimente zur lokalen Bestimmung von Glasübergangs- und Schmelztemperaturen vor. Im Gegensatz zur gängigen Meinung, dass nur dicke Polymerfilme untersucht werden können, stelle ich eine neue Methode vor, die es ermöglicht auch Filme mit Dicken unter 100 nm zu untersuchen. Hierzu wurde zuerst eine Hintergrundmessung auf dem Substrat durchgeführt, die dann von der Messung auf der Polymerprobe abgezogen wurde. Die differentiellen Messungen von Polystyrolfilmen mit Dicken zwischen 35 nm und 160 nm zeigten charakteristische Signale bei 95 ± 1 °C was in Übereinstimmung mit der Glasübergangstemperatur von Polystyrol ist. Drückt man geheizte Spitzen in Polymerfilme, so kommt es zu plastischer Deformation. Solche nanometer-großen Deformationen werden in neuen Konzepten zur hochdichten Datenspeicherung verwendet. Ein geeignetes Speichermedium für diese Systeme muss sich leicht eindrücken lassen, also weich sein, gleichzeitig aber auch langzeitstabil, also hart sein. Zur Entwicklung eines solchen Speichermediums wurde hier ein neuer Ansatz untersucht: Vergleichsweise weiches Polystryrol wurde mit einer dünnen, aber sehr harten Schicht bestehend aus plasma-polymerisiertem Norbornen geschützt. Die erhaltenen zweischichtigen Filme wurden dann hinsichtlich ihrer Stabilität gegenüber Oberflächenabnutzung und ihrer Verformbarkeit untersucht. Es konnte gezeigt werden, dass die zweischichtigen Systeme die stabile Oberfläche des Plasmapolymers mit der leichten Verformbarkeit des Polystyrols verbinden und deswegen sehr gute Speichermedien darstellen. Außerdem wurde die Glasübergangstemperatur der Filme auf einer Zeitskala von 10 µs gemessen und ein Wert von ca. 220 °C bestimmt. Die Erhöhung dieser für das Polymer charakteristischen Temperatur ist ein Resultat der kurzen Zeitskala mit der das Polymer untersucht wird und spiegelt das Zeit-Temperatur-Superpositionsprinzip wider.

Heizbare Spitzen wurden auch zur Charakterisierung von mit Silberazid gefüllten Nanokapseln verwendet. Diese Methode erlaubte es mit einer Substanzmenge von wenigen Nanogramm die Zersetzungstemperatur der Nanokapseln zwischen 180°C und 225°C zu bestimmen, was in guter Übereinstimmung mit der Literatur ist. Die Untersuchung von kleinen Mengen war notwendig, da nur wenig Material zur Verfügung stand. Bei Verwendung größerer Mengen könnte das entstehende Silber zur Kontamination oder sogar zur Beschädigung der Messinstrumente führen. Neben der Bestimmung von temperaturabhängigen Materialparametern habe ich heizbare Spitzen zur gezielten thermischen Zersetzung von Pentacen-Precursoren eingesetzt. Ziel war es nanoskopische leitfähige Strukturen zu erzeugen. Hierbei ist die Schichtdicke des Precursor-Materials entscheidend für eine vollständige thermische Umsetzung.

Ein weiterer Schwerpunkt war die Untersuchung von redox-aktiven Polymerfilmen - Poly-10-(4-vinylbenzyl)-10H-phenothiazin (PVBPT) - zur Datenspeicherung. Hierbei wurde lokal die elektrische Leitfähigkeit durch Anlegen einer Spannung zwischen Spitze und Oberfläche verändert. Die so erzeugten Strukturen waren langzeitstabil (> 16 h). Es konnte gezeigt werden, dass die Anwesenheit von Wasser essentiel für das elektrische Oxidieren von PVBPT war.

Abstract

The behaviour of a polymer depends strongly on the length- and time scale as well as on the temperature at which it is probed. In this work, I describe investigations of polymer surfaces using scanning probe microscopy with heatable probes. With these probes, surfaces can be heated within seconds down to microseconds. I introduce experiments for the local and fast determination of glass transition and melting temperatures. I developed a method which allows the determination of glass transition and melting temperatures on films with thicknesses below 100 nm: A background measurement on the substrate was performed. The resulting curve was subtracted from the measurement on the polymer film. The differential measurement on polystyrene films with thicknesses between 35 nm and 160 nm showed characteristic signals at 95 ± 1 °C, in accordance with the glass transition of polystyrene. Pressing heated probes into polymer films causes plastic deformation. Nanometer sized deformations are currently investigated in novel concepts for high density data storage. A suitable medium for such a storage system has to be easily indentable on one hand, but on the other hand it also has to be very stable towards surface induced wear. For developing such a medium I investigated a new approach: A comparably soft material, namely polystyrene, was protected with a thin but very hard layer made of plasma polymerized norbornene. The resulting bilayered media were tested for surface stability and deformability. I showed that the bilayered material combines the deformability of polystyrene with the surface stability of the plasma polymer, and that the material therefore is a very good storage medium. In addition we investigated the glass transition temperature of polystyrene at timescales of 10 μs and found it to be approx. 220 °C. The increase of this characteristic temperature of the polymer results from the short time at which the polymer was probed and reflects the well-known time-temperature superposition principle.

Heatable probes were also used for the characterization of silverazide filled nanocapsules. The use of heatable probes allowed determining the decomposition temperature of the capsules from few nanograms of material. The measured decomposition temperatures ranged from 180 °C to 225 °C, in accordance with literature values. The investigation of small amounts of sample was necessary due to the limited availability of the material. Furthermore, investigating larger amounts of the capsules using conventional thermal gravimetric analysis could lead to contamination or even damage of the instrument. Besides the analysis of material parameters I used the heatable probes for the local thermal decomposition of pentacene precursor material in order to form nanoscale conductive structures. Here, the thickness of the precursor layer was important for complete thermal decomposition.

Another aspect of my work was the investigation of redox active polymers - Poly-10-(4-vinylbenzyl)-10H-phenothiazine (PVBPT)- for data storage. Data is stored by changing the local conductivity of the material by applying a voltage between tip and surface. The generated structures were stable for more than 16 h. It was shown that the presence of water is essential for succesfull patterning.

Table of content

1.   Motivation

"It is my feeling that Time ripens all things; with Time all things are revealed; Time is the father of truth." (Francois Rabelais).

As already stated by Francois Rabelais (*1494 – †1553), a major French renaissance writer, doctor, humanist and scholar, time is an important parameter "to reveal things". Furthermore, the observed "truth" often depends strongly on time. The time dependence of experienced truth is well-known from daily life. For example, entering a swimming pool is an easy to do experiment to reveal the importance of timescales.
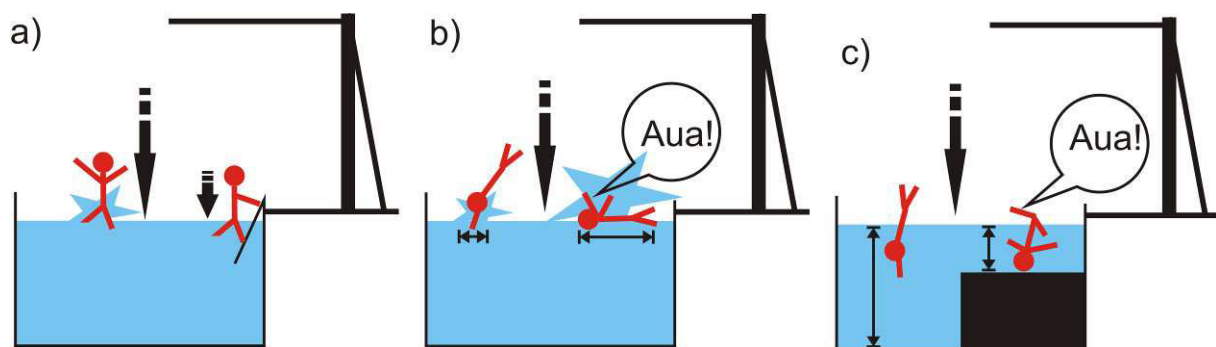
Figure 1: Importance of different time- and length scales on the interactions between a human body and a water filled swimming pool: a) "Hardness" of water and amount of water splashed depend on the time scale of entering. b) Size of water splash depends on the length scale of the contact are between human and water surface upon entering. c) The felt properties on entering depend on the length scale of depth of water.

Upon entering a pool slowly, the water has all time necessary to rearrange by flowing around the body, so one feels a very soft medium (Figure 1a, right). Upon jumping from a 10 m diving board, i.e. entering the pool very fast, the water does not have enough time to rearrange in a similar way, so one feels a harder medium (Figure 1a, left). Taking the size of the water splash caused by the body's impact as a measure reveals that the amount of splashed water scales not only with the timescale, but also with the length scale, i.e. the contact area between body and water surface and the technique of entering (Figure 1b). A sporty header will cause a much smaller splash than a less elegant belly flopper (Figure 1b). The water splash is caused by two different mechanisms. The primary mechanism is the displacement of water by the entering body. The primary splash scales with the contact area between body and water. In Olympic diving, the athletes minimize this splash by entering the water with minimal contact area, thus hands first and body stretched out. The other

mechanism causing the secondary splash is the void in the water caused by the diver who drags air with him into the water. When the walls of this void collapse, the water enters violently in the void and is catapulted out in the air. Another effect which has to be considered is cavitation at the fast entering body can cause water to evaporate due to the sudden change in pressure. This collapse of the formed cavities then causes the splash. This secondary splash scales with the time-scale i.e. with the speed at which the diver enters the water and with the depth he dives into the water. Higher speeds and higher reached depth cause a bigger splash. In order to reduce the secondary splash, athletes open their arms immediately after entering the water and roll their body to the side. Thus, they reduce their speed and the depth they reach. Furthermore, the opening of the arms destroys the walls of the formed void and allows gentler entering of water.

The simple entering of a swimming pool shows that the properties of a material have to be probed at different timescales for a complete understanding. Results from one specific timescale will not be reproducible at other timescales. In fact, the well-known time-temperature superposition principle describes shifts in experimental results when changing the timescale.

The same is true for changes in length scales. Although for a wide range of macroscopic length scales the same mechanisms and principles can be applied, the behavior of a material may change when the length scale is reduced to the nanometer regime or below. When changing the length scale of an experiment to length scales of few nanometers and below, we change the amount of sample probed down to few or even single molecules. Not only is the length scale in lateral direction of importance, but also the length scale in vertical direction. The importance of the vertical length scale can again be demonstrated by diving into a swimming pool. Upon jumping into a deep pool, one feels only the properties of water, whereas jumping into a very shallow pool will reveal that one now probes the properties of the pools ground (Figure 1d). In the same way, when the thickness of a sample is reduced to few nanometers, the substrate will have a different influence on the measurement than for samples with thicknesses of several µm.

I investigated the influence of time- and length-scale effects by studying thin polymeric films with scanning probe microscopy (SPM). SPM has become a standard technique for surface investigations since its invention in 1986 [1] and is introduced in detail in **chapter 2**. In all SPM techniques, a surface is probed with an ultra-sharp tip mounted at the end of a cantilever. Interactions between this tip and the sample surface lead to changes in the cantilevers deflection. In order to study the thermo-mechanical behavior of thin films, I used heatable SPM probes. These probes have a heater element integrated in the cantilever which is used to heat the tip.

Heatable probes can be used to analyze surfaces on the 10 nm length scale of their radius. Softening, melting or glass transition temperatures can be determined locally with a resolution in the range of the probe size [2]. In **chapter 4**, I discuss a method which is based on measuring the probes deflection upon heating. When the probe temperature exceeds the softening, melting or glass transition temperature of the sample, the probe sinks into the sample which is detected as a change of deflection. I will refer to this method as nano-thermal analysis (nTA). Investigating films with thicknesses of several 100 nm using nTA works well, but for films with thicknesses of only several 10 nm nTA investigations often fail or show results differing from the results on thicker films. Two effects have to be considered: First, when a film becomes thinner and thinner, we start to probe the properties of the substrate instead of the film properties. Second, due to the much better heat conductivity of silicon or gold substrates compared to the heat conductivity of the polymeric materials under investigation, the substrate provides an effective heat sink. The question is therefore whether it is possible to extract softening, melting or glass transition temperatures of thin films from heatable probe experiments.

In **chapter 4** I investigated two approaches to gain information about the glass transition temperature of thin polymer films. First, I improved the literature known approach by subtracting deflection curves recorded on the substrate from the deflection curves recoded on thin films, thus removing the substrate's and the cantilever's influence on the measured deflection. Second, I used changes in the adhesion between probe and sample surface instead of changes in the deflection of the probe in order to determine softening, melting or glass transition temperatures. Heatable probes can be used to modify the topography of a polymeric surface [3-6].

However, a heatable probe should be able to thermally initiate chemical reactions on the small length scale of the probe. I investigated the use of locally initiated chemical reactions for the formation of elevated structures in **chapter 5**. A precursor material should react locally from a good soluble precursor into a less soluble product. I focused on an organic precursor material which formed an organic conductor upon thermal decomposition. By consecutive washing with a solvent, the precursor can be removed, while the product stays on the substrate forming freestanding, elevated structures. The thickness of the layer is the crucial length scale in the process. In order to achieve a complete reaction of the precursor into the conductor, the decomposition temperature of the precursor has to be reached across the whole film from the probe-surface contact to the precursor substrate interface. In addition, the probes temperature must not exceed the decomposition, melting or sublimation temperature of the formed material. Upon exceeding these temperatures, the formed

structures would be destroyed immediately by the hot probe. In order to reach the decomposition temperature of the precursor while not exceeding the decomposition temperature of the formed organic conductor, the temperature difference between probe temperature and temperature at the film-substrate interface should be as small as possible. As we know from above, this results in the use of very thin films with thicknesses of tens of nanometers.

The question, whether small amounts of sample with probed areas and thicknesses in the size of few nanometers behave in the same way than a bulk of material, is not only of scientific interest. A commercial interest arises from the need of miniaturization of mechanical and electronic products. This is especially true for devices featuring some sort of data storage, like most mobile phones, notebooks and MP3 players. Today's hard drives have storage capacities of around 650 Gbit/in² (100 Gbit/cm²). The length scale of one bit is therefore approximately a square with 100 nm side length (10000 nm²). Increasing the data density by a factor of ten, thus aiming at 10 Tbit/in² (1550 Gbit/cm²) reduces the length scale of one bit by about one order of magnitude to squares with 8 nm side length (64 nm²). One option to achieve such small bit sizes is to use an ultra-sharp tip to indent a storage medium mechanically, thus constructing a nanometer sized punch card. Scanning probe microscopy experiments are a convenient method to probe the suitability of a material for nanoscale mechanical data storage. Another important factor is the time scale required for data storage application. Modern Serial ATA Ports used for hard disks can transfer data at rates of up to 6 Gbit/s. At these rates, each bit has to be written in less than 2 picoseconds. Although parallelization of the writing/reading process can increase this timescale by several orders of magnitude it will still be very short, thus requiring fast experiments to determine a material's suitability.

Nanomechanical devices using probes similar to those used in SPM to manipulate surfaces on length scales of few nanometers are currently investigated as new data storage systems [7-9]. The probes can be actuated very fast due to their small masses which allow short time scale experiments. Aside from altering the topography of a surface [10-13], SPM based data storage can also relay on altering other properties like the polarization of a ferroelectric material [14-16] or the conductivity of redox active polymers [17-19]. Altering the topography of a surface is easy to understand: The probe is used to punch small indents into a storage material, like it was done in the punch cards used in early computer technology. In **chapter 6** I developed a new kind of storage medium for indentation based data storage using the following considerations. The force needed to indent the storage material depends on the material, the size of the probe and the speed of indentation. The force needed to indent a material can be estimated from the material's yield strength Y. The yield strength Y is defined

as the stress at which a material begins to deform plastically. Exemplarily, polystyrene shows a yield strength (as determined from a second time scale experiment and macroscopic indentation) of 70 MPa. As calculated above the indents for data storage should be smaller than 64 nm². Assuming this to be the contact area during the indentation, a force of 40 nN is sufficient to cause plastic indentation. To reduce the needed force for indentation, heatable probes can be used. When the probe's temperature is close or above the material's melting or glass transition temperature, the yield strength of the material will vanish, thus reducing the force needed. At a first glance, this indicates that such indentation should be quite easy, as the needed forces can be easily achieved. However, the simple calculation is based on parameters obtained by macroscopic experiments which probe the material at the centimeter length scale and a second time scale. SPM based data storage is a microscopic technique, manipulating the surface at a nanometer length scale and a millisecond to microsecond time scale. Therefore, deviations from the macroscopic behavior are expected.

The next important issue arises from the expected life time of the written indents. The written indents representing the bits should be stable and detectable for years. In topography based SPM data storage the data is read by scanning a probe over the surface and recording the topography. It is therefore important to investigate, what happens to the surface of the storage medium, when it is scanned copious times. For polymers, it is known that scanning them copious times with an SPM probe can lead to surface wear [9, 20-24]. The exact mechanism of this nanoscale wear is still debated in literature [22, 25]. The importance of surface wear for data storage based on indents becomes obvious upon calculating the expected indent depth. For full plastic indentation and a spherical probe, the radius a of an indent should scale with the radius R of the probe and the depth d of the indent:

$$a = \sqrt{2Rd} \hspace{4cm} \text{(Eq 1)}$$

To achieve a data density of 10 TBit/in², the indents must have radii a below 4.5 nm. Typical SPM probes have radii R around 10 nm. Taking an indent radius a of 4.5 nm and a probe radius R of 10 nm in account to calculate the depth of this indent using (Eq 1), results in an indent depth d of ~1nm. Unwanted surface wear, which modifies the topography by more than 1 nm in height, makes it impossible to read the written indents reliably, thus causing a loss or modification of the stored data. Therefore, regardless of its exact mechanism, surface wear is a decisive factor for a SPM based data storage medium. In conclusion, the storage medium has to be resistive towards nanoscale wear (nano-wear).

Increasing the crosslinking density of a polymer was shown to increase its nano-wear resistivity [22]. Crosslinked polymers were therefore proposed as storage media [26, 27]. The downside of this approach is that crosslinked polymers usually show higher yield strengths and softening temperatures, therefore more force or higher temperatures have to be applied to cause an indent. These higher forces and temperatures may lead to an increased wear of the tip. Tip wear has to be avoided as it leads to a change of the tip radius during the devices life time, so the size of the written indents as well as the resolution for read back changes. Another proposed medium are "Diels-Alder" polymers which fragment upon heating and recombine upon cooling [28]. Thus, at room temperature they are wear resistive. At elevated temperatures, they fragment and can be indented easily. However, the generated fragments of lower molecular weight can be volatile, thus causing a slow loss of polymer, which reduces the medium's life time. As reaction rates depend on temperature, such materials need high temperatures to react at the fast rates required for storage applications.

In order to develop a new medium which combines sufficient nano-wear resistivity with properties allowing indentation at low probe forces and temperatures, I investigated a new concept, separating the needed properties in different layers of a stacked structure (**chapter 6)**: A sublayer providing good indentation properties covered by a protection layer which provides resistivity against tip induced surface wear. The advantage of this approach is that the materials governing indentation and nano-wear resistivity can be optimized independently. Materials which are easy to indent but lack a sufficient nano-wear resistivity can be enhanced by simply adding a second layer. This yields in a broader variety of suitable storage materials.

Upon designing such a bilayered system another length scale issue turns up. For a bilayered material, the critical length scale is the thickness of the wear resistive layer. The thickness of the protection layer influences the force exerted on the sublayer. In addition, for indentation with a heatable probe the thickness of the protection layer influences the temperature reached in the sublayer. A short calculation illustrates the influence of the protection layers thickness on the temperature reached at the sublayer. In a first approximation we consider the thermal conductivity of sublayer and cover layer to be roughly the same. The temperature should than scale approximately linear with distance from the heated probe into the film [29]. The temperature ΔT_{Int} at the interface between protection layer and sublayer can then be calculated from the temperature ΔT_{probe} at the probe surface contact, the radius of the probe R and the thickness of the protection layer $d_{protection}$ using

$$\Delta T_{Int} = \left(\frac{R}{R + d_{Protection}} \right) \bullet \Delta T_{Probe} \qquad \text{(Eq 2)}$$

Equation (2) predicts that for a protection layer with a thickness of the same length scale as the probes radius, the temperature at the interface between sublayer and cover layer would be half of the temperature reached at the probe-surface contact. For a typical SPM probe with a radius *R* of 10 nm, a protective layer with a thickness of just 10 nm will cause a bisection of the temperature at the deformable layer compared to the probe temperature. In order to keep the probes temperature (and the applied force needed for indentation) as low as possible, the wear resistive cover layer has to be as thin as possible.

Now the question is, how thin, yet homogenous and wear resistive layers can be deposited and how their wear resistivity can be probed. In **chapter 3**, I will show an overview about suitable preparation methods for thin films. A SPM based nanowear test [22, 24, 25] which I used to characterize the resistivity of such films on small length scales is introduced in **chapter 2**. During the development of the stacked material it turned out, that the wear observed for different materials and stacks originates from different mechanisms (**chapter 6**). To characterize the bilayered material's indentation properties at times of microseconds, my stacks were then investigated in cooperation with the IBM Research Laboratory (Zurich, Rüschlikon, Switzerland). For the testing, the stacks were used as media in a thermomechanical SPM based storage device [11]. A detailed description of the Millipede device is given in **chapter 6**.

SPM probes can be used to modify the conductivity of redox active polymers locally by applying a voltage between probe and sample [17]. A suitable medium for conductive SPM based data storage needs to show a distinct conductivity contrast between the two oxidation states and the switching between both states must be fast and reliable. In addition, like for all SPM based data storage concepts, the material must be resistive towards probe induced surface wear. In cooperation with Prof. Ono (Tohuku University, Sendai, Japan) and Prof. Gutmann (University Duisburg-Essen, Essen, Germany) I investigated new redox active polymers for their surface stability (**chapter 7**)

The redox behavior of a polymer can be investigated by measuring current-voltage characteristics (I-V curves). Like with the thermomechanical properties, I investigated whether the electrochemical properties change, when we reduce the length and time scale down to the size of a SPM probe and the fast times needed for fast data transfer (**chapter 7**). Furthermore, I investigated whether the electrochemical processes measured in solution are comparable with the processes in a solid film. For

the redox active polymer, the thickness of the film influences the electron conductivity. If the film is too thick, then it acts as an isolator which makes it impossible to induce redox reaction electrically. In order to achieve a suitable medium for conductive-SPM (c-SPM) based data storage, the material has to be characterized in terms of its redox behavior, the conductivity contrast between the oxidation states and its wear resistivity.

Small, heatable probes can be actuated, heated or cooled at very fast time scales due to the small masses involved. When such a probe is vibrated, its resonant frequency will be very sensitive to changes of the probes properties. Therefore, vibrating probes are investigated and used as promising nanosensor systems [30]. The use of a vibrating probe as an ultrasensitive balance for example allows to measure weights down to the attogram regime [31]. As the probes are heatable, they can be used to detect mass changes of a sample placed on them in dependence of the probes temperature. Thus, the heatable probes can be used to reduce the mass scale of the well-established technique of thermogravimetric analysis (TGA) to smaller sample amounts of nanograms or below (nano-TGA) [32]. As only nanograms of material are needed, nano-TGA is an ideal method for samples which are not available in sufficient amounts for conventional TGA or which react to dangerous products. Furthermore, the heatable probes are comparably cheap and can therefore be disposed after the experiment, so they can be used for analyzing samples which react violently upon heating and could therefore cause damage or contamination of the instrument. The question is again, whether the amount of sample influences the result, i.e. whether the result of a nano-TGA experiment is the same as the result of a conventional TGA experiment.

I compared the results of nano-TGA experiments both with nano-TA experiments and conventional TGA measurements on nanocapsules filled with a gas generating agent (**chapter 8**). These "nanobombs" should explode upon heating, thus allowing the release of additional encapsulated material. For a controlled release, it is important to know the decomposition temperature and to explore the release mechanism. For a release application, it makes a clear difference, how exactly the release takes place. Three mechanisms are conceivable: First, the generated gas could lead to an explosion of the capsule distributing its content completely at the moment of rupture. Second, the generated gas could cause a shell rupture from which the content leaks out. Third, the generated gas could just increases the shell size like blowing a balloon, thus allowing the content to diffuse through the weakened capsule's shell. Such differences in the mechanism of release are important as they have big influence on the timescale of content release from the capsule (explosion = fast release, diffusion = slow release). Nano-TGA was a suitable method for the thermal analysis of these

nanocapsules, as there was only a small amount available and the residues of the gas generating agent might lead to contamination of instruments. Although the number of capsules measured in a nano-TGA experiment is small, the result is still an average decomposition temperature of all capsules present on the probe. To determine the decomposition temperature of single capsules, I used the nTA method on single capsules dropcoated from solution. Thus I was not only able to compare the average decomposition temperature measured with nano-TGA with the average decomposition temperature measured with TGA experiments but also with the decomposition temperature of several single capsule.

2.   Fundamentals

In the fundamentals chapter I want to present the fundamental principles of scanning probe microscopy (SPM) and plasma polymerization as I used these methods mainly in my thesis. Besides the physical and chemical principles behind both methods I will also explain the technical realization in the laboratory. Furthermore I'll give several examples for applications which are realized with SPM and plasma polymerization.

2.1   Scanning Probe Microscopy imaging

One of the most versatile senses of a human is the tactile sense. It allows us to gain a variety of different information about a surface with a single touch. While our eyes just provide us an image of the surface and its color, with our tactile sense we can feel the surface's structure, temperature, and many other properties. Scanning probe microscopy (Figure 2) uses an ultrasharp probe to scan a surface, thus recording the topography and other surface properties like the softness, electrical or thermal conductivity, or surface potentials [33-36].
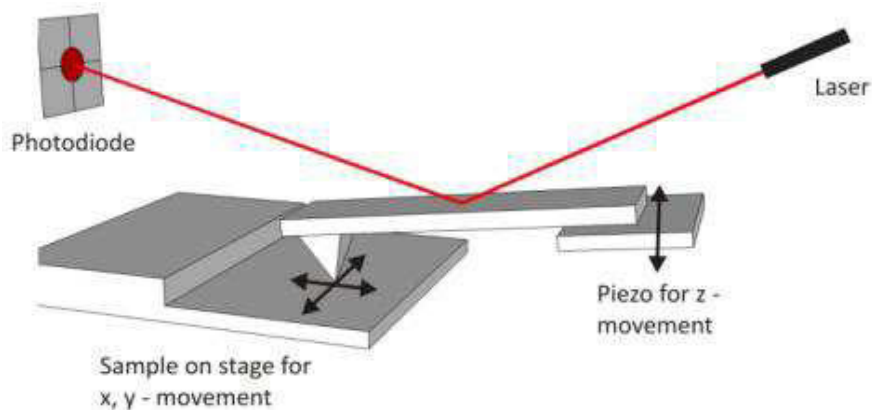
Figure 2: Working principle of an SPM in contact mode. A sharp tip mounted on a cantilever is used as a probe. This probe is raster scanned across a surface. Topographic changes lead to changes in the deflection of the cantilever. The deflection is monitored using a laser beam deflected by the cantilever (optical lever principal). To keep the deflection of the cantilever, and therefore the force between tip and surface, constant, a feedback loop adjusts the z position of the cantilever. Thus, a topographic image of the surface can be recorded using the z piezo position to gain the height at each tip position.

Scanning probe microscopy (SPM), also called scanning force microscopy (SFM) or atomic force microscopy (AFM) was first described in 1986 by Binnig, Gerber and Quate [1]. They described the scanning force microscope to be "a combination of the principles of the scanning tunneling microscope and the stylus profilometer"[1]. Like a human running his finger over a surface to feel its properties, the probe, an atomic sharp tip mounted on a cantilever, is raster scanned across the surface in the x and y plane. As the signal in SPM is caused by interactions between the tip and the surface, the contact area between them limits the resolution. Surface features which are smaller than the contact area cannot be imaged correctly. As the contact area depends strongly on the radius of the tip, the resolution of a scanning probe microscope depends on this tip radius. Using tips with a single atom apex allows atomic resolution and has been successfully demonstrated in ultra-high vacuum [37], and in liquids [38]. The interaction between the tip and the surface is monitored using a laser beam reflected by the cantilever on to a photodiode (Figure 2). For small cantilever deflections the cantilever can be considered as a spring with a linear dependence of the acting force *F* with the deflection *Δz*. The proportionality is given by the spring constant *k*:

$$F = k \bullet \Delta z \qquad\qquad (Eq\ 3)$$

Every change in interaction between tip and surface results in a deflection of the cantilever, e.g. changes in the topography of the sample induces changes in the cantilever's deflection. Feedback loops are used to adjust the z position of the probe to bring the deflection back to the initial value. The z-movement of the probe is than a measure for the topography of the sample. To allow precise movements in all direction as well as precise scanning with nm resolution, usually piezos are used for both raster scanning in x,y-direction as well as for changing the z position of the cantilever (Figure 2). The topography mapping can be combined with the simultaneous measurement of other properties. For example, using conductive tips and cantilevers, applying a voltage between tip and sample and recording the current flow allows the local mapping of conductivity [35]. Using cantilevers with integrated joule heaters and monitoring their resistance while applying a constant heating voltage allows the local mapping of thermal conductivity. Other measurements modes allow the local mapping of mechanical properties, surface potentials, friction etc. Instead of mapping properties while raster scanning the probe across the surface, it can be used for investigating the sample at a fixed position. For example, force distance curves (F-D curves) can be recorded. These F-D curves can be used to characterize mechanical properties, like adhesion and elastic moduli of the surface [39].

2.1.1 Operation modes in SPM

Contact mode

In contact mode, where the tip is in constant contact with the surface, usually the force between tip and surface is kept constant by the feedback (constant force mode). Topographical differences of the surface cause a change of cantilever deflection, thus the position of the laser spot on the photo diode changes (Figure 2). This change is measured by the instrument. According to the spring equation (Eq 3), a change in deflection represents a change of the contact force, thus the feedback loop moves the cantilever in z direction until the force is at the chosen value again. By recording this z-movement while raster scanning the probe across the sample surface a topographic image of the surface is recorded (Figure 2). This intuitive approach works at ambient conditions as well as in liquids on a wide variety of samples. However, there are certain disadvantages of the contact mode. The friction between tip and sample surface can lead to damage of tip or sample. On hard samples, usually the tip wears off during the measurements, which leads to errors in the determination of the size of surface structures due to changing tip radii [40]. On soft samples, even when measuring with the minimum possible load, the forces can be high enough to destroy surface structures and causing a considerable wear of the surface [41]. Samples, which consists of material only loosely bound to the substrate, like proteins on a silicon wafer, can hardly be measured in this mode, because the tip acts like a molecular broom, pushing the proteins together, thus forming agglomerates [20]. Such wear makes it difficult to distinguish between intrinsic features of the surface and artifacts induced by the scanning tip. The lateral forces causing the wear are hard to control as they are not contributing to the vertical deflection of the cantilever and are thus not monitored by the feedback system. However, it is possible to monitor these lateral forces using other operational modes, e.g. in friction force microscopy (FFM).

Intermittent contact mode

Using dynamic operation modes, commonly known as "tapping mode" or "intermittent contact mode" solves most of the wear issues of contact mode experiments [33]. The cantilever is vibrated vertically close to its resonant frequency [42] using a piezo actuator. The motion of the cantilever can be described as harmonic oscillator. As long as the cantilever is far away from the surface it can be described in analogy to the spring equation:

$$F_0(z) = k \bullet (z - z_0) \hspace{3cm} \text{(Eq 4)}$$

15

Here, F_0 is the force acting on the cantilever, k is the cantilever's spring constant, z the deflection and z_0 is the cantilever's rest position. As the tip approaches the surface other forces begin to influence the cantilever. Long-range interactions of van-der Waals type, electrostatics, capillary forces due to a thin water layer formed on almost every surface in ambient conditions, and finally, when the tip touches the surface, deformation of sample and tip [33] influence the cantilevers vibration. All these forces lead to a dampening of the cantilever's amplitude of the cantilever upon surface approach. Therefore, the amplitude of this vibration is commonly detected and used to determine the z-position of the cantilever and thus to gain the topographic information. Close to the surface, the movement of the cantilever can be described as a dampened harmonic oscillator. The dependence of the amplitude $A(\omega)$ of the dampened harmonic oscillator on the excitation frequency can be determined using the steady state solution of the damped harmonic oscillator and ends up with a Lorentzian expression [33]:

$$A(\omega) = \frac{F_0/m_{eff}}{\left(\left(\omega_0^2 - \omega^2 \right)^2 + \left(\omega\omega_0/Q \right)^2 \right)^{1/2}} \qquad \text{(Eq 5)}$$

The amplitude $A(\omega)$ of the cantilever is here calculated from the acting force F_0, the effective mass m_{eff} of the cantilever, the angular resonant frequency ω and the free angular resonant frequency ω_0. Q is the "quality factor" of the vibrating cantilever. The quality factor Q of the vibrating cantilever quantifies the energy dissipation per oscillation cycle, and is therefore a measure for the dampening of the harmonic oscillator. The Q factor can be explained as the energy stored in the oscillator divided by the energy lost in each oscillation cycles. Therefore, lower Q factors indicate a stronger dampening of the oscillator. Of course, not only interactions between sample and probe influence the Q factor. The measurement environment, especially the surrounding "medium", e.g. UHV, vacuum, air or liquids influences the Q factor. More viscous media like liquids lead to lower Q factors, while measuring in vacuum results in higher Q factors.

The Q factor influences the sensitivity of the amplitude towards changes in the resonant frequency. As in intermittent contact mode in air, the amplitude is usually monitored for the instrument's feedback on changing forces between probe and sample, the Q factor is important for the feedback speed of a scanning probe microscope operated in intermittent contact mode. The feedback speed determines the maximum possible scanning speed.

For the amplitude modulated (AM) feedback, the cantilever is excited with a constant operation frequency ω_{Op}, which is left of the free resonant frequency ω_0 (Figure 3) [33]. Upon interactions with the surface, the resonant frequency is shifted to higher values for repulsive forces or to lower values for attractive forces. As the amplitude depends strongly on the resonant frequency (Eq 5), a change in amplitude appears. Upon changes of the amplitude, the z-position of the probe is altered to adjust the amplitude to the initially set value (amplitude setpoint). The operating frequency is chosen to be left of the free resonant frequency to be sensitive towards small changes of the amplitude. When the probe would be operated at its free resonant frequency, small changes of the resonant frequency caused by external forces would cause almost no change in amplitude (Figure 3).
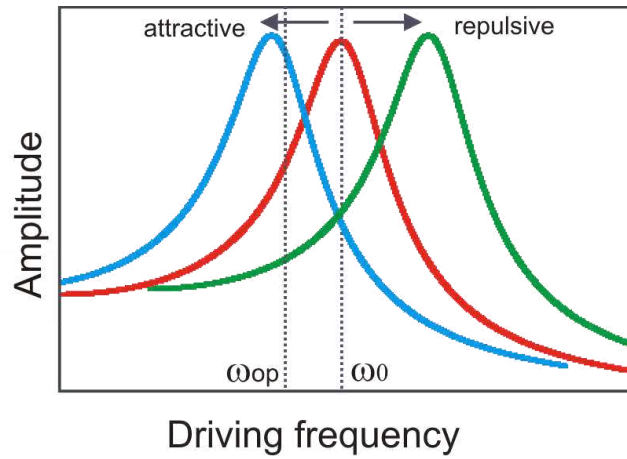

Figure 3: Resonance curve of the harmonic oscillator vibrating freely (red curve) and under the influence of attractive (blue) and repulsive (green) forces. When the cantilever is vibrated at an operation frequency ω_{Op} left of the free resonant frequency ω_0 the amplitude at ω_{Op} changes under the influence of external forces, e.g. interactions between the vibrating probe and the sample surface [33].

Due to the short contact time between the tip and the surface, damaging of soft samples is drastically reduced using this intermittent contact mode. In addition, using the amplitude modulation in the regime of the short ranged interaction forces, meaning the tip touches the surface in every cycle, offers an intriguing second way to gain additional information about the scanned surface: Monitoring the phase shift between the excitation (known from the driving signal of the piezo) and the generated oscillation of the cantilever gives insight in the local mechanical properties of the sample (phase imaging) [33]. Different material or surface properties lead to different phase shifts.

2.2   Mechanical interaction between probe and surface

2.2.1   Force-distance curves

In addition to the above explained phase imaging, other SPM experiments can be performed to analyze the mechanical behavior of the sample surface or to probe interactions between the sample surface and the SPM tip. The first experiment is the recording and analysis of force-distance curves [39]. For the recording of a force distance curve, either the sample or the tip (depending on the used instrument) is moved up and down, and the resulting deflection of the cantilever is measured. This measurement results in a plot of cantilever deflection Z_C versus piezo height Z_P (Figure 4).
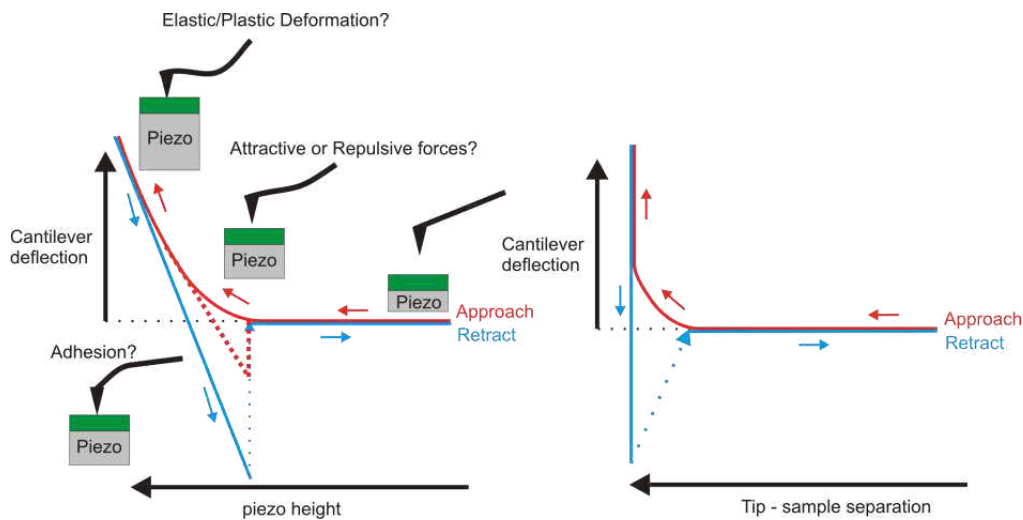

Figure 4: Schematic of a standard force measurement (force distance curve, FD-curve). The cantilever deflection Z_C is plotted against the piezo height Z_P. The drawn curve would result from contact between SPM tip and a non-deformable surface. Attractive and repulsive forces and the behavior of the surface influence the shape of the FD-curve. To analyze force-distance curves, the deflection signal is translated into the tip sample separation or distance D. For a non-deformable surface D can be calculated using $D = Z_C + Z_P$ [39].

On a hard, non-deformable sample, the tip approaches the surface, as the piezo extends, without any change in deflection, until it comes into the range of attractive or repulsive forces acting between tip and sample surface. Attractive forces may lead to a sudden "snap into contact" when the tip is close enough to the surface (indicated by the dashed red curve in Figure 4), while long range repulsive forces may lead to a bending of the cantilever despite the fact that there is no contact between tip and surface (solid red line in Figure 4). After the tip is in contact with the non-deformable surface, the deflection signal scales linearly with the piezo extension as the complete movement of the piezo is transduced into cantilever deflection.

Upon retraction of the cantilever, attractive forces, for example adhesion or water menisci between the probe and the surface, can lead to a bending of the cantilever below its natural shape. When the restoring force of the cantilever resulting from its spring behavior exceeds the attractive force, a sudden snap out (blue dotted line in Figure 4) from the tip position on the surface into its rest position occurs. In order to analyze the recorded data, the curves have to be transformed in a way that the cantilever deflection is plotted against the separation between tip and sample, the distance D. For a hard surface this can be done by assuming $D = Z_C + Z_P$ [39]. For measurements on deformable samples it is mandatory to perform a calibration experiment on a non-deformable sample in order to determine only the cantilever deflection upon piezo movement. On a deformable sample, upon increasing the piezo height the sample is deformed in addition to a change in cantilever deflection. By using the previously determined behavior of the cantilever, the contributions of cantilever deflection and sample deformation can be separated. The spring constant of the cantilever has to be known in order to translate the cantilever deflection into the force applied on the probe using the spring equation (Eq 3). A rough value is provided by the cantilever manufacturer, but the given values can have errors of more than 100%. For exact spring constants, I used the thermal tune method [43]. This approach computes the spring constant of the cantilever by fitting thermal vibrations of the cantilever. The fit just assumes one degree of freedom of the vibrating cantilever and is therefore not absolutely precise. However, the error is around 20 % which is much better than the spring constant range provided by the manufacturer [43].

The interactions between the sample and the probe scale with the contact area between them. This contact area changes when the probe deforms the sample surfaces. On an ideally elastic material, the probe will deform the sample upon approach to a certain depth. Upon withdrawal this depth will be completely restored, thus the contact area change during withdrawal shows the same behavior than during approach. Therefore the forces acting between probe and sample should be the same for approach and retract and the curve recorded on approach should overlap the curve recorded on retract. For samples, which are not ideally elastic and thus shows some plastic deformation during the approach, the sample's surface will not regain its original shape during retract of the probe. Thus, the contact area change during retract differs from the contact area change during approach and thus the forces on retract and approach are different. This force difference leads to a non-overlapping of approach and retract curves. As most samples show a mixed behavior the curves recorded on them do not overlap [39].

Neglecting plastic deformation, the contact area between the probe and the sample can be related to the sample's Young's modulus E. There are different theories which are usually used to describe the relations between the load on the probe F_N, the Young's modulus E of the sample, the samples deformation d and the contact radius a. The simplest theory is the well-known Hertz theory. Hertz [44] theory can only be applied to systems where the adhesion is expected to be much smaller than the applied loads, because the adhesion work W per unit area is neglected [39]. The other two theories were derived by Johnson-Kendall-Roberts (JKR) [45] and Derjaguin-Müller-Toporov (DMT) [46]. Both theories are approximations and differ in the way they account for adhesion. DMT accounts for adhesion outside the contact area, JKR accounts for adhesion in the contact area. Therefore, JKR theory is used for large probes and soft samples with expected high adhesion and DMT is used for small probes and stiff samples with expected small adhesion [39]. With a known probe radius R, both JKR and DMT theory allow calculating the adhesion W from the jump-off contact. An overview over all three models is given in Table 1.

Table 1: Relation between contact radius *a*, deformation *d* and adhesion force *F$_{Ad}$* for spherical tips on an elastic deformable flat surface. *R* is the probe radius, *v* is Poisson's ratio of the sample, *E* the Young's modulus of the sample, *F$_N$* the applied load on the probe and *W* is the adhesion work per unit area [39].

	Hertz	DMT	JKR
$a^3 =$	$\dfrac{3}{4}\dfrac{R(1-v^2)}{E}F_N$	$\dfrac{3}{4}\dfrac{R(1-v^2)}{E}(F_N+2\pi RW)$	$\dfrac{3}{4}\dfrac{R(1-v^2)}{E}(F_N+3\pi RW+\sqrt{6\pi RWF_N+(6\pi RW)^2})$
$d =$	$\dfrac{a^2}{R}$	$\dfrac{a^2}{R}$	$\dfrac{a^2}{R}-\dfrac{2}{3}\sqrt{\dfrac{3}{4}\dfrac{(1-v^2)6\pi Wa}{E}}$
$F_{Ad} =$	0	$2\pi RW$	$\dfrac{3\pi RW}{2}$

Upon plastic deformation, the recorded curve will deviate at a given load from the behavior predicted by the three models. This point is the yielding point. At this load, the probe exerts a pressure on the sample which exceeds the sample's yielding strength Y. The pressure can be calculated from the applied load and the contact area at this point. As before, the yielding point is reached, elastic behavior is observed, the contact area at the yielding point can be determined with one of the

models introduced above. Thus, the yielding strength Y of materials can be probed on the length scale of the probe radius R.

The degree of plastic deformation, thus the permanent deformation d_{rem} can be calculated from the retract curve. It equals the distance between the two intercepts of the retract curve with a line at $F_N = 0$. Using the FD-Curves for plastic indentation of a sample surface is of interest, as very high pressures are achieved under the tip even for small forces. The reason for the high pressures is the small contact area between tip and surface. The time scales of such SPM experiments can be very short, as the approach and retract of the tip using a piezo or even electrostatic excitation is very fast. For example, the stress on the material during a nano-indention experiment is so high, that the same stress would lead to failure of the material in a macroscopic experiment, but causes no damage in an SPM experiment. Therefore SPM techniques allow probing at conditions which are not accessible otherwise.

2.2.2 Nano-wear test

The behavior of a surface upon copious interactions with a sliding contact is an important surface property not only for SPM based devices like storage systems, but also for other nanoscale devices that rely on moving contacts like nano electronic mechanical systems (NEMS). For such applications, the surface must not change upon interaction with the sliding contact, as this change will lead to a different, unpredicted behavior. This change upon interaction with a sliding contact is referred to as wear. As the contact is in the nanometer regime, I will call the induced changes nano-wear. This nano-wear can be quantified with the change in the root mean square (RMS) roughness or the height of a defined surface area upon a defined interaction with a sliding object. The change in RMS roughness or height is then a measure for the nano-wear resistivity of the surface, i.e. the surface's ability to withstand nano-wear. A surface with bad wear resistivity will show changes even after a single contact with the sliding object. To probe the mechanical property of wear resistivity of a surface on a nanometer scale, SPM based nanoscale wear tests are used. For these nano-wear tests, a defined area is scanned a defined number of times with a defined load with the SPM probe. Then images of the scanned area before and after the test are analyzed and compared [22-25, 47-54]. The crucial parameters for this test are the applied load on and the moving speed of the probe.

Hard, inert materials like Si-wafers are not altered in any way (Figure 5). Very soft materials show a massive change in topography, the so called tear wear, where vast amounts of material are removed from the tested area and pile up as rims on the left and right side in fast scan direction of the

cantilever. This mode is for example observed for polyisoprene-b-polystyrene (MW = 24 kg/mol) [22]. Other polymers exhibit "rippling" wear: regular structures of elevated and decreased height compared to the reference area around are formed perpendicular to the fast scan direction [22]. The wavy structures observed for rippling wear often show a very regular and characteristic "wave length" that depends on the exact scan parameters, the molecular weight and the structure, especially the crosslinking density, of the polymer [22].
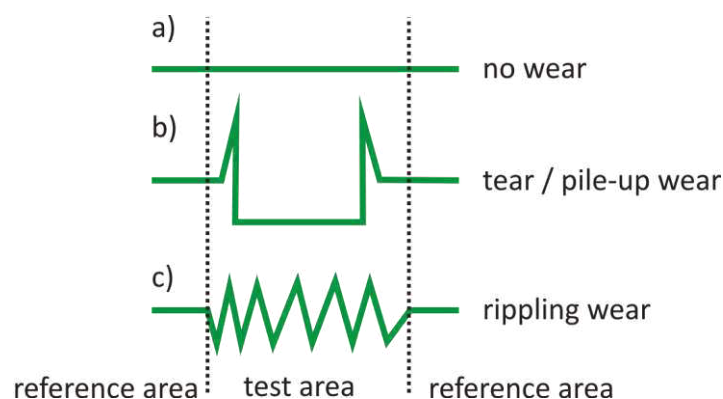
Figure 5: Schematic height profiles through an image recorded after a SPM nanowear test resulting from different wear mechanisms. The tested area is in the center, the non-tested areas on the left and right serve as a reference. a) No wear, as observed on hard materials. b) Tear or pile-up wear: material is removed from the tested area and piles up at the rims, as observed on very soft materials. c) Rippling wear: the material on the surface is rearranged forming more or less regular, wavy structures, as observed on most polymers.

SPM based nano-wear can originate from different mechanisms. One of the first proposed mechanisms for the observed nano-wear on proteins adsorbed on mica was proposed in 1992 by Lea et.al. [20]. They described wavy structures found after scanning adsorbed proteins in contact mode. These rippling structures were explained with the "molecular broom" effect: The moving probe accumulates proteins in front of it in moving direction, sweeping them together. When enough material is piled, the SPM feedback detects the obstacle, moving the tip upwards (Figure 2). Then the process starts again. For polymers, Leung and Goh reported in the same year the formation of lumps of entangled polymer chains [24] during the nano-wear experiment, which they described with a "Stick-Slip" mechanism. The moving probe drags and piles up entangled polymer chains until the probe jumps over the accumulated material. The effect may be enhanced due to the entanglement of polymer chains, as the chains in direct contact with the probe and the entangled chains will be dragged along together. The size of the formed lumps and the distance between them will depend strongly on the molecular weight of the chains, the applied load, and the feedback parameters. Consecutive scanning the same area leads to accumulation of material in a regular pattern. As in this

wear mode no material is removed or added from or to the patterned region, the average height of worn and non-worn regions should remain the same [55].

The second widely acknowledged theory is based on crack-propagation: Elkaakour et. al. explained the formation of lumps by the stress inside the polymer film which is released by the propagation of cracks inside [23] the film. The cracks propagate in front of the moving probe, thus leading to an increase in topography. Again, when the formed lumps reach a certain size, they are detected by the instrument's feedback system, and the probe is moved upwards over the obstacle. Consecutive scanning of the same area increases the size of the lumps and leads again to the formation of regular patterns. The third theory assumes delamination of the film from its substrate, which is closely related to the crack-propagation model. The polymer film delaminates at its interface with the support [55], which leads to the formation of the observed wavy structures. Both mechanisms, crack propagation and delamination, lead to an increased height in the areas showing nano-wear [55]. For delamination, the height difference between worn and non-worn areas should scale linearly with the amplitude of the ripple "waves". However, this linear scaling can only be found for patterns, which can be described with a sinusoidal wave, and assuming that the thickness of the layer itself does not change during delamination [55]. If sinusoidal waves are observed in the tested area and the thickness of the layer is constant, then linear scaling indicates delamination, and non-linear scaling indicates crack propagation according to Schmidt et.al [55].

2.3 Thermo-mechanical interaction between probe and surface

Using heatable probes in SPM allows additional experiments for surface characterization. Heatable probes can be realized by including a joule heater in the cantilever. The joule heater is positioned above the tip. Joule heaters can be integrated in silicon cantilevers by using highly doped, thus conductive, silicon for the cantilever itself and less doped silicon for the heater area. Following Joule's first law, the produced heat Q is proportional to the square current I flowing through the heater multiplied with its resistance R:

$$Q \propto I^2 \bullet R \qquad \text{(Eq 6)}$$

The fundamental formula to describe Joule heating is to relate the power P converted from electrical to thermal energy with the voltage drop V across the heater and the current I going through the heater. Ohm's law can then be used to relate the power P to the resistance R of the heater:

$$P = IV = I^2R = V^2/R \qquad \text{(Eq 7)}$$

From (Eq 7) we expect a quadratic relation between the temperature of a Joule heater and the applied voltage. For probes manufactured from silicon it is important to note that their resistivity will change with temperature. Thus, it is important to measure the resistivity of the probe during heating in order to be able to relate the applied voltage to a certain temperature.

The tip is fabricated beneath the heater area, so it transfers the heat locally to the sample surface thus allowing investigation of thermal properties of the sample very locally. However, it is important to note, that not all heat generated by the Joule heater is transferred to the tip. Part of the heat is dissipated into the cantilever itself and the surrounding medium (air/liquid). Therefore, heatable probes have to be calibrated in order to know precisely at which heating voltage which tip temperature is reached (details on the calibration process are described in the experimental chapter 3.5.2). Furthermore, some of the generated heat can also be transferred via the medium from the heater to the surface. Thus, the surface beneath the probe gets heated, even when it is not touched directly by tip. Calculations by King et.al. showed that ~20% of the generated heat is dissipated in the surrounding air (mainly above the cantilever), the main fraction is transferred via the gap between cantilever legs and sample to the sample surface [56]. Only 0.1 % of the heat is transferred via the tip [29, 56]. For some experiments this heat path via the air is unwanted. The heat transfer via air can be avoided by performing the experiments in vacuum. As in vacuum less heat is dissipated in the surrounding the temperature of the heater at a given voltage may differ from the temperature at the same voltage in air. Therefore, the probes have to be calibrated in the same environment, in which the experiment will be performed.

With heatable probes the local melting, softening or glass transition temperatures of polymers can be determined. For the temperature determination, the probe is placed on the sample surface with switched off SPM feedbacks. The probes temperature is ramped up and the deflection of the probe is monitored. Once the melting, softening or glass transition temperature of the sample is reached, the elastic modulus and the yield strength of the sample decreases or even vanishes. As the force applied on the probe stays constant, the probe can move deeper into the material. Thus, the measured deflection of the cantilever decreases.

Heatable probes allow probing of the thermal conductivity of a sample with high spatial resolution [2, 29, 36]. The probe is heated with a constant voltage and is raster scanned across the surface. A change in the thermal conductivity of the surface leads to a change in the amount of heat transferred

from the heater into the sample. This change in transferred heat causes a change of the heaters temperature, thus a change of the heaters resistivity [57]. By monitoring the heaters resistivity the thermal conductivity of the sample is probed. The same idea can be used for thermal height sensing. The distance between probe and sample influences the heat transferred between them. Upon decreasing distance more heat is transferred, the heaters temperature drops and its resistivity increases. Therefore the resistivity of the heater is used to monitor the probes position. This height sensing is very accurate even at high tip speeds of more than 500µm/s according to Somnath et.al [57]. In SPM based applications with multiple cantilevers operated at the same time or with limited space for the detection system the thermal height sensing is used. For example, in IBMs SPM based data storage system, the "Millipede", written indents are read out via thermal height sensing [11].

Heatable probes allow very local manipulation of surfaces in different ways. A probe heated above the softening temperature of the surface can indent the material with low force, thus patterning the surface. This method is, for example, exploited in thermomechanical data storage [58]. The heatable probes can thermally decompose sample material in order to remove material in a very controlled way, for example as first step in nano-lithography [4]. Also other chemical reactions could be initiated locally on a surface. Another method using heatable probes for surface manipulation is an advanced dip pen nanolithography method. When the tip is heated, the material deposited on the probes tip can flow to the substrate forming structures. The temperature influences the flow rate of the material and therefore the size of the "written" features [6].

Aside from the use in SPM, the heatable cantilevers can be used as nano-mechanical sensors. For sensing applications, the cantilever is vibrated and its resonant frequency is monitored. Upon changes of the cantilevers mass, its resonant frequency changes as well according to:

$$\Delta m = \left(\frac{k}{4\pi}\right) \bullet \left(\frac{1}{f_1^2} - \frac{1}{f_2^2}\right) \qquad \text{(Eq 8)}$$

The mass difference Δm on a vibrating cantilever can be calculated from the change in resonant frequency. Here, f_1 and f_2 are the resonant frequencies of the cantilever before and after the mass change. k is the spring constant of the probe. By placing a sample on the probe and monitoring the resonant frequency during heating, mass losses due to thermal decomposition can be detected [32].

2.4 Electrical analysis and modification of polymer surfaces

SPM tips can be utilized to locally probe the conductivity of a sample by applying a voltage between probe and sample and detecting the flowing current [34, 35]. This is done by grounding either probe or sample and applying a potential to the other one. The flowing current is amplified using very sensitive low-noise current amplifiers. Due to the sensitivity of the amplifiers it is commonly necessary to shield the setup from external electric fields induced for example by other lab equipment, fluorescent lamps or even the normal power grid. Most conductive SPM (c-SPM) experiments are done in contact mode. The microscope's feedback keeps the force acting between probe and sample constant, thus electrostatic interactions do not change the applied force. This is important, because, as introduced (chapter 2.2), a change in force will lead to a change in contact area. The ohmic resistance R between the probe and the tip changes with changing contact area A:

$$R = \rho \bullet \frac{l}{A}$$ (Eq 9)

In this equation, l is the length of the conductor and ρ is the conductor's specific electric resistance.

The conductive scanning probe microscopy was used by Murrell et al in 1993 to detect local tunneling currents on SiO_2 gate films [59] and was later established as a standard characterization technique for semiconductor devices. c-SPM is commonly used for the analysis of organic electronic structures like carbon nanotubes [60] and different materials for organic solar cells.

For c-SPM measurement the probe and the sample substrate need to be conductive. Therefore, cantilever and tip are usually coated with high conductive materials like gold, platinum, iridium or alloys of noble metals. Tips are often coated with platinum-iridium, owing to its hardness and corrosion resistance. Even probes made completely from noble metals are commercially available. Good conductivity of tip and cantilever is necessary because due to the small contact area between probe and tip a high contact resistivity is expected (Eq 9). As polymers usually have a lower conductivity compared to metals, the polymer films need to be thin, as the resistance scales with the length (Eq 9). Thin polymer films are particular important because we cannot apply high voltages. The resistivity of the conductive cantilevers would otherwise lead to the joule heating (chapter 2.3) and the evaporation of the conductive coating. Here again, a platinum-iridium coating is very suitable because it exhibits a high melting temperature.

Mainly two experiments are performed using c-SPM. The first is imaging of the local conductivity. While the tip scans the surface in contact mode like in conventional SPM the flowing current is detected. Thus conductivity and topography images of the surface are recorded at the same time. The second experiment is to probe the sample at a given location regarding its current-voltage characteristics by recording local current voltage characteristics ("I-V-curves") on an area in the size of the tip apex. For such an experiment, the tip is placed on the point of interest. Then the voltage is ramped from minimum -10 V to maximum +10 V and the current is recorded.

For modification of the sample surface, the conductive probe can induce electrochemical reactions in a sample very locally by applying a voltage. Redox active polymers and organic molecules like rose bengal can change their oxidation state by applying a voltage. For molecules like rose bengal, this change of the oxidation state, changes their conductive properties. The local change of conductivity in such materials can be used for data storage applications based on c-SPM. For polymer films made from polyaniline (PANI) and 2,2,6,6-tetramethylpiperidine-1-oxyl (TEMPO) successful patterning of small structures using c-SPM was recently demonstrated [17, 19, 61].

2.5   Plasma polymerisation

Plasma polymerization or plasma deposition is used in industry to deposit thin films because the method allows high yield and high throughput processes. A radio frequency (RF) generator provides the energy for forming plasma at low pressure in a glass reactor. The monomer precursor is a gas in the reactor. The current flowing through this gas cause an electrical gas discharge. The energy set free by the gas discharge fragments the monomer thus forming radicals. These radicals recombine with each other, thus polymerization is started. Usually, the recombination happens preferred at surfaces, for example the reactors walls or solid substrates placed in the reactor. The recombination of radicals and fragments on the substrate surface leads to a coating of the substrate with a homogenous, polymeric coating of variable thickness. The disadvantage of the plasma polymerization process is that the chemical reactions in the plasma are highly complex and not specific, therefore the resulting polymers are not well defined [62]. Due to the radicals involved in the process, the polymers are usually not uniform in their molecular weight distribution, they are highly branched and highly crosslinked [62]. The advantage of the plasma polymerization besides high yield and high throughout rates is the fact that the formed polymers are usually nano-wear resistive because of their high crosslinking, which hinders the mechanisms responsible for wear (chapter 2.2.2). The high crosslinking density makes them very stable towards solvents. Finally, they are usually bond firmly to

the substrate and do not exhibit holes, even for ultra-thin layers. All these properties make them interesting for usage as protection layers.

The exact properties of a film deposited by plasma polymerization depend strongly on the deposition parameters. One of the most important parameters is the power of the RF source. Higher plasma powers lead to more fragmentation of the monomers and thus to more radicals in the plasma. More radicals in the plasma lead to a higher grade of polymerization and crosslinking [63]. It is important to keep in mind that fragmentation is not limited to the monomers. Also already formed polymer chains can be fragmented again. This fragmentation of bigger molecules ("sputtering") is exploited for example in plasma cleaning. During the plasma process, fragmentation and recombination compete against each other. Therefore, the plasma is often used in pulsed mode. In pulsed mode a short energy pulse (t_{on}), usually in the length of tens of microseconds, is followed by a short time without energy input (t_{off}). The radicals formed during the plasma recombine during the time without plasma. Thus, the t_{off} time reduces the sputter rates and increases the deposition rates. Of course, the grade of polymerization and crosslinking depends on the pulse mode and pulse durations as well. Therefore, the mode of operation (continuous or pulsed) and the timing of t_{on} and t_{off} times influences the properties of the film. Furthermore the exact position of the substrate in the sample influences the deposited film. Finally, additional gases beside the monomer can be present in the reactor. For example gases like helium or oxygen increase the fragmentation rate. Additive gases like oxygen can be incorporated into the deposited film allowing further tuning of its properties. The thickness of the film can be adjusted by the deposition time.

Especially plasma polymers deposited from hexamethyldisiloxane (HMDSO) are used as wear resistive protection layers [64-66], because they form hard, silicon-oxide (SiO_x) like surfaces [65]. Due to this oxygen containing surface structure, they form hydrophilic surfaces. More hydrophobic surfaces can be realized by adding small hydrocarbons like methane to the process, thus using a mixed precursor gas of HMDSO and methane. This gas mixture results in films with surface properties similar to diamond like carbon (DLC) films. Coatings made from HDMSO and hydrocarbons exhibit a higher stability at elevated temperatures than pure DLC and do not absorb visible light [66]. They are reported to have less intrinsic stress than pure DLC, which leads to crack-free coatings [66].

Hydrophobic plasma polymers made from oxygen-free precursors are used in the automotive industry to create water repellent glasses for windshields and car windows [67]. In textile industry they are used to increase the contact angle of textiles and fibers up to 142° with water, using 1,2-butadiene as a precursor [68]. In electronics, metallic conductors [64] and passive electronic

components [69] are coated with thin plasma polymer layers for isolation and anti-corrosion purposes. Silver optics are coated to enhance their properties and protect them against environmental influences [70]. In food packaging, plasma polymers are used to reduce the permeability of transparent PET foils with respect to oxygen, water and CO_2 thus helping to keep the packed food fresh for a longer time [71]. More exotic applications involve the protection of metallic archeological objects against humidity, oxygen and H_2S with ultrathin, invisible blocking layers deposited from methane and propane [72]. Here, the advantage of the plasma polymer is the fact, that the appearance of the object is not changed in color or structure.

3. Experimental

3.1 Substrate preparation

Silicon substrates were prepared using the following routine: Silicon wafers (Siltronic AG)(N-doped, [100]) were cut into 2.5 cm x 2.5cm pieces and were cleaned by washing with ethanol and MilliQ-water. After drying with an air gun, the wafer pieces were cleaned for 5 minutes in a plasma cleaner (PDC-002, Harrick Plasma. Ithaca, NY 14850, USA). To avoid contamination of the wafer pieces, they were stored in glass vessels after cleaning. For thermomechanical data storage experiments highly doped silicon wafers provided by IBM were used as substrates, as these highly doped wafers allow enough conductivity for electrostatic excitation of cantilevers. The highly doped wafers were treated as described above.

For highly conductive silicon based substrates, wafers were cut into pieces of 1 cm x 1 cm size and were cleaned using ethanol, isopropanol and MilliQ-water. Consecutively, they were sputtered with 4 nm chrome followed by 40 nm of gold. The chrome layer served as an adhesion layer.

Conductive glass substrates were prepared by thoroughly cleaning glass slides in DCM, acetone, Alconox® and MilliQ water. On the dried glass slides a 3 nm thick layer of Cr as an adhesion promoter was deposited by thermal evaporation. On this layer 100 nm Au were deposited using again thermal evaporation.

3.2 Thin film preparation

3.2.1 Spincoating

To prepare thin films two different techniques were used. Thicker films ranging from 20 nm to 100 nm were prepared using spincoating of conventional polymerized polymers which were either synthesized in house or provided by commercial suppliers. Spincoating is a commonly used coating process [73]. A solution of the polymer is dropped on the substrate, which is mounted on a rotor. Upon rotating, excess solution is flung from the substrate, thus a thin and smooth film forms. The film's thickness depends on the evaporation of solvent, thus on temperature, air humidity, on the

concentration of the solution and the rotation speed. Controlling these parameters, films with different thicknesses can be made from exactly the same polymer [73].

Single polystyrene films

Polystyrene (125.630 MW, synthesized in house) was used as sample material, because the properties of polystyrene are well known from literature. The thickness of the films was adjusted via the concentration of the spincoating solution and the spincoating rotation speed. For the spincoating of thicker films 0.36 g of PS in 15 ml toluene were used. For the thinner films, 0.1014 g PS were solved in 15 ml toluene. Different accelerations and final rotation speeds led to a variety of PS film thicknesses for both solutions. The thickness of the films was then determined by measuring profiles across a scratch induced with a sharp needle. Acceleration, rotation speed and the resulting thicknesses for both concentration sets are summarized in Table 2.

Table 2: Experimental parameters for PS films with different thicknesses spincoated on Si-wafers

Concentration	0.36 g PS in 15 ml toluene			0.10 g PS in 15 ml toluene		
Sample name	PED PS1	PED PS2	PED PS3	PED PS5	PED PS6	PED PS 7
Rotation speed [RPM]	2000	1000	500	2000	2000	500
Acceleration [Rounds/s^2]	2000	2000	250	2000	1000	250
Thickness [nm]	163	218	318	35	40	63

Polystyrene films for bilayered stacks

Polystyrene (125.630 MW, synthesized in house) was dissolved in toluene yielding in a 2 weight-% solution. Using a syringe, 1-2 ml PS solutions were dropped on the wafer piece, covering it totally. Then the spin coater was ramped up to 2000 RPM at an acceleration of 5000 RPM/s^2. The rotation was left at 2000 RPM for 100 s. After the spin coating process the thickness of the PS layer was measured by means of profilometry and X-Ray reflectivity XRR. This spin coating procedure resulted in PS film thickness ranging from 100 to 120 nm.

Redox-active polymers

To investigate the electrical switchable polymer poly-10-(4-vinylbenzyl)-10H-phenothiazine (PVBPT), it was spin coated on conductive substrates. The PVBPT (13400 g/mol) was spincoated from dry DCM (5 g/l and 10 g/l solution were used for different film thicknesses) at 1000 RPM for 60s. Afterwards the substrates were annealed first in DCM vapor at 50 °C and then in vacuum at 100 °C to improve the smoothness and the surface coverage of the PVBPT film.

13,6-N-Sulfinylacetamidopentacene

The 13,6-N-Sulfinylacetamidopentacene (97%, Sigma-Aldrich) films were prepared either on cleaned silicon wafer (Siltronic AG)(N-doped, [100]) pieces, or on silicon wafers covered with sputtered gold. For the spincoating 0.015 g of 13,6-N-Sulfinylacetamidopentacene (97%, Sigma-Aldrich) was dissolved in 2 ml chloroform. The spincoater was then ramped to a speed of 1000 RPM within one second. After 120 s, the spincoating was finished. The prepared films were stored in the fridge to avoid decomposition of the precursor.

3.2.2 Plasma polymerization

I used a plasma reactor (Figure 6) in order to deposit films with thicknesses from 5 nm to 100 nm on different substrates. The plasma reactor itself is a glass tube with 10 cm diameter and surrounded by a coil antenna, which is attached to a radiofrequency source (Coaxial Power Systems Ltd, Eastbourne, England), via a homemade matching system [74-76]. In addition, a homemade pulse generator can be used to generate pulsed plasma with adjustable t_{on} and t_{off} times of the plasma.

The radiofrequency source can be adjusted in power between 0 W and 150 W. The power of the plasma has a great influence on the properties of the deposited films. The plasma power determines the fragmentation of the monomer molecules. Adjusting the t_{on} and t_{off} times influences the film properties due to a different ratio between sputtering and recombination rate.
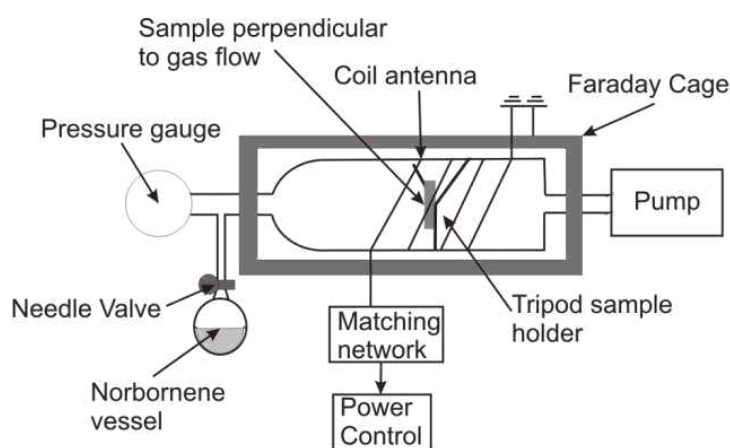

Figure 6: Schematic sketch of a plasma reactor consisting of a 10 cm diameter glass tube surrounded by a coil antenna and attached to a high vacuum pump. Using a tripod glass holder, the substrates can be brought into the reactor perpendicular to the gas flow.

Thin films of plasma polymerized norbornene were deposited on Si wafers and PS covered Si wafers. The monomer used was norbornene (Sigma-Aldrich, 99% purity, bp. 65 °C, vapor pressure 52 mbar at 25 ° [77]). In the first step, the reactor was cleaned using a plasma of 250 mbar partial pressure O_2 and 250 mbar He, which was ignited with 150 W RF power. During the cleaning plasma, the attached vacuum pump was operated at full power. Oxygen-helium plasma shows strong sputtering and should remove organic residues from the reactor. Due to the continuous gas flow, compounds removed from the reactor walls were removed from the whole system or trapped in the liquid nitrogen cooling traps attached ahead of the vacuum pump. The cleaning is of importance as the reactor is used by several researchers using different monomers. In the second step, the sample was placed on a glass tripod holder (Figure 6) in the reactor. In order to get comparable films, the sample was always placed on the same position in the last third of the glass tube. The reaction chamber was then evacuated to less than 0.009 mbar. In order to avoid that large amounts of monomer condense in the cooling trap, the pumping efficiency was reduced to 20% via a throttle valve prior to adding the monomer into the reactor. The norbornene monomer pressure in the reactor was adjusted to 0.05 mbar. Although norbornene is a solid at room temperature, its vapor pressure is sufficient to achieve this pressure without additional heating. After the monomer pressure was stable at 0.05 mbar, the power source was started. To deposit films with different properties, the deposition was carried out with plasma powers varying between 50 and 150 W. We deposited films in pulsed mode (standard: t_{on} = 20 ms, t_{off} = 50 ms) and in continuous mode (t_{off} = 0 ms), too. These conditions were already used to successfully deposit other plasma polymerized materials in this reactor [22, 65, 74-76]. For depositions, the RF source was ramped within seconds to the final power. In pre-experiments, the correct matching parameters were determined, to keep the reflected power as low as possible during the depositions, in order to avoid damage of the RF source. Norbornene plasma ignites at about 40 W and has a pale violet to white color. During the plasma deposition reaction, the pressure increased up to 0.09 mbar. After the plasma reaction the pressure returned to the initial value of 0.05 mbar. As higher plasma power lead to more fragmentation of the monomer and more radicals in the plasma, films deposited at higher plasma power were typically higher crosslinked [78], [79].

For the deposition on Si wafers we operated the plasma in pulsed mode (t_{on} = 20 ms, t_{off} = 50 ms). For the deposition on PS layers additionally continuous mode plasma (t_{off} = 0) was used. By using different deposition times to deposit ppNb on test samples, we determined the deposition rates for both cases in order to be able to produce films with the desired thickness on the samples for the nanowear and indentation tests (Figure 7).
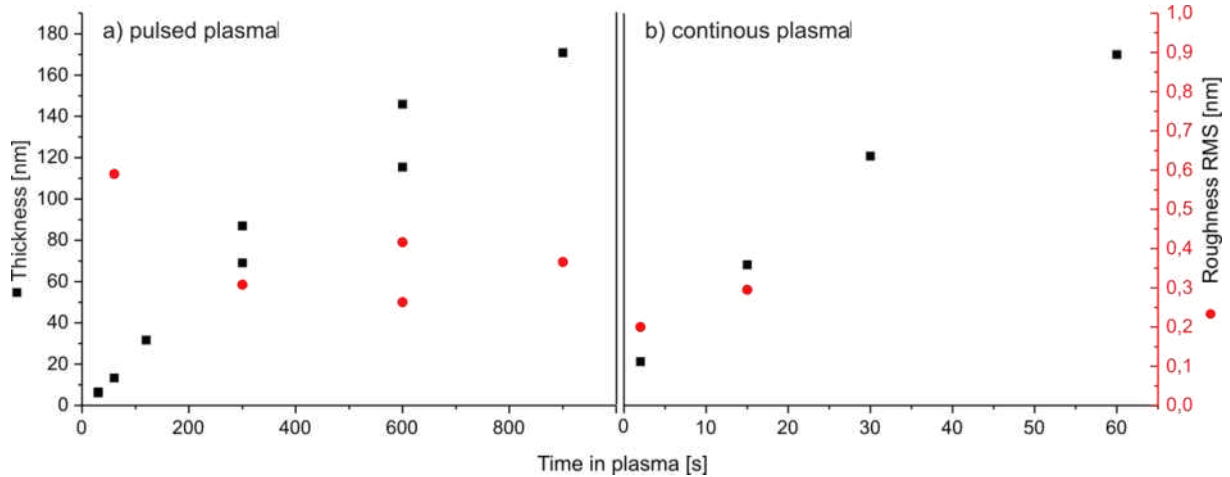
Figure 7: a) Thickness and roughness of ppNb films deposited in pulsed mode at 50 W are plotted against the deposition time. The average deposition rates were 10 nm/min. The resulting RMS roughnesses were in the range of 0.4 nm calculated from a 1 µm x 1 µm square. b) Thickness of ppNb films deposited in continuous mode at 50 W are plotted against the deposition time. The average deposition rates were 10 nm/s. The resulting RMS roughnesses were in the range of 0.4 nm calculated from a 1 µm x 1 µm square.

For the pulsed mode deposition of ppNb on Si-wafers, the deposition rates were in the order of 10 nm/min (Figure 7). In the case of a PS surface and $t_{off} = 0$ we estimated a deposition rate of ~10 nm/s (Figure 7). For ultra-thin films, this results in deposition times of less than one second. The difference in the deposition rates arises from the amount of monomers formed during the course of the deposition. In continuous plasma of one second duration, radicals are formed for one second, whereas in pulsed mode plasma of one second duration, radicals are formed only for 285 µs. The plasma in pulsed mode has just a quarter of the plasma duration compared to continuous mode. On a silicon wafer it was not possible to deposit films using continuous plasma, indicating that on silicon wafers the sputter rates of the plasma exceeded the deposition rate. In pulsed mode the deposition rates are increased, because in the t_{off} time only deposition and recombination can take place, while in the t_{on} time, recombination and deposition compete with fragmentation and sputtering. Regardless of the deposition mode, the roughness of the films as determined as RMS values from 1 µm x 1µm squares recorded with 512 lines and 512 pixels/line where all well below 1 nm (Figure 7).

3.3   Nanocapsule preparation

The nanocapsules were synthesized by A. Hamberger using inverse miniemulsion and interfacial polyaddition [80]. In short: Precipitation in the confinement of an inverse miniemulsion was followed by interfacial polyaddition to form the polymeric shell. This preparation resulted in capsules with diameters around ~ 500nm. As a gas generator, the insoluble silver azide was used. Silver azide is a primary explosive that decomposes between 160 °C and 260 °C forming nitrogen and metallic silver [81]. Further details of the synthesis can be found in [82]. The capsule synthesis via polymerization at the aqueous/organic interface of the droplets in the emulsion has been reported by other groups as well and is commonly used for the synthesis of capsules [83, 84].

For the nano thermogravimetric analysis, the miniemulsion of silver azide containing nanocapsules was freeze dried. First step was freezing the solution in liquid nitrogen and second step was evaporation of the solvent at -60 °C and 0.001 mbar for 24h. The freeze dried capsules were then placed on top of the cantilever using a nanomanipulator. For the analysis of single capsules and the visualization of the shell rupture mechanism, the capsules were drop-coated from cyclohexane on top of silicon wafers. Subsequently, the coated wafers were dried under ambient conditions

3.4   Layer thickness and surface hydrophobicity

Profilometry:

In order to measure the thickness of the single PS and single norbornene films or stacks of PS covered with plasma polymerized norbornene, profiles across scratches made by a sharp needle were recorded (KLA-Tencor P-16+, Milpitas, USA). The films thicknesses were calculated as the mean value of the height difference between scratch and films surface on 6 different positions. The thickness of the ppNb layer which was deposited on top of a PS layer was calculated by subtracting the measured thickness of the polystyrene film from the thickness of the bilayer. The standard deviation in the measurement of the thickness reaches up to 5 nm. Therefore the thickness of thin films (< 10 nm) could not be measured precisely.

***

X-ray reflectivity measurements:

X-Ray Reflectivity (XRR) measurements were performed for determining the thickness of thin layers and of different layers in the bilayered materials. For this purpose, 1 x 1 cm^2 sized samples were analyzed in a Seifert XTD 3003 TT X-ray diffraction system (Seifert, Ahrensburg, Germany). The diffractometer was operated in reflectivity mode with a multilayer mirror as a monochromator at a fixed wavelength of λ = 1.54 Å. The beam size was 1000 × 100 μm^2 (horizontal × vertical) having a resolution in q$_z$ = 6 × 10^{-3} ± 2 × 10^{-3} Å^{-1}. The reflectivity curves (Figure 8) were analyzed with respect to the thickness of the films (d_{Film}) arising from the width (Δq) of the Kiessig fringes by

$$d_{Film} = \frac{2\pi}{\Delta q}$$

(Eq 10)

As in a two layered systems we have three interfaces (substrate-PS, PS-ppNb, ppNb-air), the Kiessig fringes form a complex beating pattern, with two distinct distances (Figure 8).
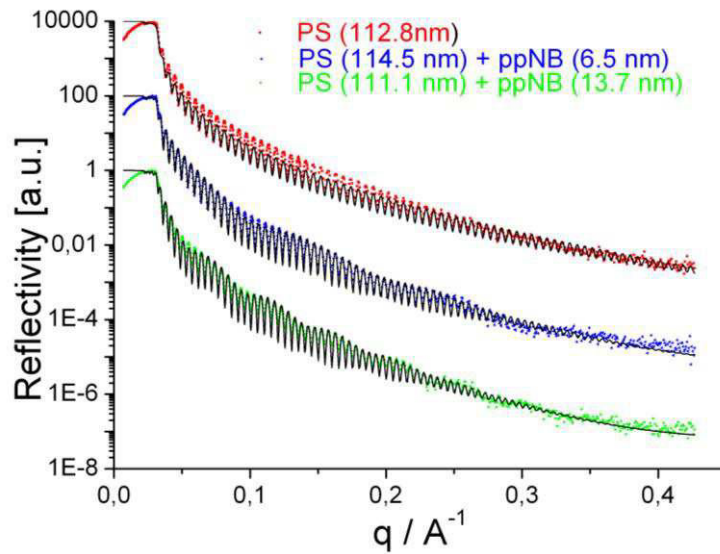

Figure 8: XRR data of blank spincoated PS film (a) and two samples covered with different thick protection layers (b,c). For the stacks shown here, the ppNb was deposited in continuous mode at a plasma power of 150 W. The normalized data of the blank film and the 6.5 nm ppNb protected film are multiplied with 10000 and 100 in order to show all data in one diagram. The black lines represent fits based on Parrat's formalism. Fitting and measurement are in good agreement.

The short distance corresponds to the thick PS layer, the long distance to the thin ppNb layer (Eq 10). For an exact determination of the layer's thickness and the interfacial roughness, Parrat based fits [85, 86] were used. The fits also resulted in values for the roughness of the film's surfaces and the

roughness of the interfaces between silicon wafer and PS as well as the roughness of the interface between PS and ppNb. In the fit function the thickness of both layers, substrate roughness, PS/ppNb interfacial roughness and the ppNb surface roughness were used as fitting parameters. The electron density of the materials was fitted as well. The surface roughness determined by XRR cannot be compared directly to the roughness determined using SPM. This is due to differences in the probed areas: The area probed using XRR is the size of the beam, which is 1000 μm x 100 μm. This area is much larger than the 1 μm x 1 μm area investigated with SPM. Furthermore, the SPM tip has a finite size and thus a different sensitivity towards surface features than the X-Ray beam.

The thicknesses of the plasma deposited norbornene were as low as 6.5 nm (Figure 8). For the investigation of indentation properties we used the stacks with the two thinnest protection layers (6.5 nm and 13.7 nm) as larger thicknesses of the protection layer could have a negative influence on the indentation properties of the stack.

Hydrophobicity

I investigated the hydrophobicity of plasma polymerized norbornene (ppNb) via static contact angle measurements (OCA35, DataPhysics Instruments Gmbh, Filderstadt). The samples were probed using milli-Q water. For all ppNb films we found a static contact angle with MilliQ-water between 80° and 90° which did not change within one month. These contact angles are comparable for contact angles found for PS (88°) [87] or films made from conventional synthesized poly-norbornene (75° - 100°) [88].

3.5 Scanning probe microscopy experiments

3.5.1 Scanning probe microscopes and cantilevers

For imaging I used a Dimension 3100 (D3100) equipped with a Nanoscope IIIa controller (Veeco Instruments, Mannheim, Germany) or a Dimension 3100CL (D3100Cl) equipped with a Nanoscope IV controller (Veeco instruments, Mannheim, Germany). The D3100 Cl has a closed loop scanner and is therefore more precise as the piezo position is constantly monitored by additional sensors. Without the closed loop the piezoelectric elements can slowly move due to piezo creep thus causing a change of position during measurements.

For measurements involving the heatable probes, I used an Enviroscope with a Nanoscope IIIa controller (Veeco Instruments, Mannheim, Germany) and a Nano-TA2 extender (Anasys Instruments, Santa Barbara, USA). The Enviroscope uses the same scanner as the Dimension but it is mounted inside of an environmental chamber which can be evacuated or flushed with different gases. The instrument has a stage heater for substrate heating. The Nanoscope IIIa controller does not allow thermal tune, so the spring constant of the heatable probes could not be determined. As these probes are already mounted into a holder by the manufacture, they cannot be tuned in another instrument.

Nano-wear experiments were performed on a Nanowizard instrument (JPK, Berlin, Germany). This instrument allowed thermal tune, which was mandatory for nanowear experiments as introduced above.

c-SPM experiments and spring constant determination of conventional probes were done on a Multimode Torsion TUNA with a Nanoscope V controller (Veeco Instruments, Mannheim, Germany). The TUNA module consists of a sensitive low-noise current amplifier and a special SPM head. The amplifier is mounted directly next to the cantilever holder for a short connection wires to reduce external noise. The microscope can be covered by a glove bag which can be flushed with dry nitrogen in order to measure without humidity. A heater/cooler scanner allows experiments at different temperatures. For c-SPM measurements I applied the voltage to the sample with the probe grounded.

Beside the AN2-200 heatable probes (Anasys Instruments, Santa Barbara, USA), I used Aluminum coated OMCL-AC160TS-R3 probes (Olympus, Tokyo, Japan) with a resonant frequency in air of 300 ± 100 kHz and a spring constant of~ 26 N/m. The cantilever has a length of 160 μm, a width of 40 μm and a thickness of 3.7 μm. The tip has a length of 14 μm and a tip radius of 7 nm. For contact mode I used NanoWorld Cont-W probes (Nanoworld, Neuchatel, Switzerland). The resonant frequency of these probes is 13 ± 4 kHz, with a spring constant between 0.07 and 0.4. The cantilevers dimensions are (LxWxT) 450 μm x 50 μm x 1 μm. The tip has a height of 10 - 15 μm and a radius below 8 nm. For c-SPM I used CSC17/Ti-Pt probes (Mikromasch, Tallinn, Estonia). These probes are made from silicon coated with a 10 nm Pt layer on a 20 nm Ti sublayer. They have resonant frequencies of 12 ± 3 kHz and spring constants ranging from 0.05 N/m to 0.3 N/m. The cantilevers dimensions (LxWxT) are 460 μm x 50 μm x 1 μm. The tip has a height of 20 μm -25 μm and a radius after coating of 40 nm.

3.5.2 Heatable probes and heatable probe calibration

The heatable probes I used in my work were AN2-200 cantilevers (Figure 9) (Anasys Instruments, Santa Barbara, USA). The horseshoe-shaped cantilevers are batch fabricated from doped silicon. The heater area is composed of lower doped silicon (darker grey shadow in Figure 9 surrounding the white tip) and thus acts as joule heater due to a higher resistance than the cantilever legs. The AN2-200 cantilever have a length of ~ 200 μm, thickness of 2 μm, spring constants from 0.5 to 3 N/m and resonant frequencies between 55 kHz and 80 kHz. They have a tip for SPM based imaging with a radius below 30 nm and can be used for contact and intermittent contact (tapping) mode. The temperature of the tip is controlled using a Nano-TA2 extender (Anasys Instruments, Santa Barbara, USA) which is connected to the cantilever to provide the heating voltage and to the deflection output of the scanning probe microscope for deflection recording. The extender provides a precise temperature control and capability of recording the cantilever deflection.
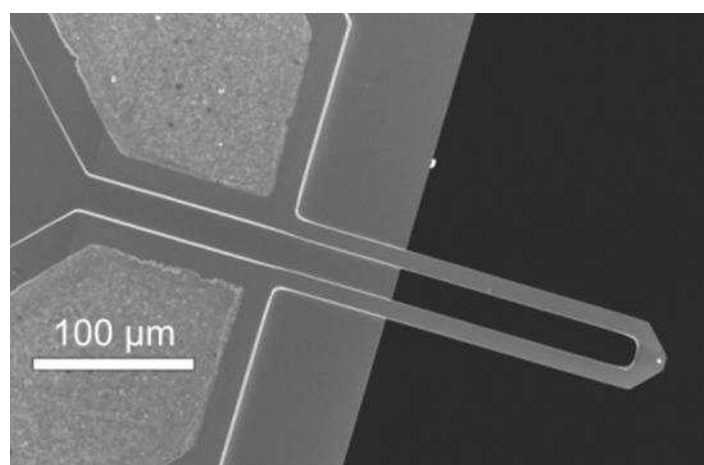

Figure 9: Scanning electron microscope image of a heatable probe (AN2-200, Anasys Instruments, Santa Barbara, USA).

The temperature of a Joule heater depends on the applied voltage. Therefore each cantilever has to be calibrated in terms of voltage-temperature dependence. This calibration is done by recording voltage deflection curves on samples with known melting temperature (T_M) (Figure 10). The samples I used for calibration were 1 mm thick disks of polycaprolactone (PCL) (T_M = 55°C), polyethylene (PE) (T_M = 116°C) and polyethyleneterephtalate (PET) (T_M = 235°C) glued on steel disks. To record these curves, the cantilever is positioned at a fixed position on the surface with the tip in contact with the surface. Then, the feedback which keeps the cantilevers deflection constant is switched off by reducing integral and proportional gain to zero. Heating leads to an increase of the cantilever's

deflection (Figure 10) due to thermal expansion and bending of the cantilever, and thermal expansion of sample and possibly the substrate. When the tip reaches the melting temperature of the sample, the E-modulus of the sample below the tip vanishes, thus the tip sinks into the material causing the deflection of the cantilever to decrease. This decrease in deflection marks the voltage at which the melting temperature of the sample is reached. A quadratic fit function provided by the manufacture allows generating a calibration curve by fitting data points consisting of the recorded voltage and the known melting temperature of the calibration samples. This calibration of the tip is precise (error ~ 1 °C) for temperatures between room temperature and 350 °C according to the manufacturer. The recording of the voltage-deflection curves was controlled with the "Nano-TA studio" software (Anasys Instruments, Santa Barbara, USA). With the "Nano-TA studio" software the calibration files for further measurements were generated.
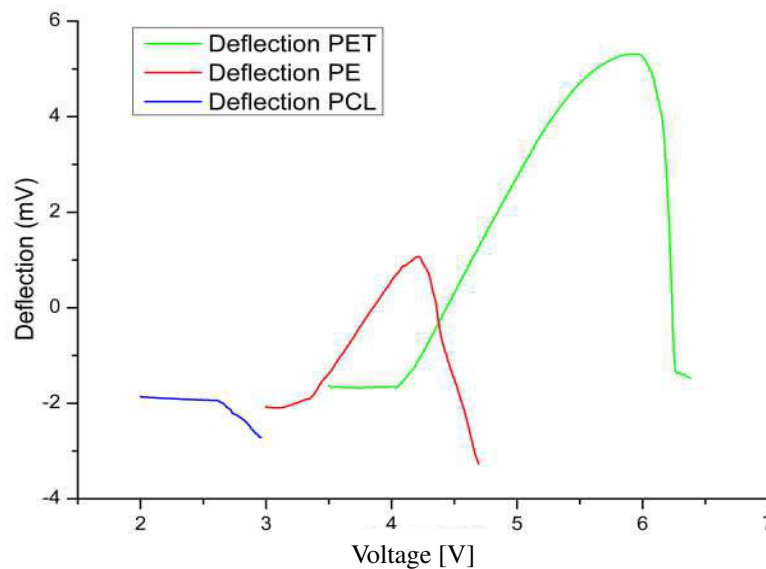

Figure 10: Calibration of a heatable cantilever using three polymers with known melting temperature T_M. The exact voltage at which the decrease occurs is determined by drawing tangents at the linear parts of the curve left and right of the melting point. The intersection of both tangents marks the voltage at which the polymers melt.

Note, that the heatable tip was retracted from the surface before cooling it to room temperature. This retract prevented the tip from being trapped in the sample material as this will freeze immediately upon cooling. This trapping could destroy the tip or cantilever upon retracting. Furthermore, upon retracting, sample material can stick to the tip, changing its radius. To melt or burn away any residual material, the tip was cleaned after each experiment by heating it with the maximal possible heating voltage of 10 V. As the heated area of the cantilever is much bigger than the

size of the tip, heat flow between cantilever and surface can not only occur through the tip, but also through the air gap. Thus, to avoid heat flow between cantilever and surface through the air gap, I usually performed nTA experiments at reduced pressure around 2 mbar.

3.5.3 Nano-wear experiment

In order to test for tip induced nano-wear on the investigated polymer films, I performed SPM based nano-wear experiments. For the experiments I used soft contact cantilevers (NanoWorld, CONT, nominal spring constant 0.2 N/m). The spring constant of each cantilever was determined using the thermal tune method [43]. The surface nano-wear tests [22] were performed following this routine: An area of 3 µm x 3 µm was scanned 100 times at a velocity of 50 µm/s and an applied load of 10 nN. For the redox active polymers I performed additional experiments with an applied load of 5 nN. Afterwards the tested area was imaged at a scan size of 5 µm x 5 µm. For the analysis of the images the free software "Gwyddion" was used. By analyzing the root mean square roughness (on an area of 1 µm x 1 µm) of the tested area we quantified the mechanical nano-wear stability of the film in terms of change in roughness during the experiment. For the analysis of changes in the mean hight of the surface between the worn area and the non worn reference area around it, the images were carefully flattened. Then, the average height of 1 µm x 1µm squares inside and outside the patterned areas was determined. The arithmetic average height inside and outside as well as the standard deviation was then calculated. The height determination is prone to several errors, both from the measurement and the image analysis, which should be considered: First, it cannot be excluded that the tip is not able to measure the exact topography between the ripples, because it does not penetrate deep enough between two bundles. Second, the tip can get blunt during the patterning process. I checked this blunting by imaging several tips before and after the nano-wear experiment, and did not find a distinct change of the tip radius. Third, the measured height difference depends strongly on the exact method of height determination and the flattening process during image processing.

3.5.4 Thermal investigations

Thin polystyrene films

For thermal investigations, the samples were mounted in the chamber of the Enviroscope. The AN2-200 cantilevers were temperature calibrated under reduced pressure and under ambient conditions, as experiments under both conditions were planned. The temperature deflection curves were recorded in the same way as the calibration curves and were analyzed using the "Nano-TA studio"

software. The heating rates were usually 1°C/s. Also FD-curves were recorded on PS films with different thicknesses at different probe temperatures. Before measuring a series of FD-curves on the PS samples, FD-curves were recorded at the given temperature on silicon in order to determine the deflection sensitivity at this temperature. These calibration measurements were used in the force analysis software for the calculation of the adhesion.

Nanocapsules

All SPM analysis experiments with the nanocapsules were conducted in the Enviroscope with AN2-200 heatable cantilevers. The Enviroscope's chamber was evacuated to a pressure of 2 mbar using an external oil pump. The reduced pressure provided a higher Q-factor of the cantilever. The absence of oxygen prevented the decomposition of the polymeric shell by burning, too.

For the nanothermal gravimetric analysis, the resonant frequency was determined before and after loading, using the autotune capability provided the Enviroscope software (V 5.31, Bruker, Mannheim). After loading the cantilever with the nanocapsules it was mounted in the instrument and the resonant frequency was determined. Then the temperature was ramped in steps of 5 K from 140 °C to 250 °C, the expected decomposition temperature range of the silverazide. At each temperature the resonant frequency was determined with an accuracy of 0.015 Hz.

All images were recorded in contact mode with minimum possible force to localize single capsules. After a single capsule was localized, the heatable cantilever was positioned central on top of the capsule. Then, the SPM feedback was switched off and a temperature ramp was performed. The deflection during heating was recorded. After the ramp was finished, the feedback was switched on again, and the capsule was imaged again.

3.5.5 Patterning using heat

13,6-N-Sulfinylacetamidopentacene

The patterning experiments and the imaging of the structures were conducted in the Enviroscope scanning force microscope. The Enviroscope's chamber was evacuated to a pressure of 2 mbar using an external oil pump. Due to the absence of oxygen, side reactions of the precursor with oxygen were hindered. In addition, the formed gaseous products were removed, so neither back reactions nor contamination of tip, sample or instrument are expected. The same instrument and tip was used to image the samples after the patterning step and after the removal of precursor. The conductivity

measurements were performed in the Multimode TUNA TR. Therefore, the samples were marked with crosses by scratching with a needle in order to have structures visible in the optical microscope for localization. The patterning was done by scanning squares with the tip at an elevated temperature. Afterwards the squares were imaged. Then the tip was retracted and the sample table was removed from the instrument. The sample was then washed with chloroform while still mounted on the table. The washing was done by dripping chloroform from a syringe onto the tilted sample. After drying, the table was placed back in the instrument. The removal of the whole table instead of just the sample allowed finding the location of patterning again on other instruments or after the washing.

3.5.6 Patterning using voltage

PVBPT films spincoated on gold coated glass substrate were investigated using the Multimode TUNA. For a rough control of the environment, the whole SPM was covered with a "glove bag". Flushing the glove bag with dry nitrogen or using a gas mixing system to mix dry and humidified nitrogen, the humidity during the measurement can be controlled. The instrument can be equipped with a heatable stage to allow experiments at elevated temperature or to remove physisorbed water from the sample surface, by heating the sample above 100 °C to evaporate the water.

The cantilevers for the measurement were silicon cantilevers coated with a Ti-Pt alloy (CSC-17/Ti-Pt, Mikromasch, Tallinn, Estonia, nominal spring constant 0.15 N/m) and the measurements were conducted in normal contact mode. Most of the writing and reading experiments were conducted under ambient conditions. Only experiments regarding the humidity were conducted using the glove bag. In order to write electrically, a DC bias was applied to the sample, while the tip was grounded. The current flowing through the tip was measured. The general writing voltage V_W was 10 V, the general reading voltage V_R was -6 V. A typical patterning test experiment was similar to the nanowear test. First, I patterned areas of 3 μm x 3 μm with a speed of 0.3 μm/s. To verify that the pattering was successful I zoomed out to a 5 μm x μm area and imaged the flowing current.

However, the SPM does not show zero current, i.e. 0 pA, when we do not apply any voltage, which is counter-intuitive. Instead, it showed a constant signal of ~ 500 fA. The same is true for all applied voltages higher than 0 V.

In some cases reading with V_R = -6 V led to a very noisy image with strong coupling between topography and conductivity signal. In these cases, lowering V_R to -5 V, which is still sufficient to image the differences in conductivity, led to good images of topography and current

3.6 Scanning electron microscopy experiments

The nanocapsules on top of an AN2-200 heatable cantilever were additionally investigated using scanning electron microscopy (SEM). After loading, one of the cantilevers was mounted inside a scanning electron microscope (LEO EM1530 Gemini, Zeiss, Oberkochen, Germany) measurement chamber. SEM images were taken before and after the micromechanical cantilever was heated to 300 °C for 5 min. During the heating the shutter of the electron emitter was closed to avoid damage of the electron source due to changes in pressure or generated metallic silver.

4. Thermomechanical investigations of single layers

Heatable SPM probes can be used for probing the thermal properties of a material with high spatial resolution. The local probing of thermal properties can be utilized, for example, for the identification of different domains in polymer blends by determining the melting, softening or glass transition temperature of each domain. In such a nanoscale experiment time- and length scale effects have to be considered. The thickness of a material may influence the results of an experiment due to an increasing influence of the substrate for thinner films. In the experiments presented in this chapter, the main difference from macroscopic experiments is the length scale. Usually, samples with thicknesses of several 100 nm or above are investigated. Here, I will present investigations of samples with thicknesses below 100 nm.

4.1 Deflection based probing

Effects influencing the deflection

The conventional experiment to determine temperatures at which the mechanical behaviour of a polymer changes (glass transition, melting or softening temperature) with a heatable probe is to record temperature-deflection curves (TD-curves). For the analysis of TD-curves, it is necessary to understand how the deflection signal is caused. There are three effects that add to the deflection signal: The thermal expansion of the cantilever, the thermal expansion of sample, and the indentation of the sample. In addition, a temperature increase can lead to an increase in deflection because the cantilever is bent due to bimetallic behaviour. The thermal expansion of the sample leads to an increase in deflection as the cantilever is pushed upwards. Indentation of the sample causes a decrease of deflection as the tip sinks into the sample causing the cantilever to move downwards. In the simple case of a bare silicon sample, only thermal expansion of sample and cantilever occur, so we expect a steadily increasing deflection signal.

For a polystyrene film, the thermal expansion of the PS and the possible indentation of the PS by the tip add additional contributions to the observed deflection. The indentation of PS should scale with changes of the E-modulus according to the Hertz model, because tip radius and applied force should not change during the experiment (the applied force could change a little during the experiment because of thermal expansion and bending of the cantilever). The E-modulus of PS changes with

temperature [89]. During the glass transition (Figure 11), the E-modulus decreases with temperature until ~ 100 °C, where the rubber plateau is reached.
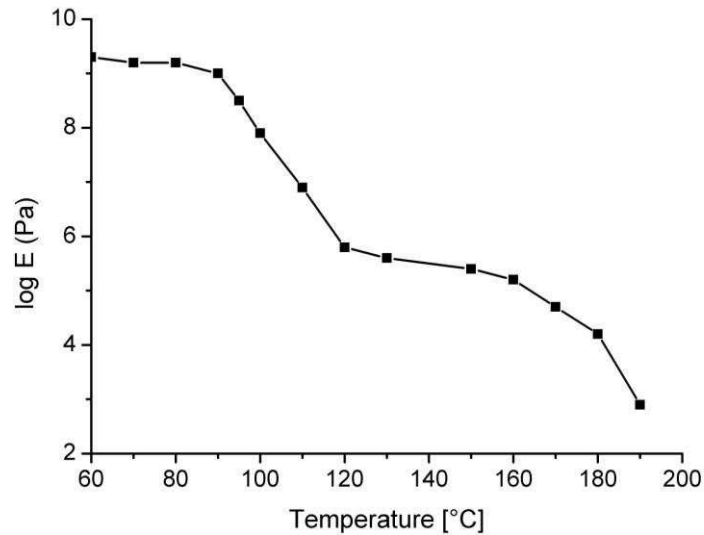

Figure 11: The logarithm of the E modulus of PS plotted against the temperature. The E-modulus was determined from measuring the stress and strain after 10 s of constant straining (stress relaxation experiment). Data is taken from [89]

The PS I used here was ataktic and therefore amorphous, the rubber plateau is short and passes into a regime of further softening at temperatures above 150 °C. Of course, thermal expansion and bending of the cantilever as well as thermal expansion of the probe will also occur when the tip sinks into the sample, so the effects might overlap, thus the recorded deflection will represent the sum of all discussed effects.

TD-curves on silicon and thick PS films

TD-curves recorded on bare silicon (Figure 12 left) showed a steady increase in deflection. However, thermal expansion of the silicon should scale roughly linear with temperature. The recorded TD-curves showed a non-linear correlation between temperature and deflection. The non-linear behaviour is due to bending of the cantilever upon heating. The behaviour of the cantilever on silicon is well reproducible, all curves showed the same behaviour independent of the position at which they were recorded. The slope of all TD-curves recorded on silicon is always positive, which matches the expectations as no indentation should occur. Three regimes can be distinguished. In the beginning (regime I), the TD-curves have a slope of 0.042 ± 0.001 V/K. At the transition to regime II, the slope reduces to 0.0041 ± 0.0006 V/K. In regime III the slope is again increased to 0.0160 ± 0.0004 V/K.

Curves recorded on 163 nm PS (Figure 12 right) showed a single decrease at 126 ± 1 °C. The temperature was determined as the intersection of linear fits of the linear increase before and the linear decrease after the inflection point of the TD-curve (indicated as black dotted lines in Figure 12 right). The temperature of 126 °C matches neither the expected glasses transition nor the softening regime, as this temperature is in the middle of the rubber plateau. Furthermore, from the behaviour of the E-modulus (Figure 11), two regimes with decreasing deflection should be observed, which I did not. If no indentation occurs, then the slope of TD-curves recorded on PS should be higher in regime I than the slopes of TD curves recorded on silicon, because the thermal expansion coefficient of PS (5-7*10^{-5}K^{-1} at 20°C) is bigger than the thermal expansion coefficient of silicon (2.6*10^{-6}K^{-1} at 20 °C).
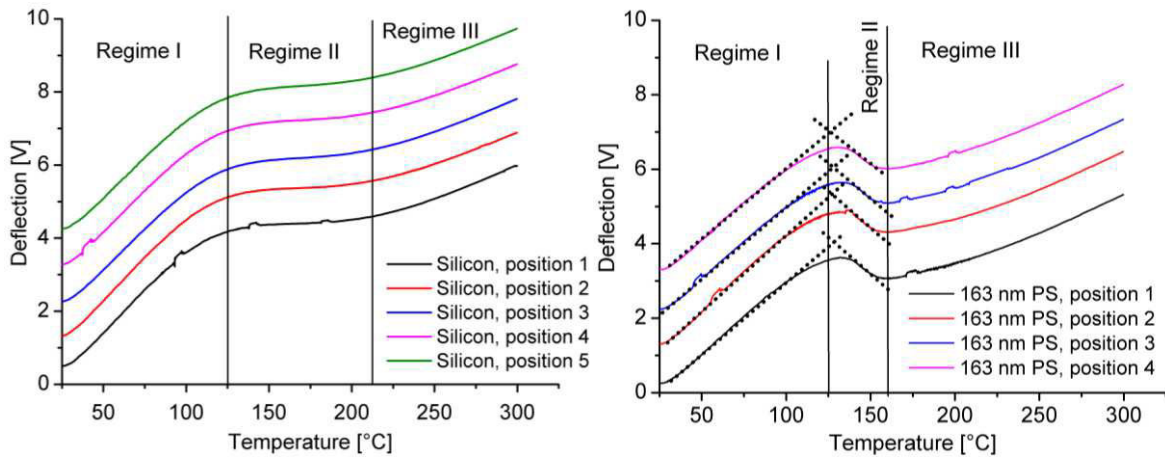

Figure 12: Left: Temperature-deflection curves recorded on bare silicon. Right: Temperature-deflection curves recorded on a 163 nm thick PS film. The deflection signal was shifted by adding +1 V, +2 V, +3 V, … for different positions for better visualisation.

The slopes of the TD-curves on 163 nm PS in regime were 0.038 ± 0.008 V/K, thus lower than the slopes of TD curves recorded on silicon (0.042 ± 0.001 V/K). The best explanation for the lower slopes is that PS is indeed indented due to the lowering of E-modulus. The negative slope in regime II corresponds to the tip sinking into the surface. In regime III the slopes of the TS-curves recorded on PS are 0.0191 ± 0.0003 V/K, thus higher than the slopes of TD-Curves recorded on silicon (0.0160 V/K). In regime III the higher thermal expansion of PS leads to a higher slope of the TD-curves. This finding indicates that the heatable tip did not penetrate completely through the PS film, but that it is still resting on PS, because otherwise the slope of the TD-curves recorded on silicon should not differ from the slopes of TD-curves recorded on PS. This argument is strengthens by calculations of the expected deflection decrease for a complete penetration of the film. For a 163 nm thick PS film the deflection decrease should be 1.8 V for a complete penetration (the cantilever's

deflection sensitivity was 90 ± 2 nm/V as obtained from FD-curves). The observed deflection decrease on the TD-curves on 163 nm PS is 0.6 V, corresponding to an indent of only ~54nm.

TD curves on thinner PS films

The question is now, how the TD-curves change, when the PS film gets even thinner. For thinner films, the signal attributed to the polymer film, i.e. the tip sinking into PS, is proportional to the film thickness.
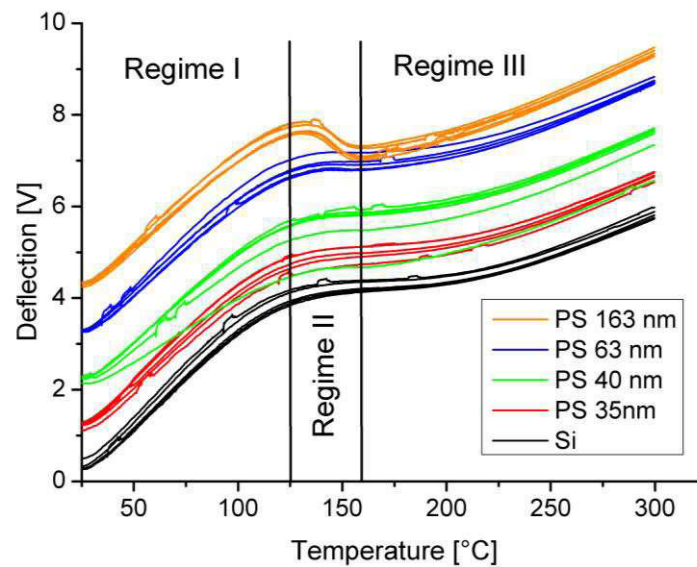

Figure 13: TD-curves recorded on PS with different film thicknesses. 163 nm thick PS and pure silicon are showed for comparison. The PS film curves are shifted by +1V, +2V, +3 V, … for better visualisation.

TD-curves recorded on the 35 nm, 40 nm and 63 nm thick PS films did not show a distinct decrease in deflection (Figure 13). I analysed the slopes of PS curves and compared them with the slopes of curves recorded on silicon. In the beginning (Figure 13, regime I), the slopes of all TD curves recorded on PS were lower than for the curves recorded on silicon: TD curves recorded on silicon showed a slope of 0.042 ± 0.0001 V/K, TD curves on 35 nm PS had a slope of 0.038 ± 0.0008 V/K, on 40 nm PS the slope was 0.038 ± 0.0005 V/K, on 63 nm PS it was 0.038 ± 0.003 V/K and, for comparison, on 163 nm PS the slope was 0.038 ± 0.0008 V/K. Thus, the deflection changes in regime I (Figure 13) were independent of the film thickness. The smaller deflection increase for all PS films indicates that for all PS films deformation must have taken place. In regime II, only for the 163 nm thick PS films a decrease in deflection was observed, indicating that for the thinner films no further deformation is possible. The question is now, whether this means, that the tip has penetrated through the thinner films and is thus resting on the silicon substrate. To check this possibility, I compared the slopes in

regime III. If the tip is resting on the silicon substrate, then the slopes in regime III must be independent from the film's thicknesses. The slope of TD curves recorded on silicon in regime III was 0.0160 ± 0.0004 V/K. For 35 nm PS film the slope was 0.0163 ± 0.0004 V/K, for 40 nm PS the slope was 0.0169 ± 0.0002 V/K, for 63 nm PS the slope was 0.0170±0.0003 V/K, for comparison again for 163 nm the slope was 0.0191 ± 0.0003 V/°C. All TD curves recorded on PS films showed a higher slope in regime III than the TD-curves on silicon. Therefore, I assume that a thin PS layer is still present beneath the tip. The dependence of the slope with the PS film thickness can be explained in two ways: First, the thermal expansion coefficient of PS is higher than the thermal expansion coefficient of silicon, thus the slopes of the curves recorded on PS are higher than the slopes of curves recorded on silicon. For thicker PS films, the remaining PS layer under the tip is thicker, therefore more expansion is observed. Second, the temperature reached in the PS and in the cantilever can depend on the PS thickness, as the silicon substrate serves as an effective heat sink. A higher temperature reached in the cantilever may lead to more bending, explaining the higher slopes observed on thicker PS films. Finite element simulation of a heatable probe in contact with a substrate by Haeberle et.al [36] predicts, that the temperature at the tip surface contact depends strongly on the substrate. Good heat conducting substrates like silicon lead to a drastic reduction of the reached temperature than bad heat conductors like glass according to their simulations (Figure 14).
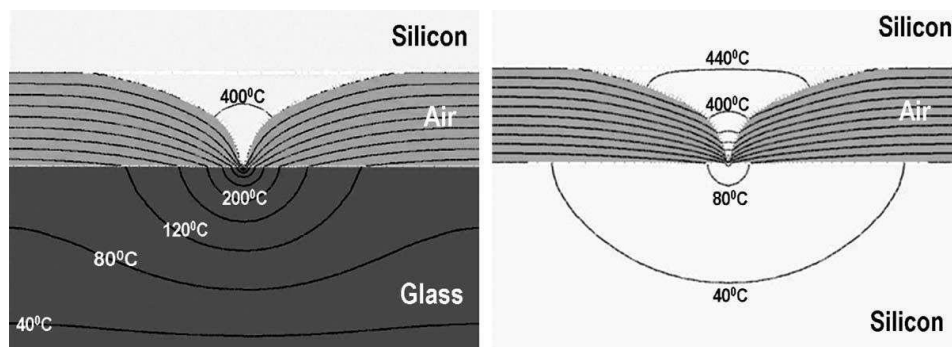

Figure 14: Finite element simulation of probe heated to 400 °C with a probe radius of 10 nm in contact with a bad thermal conductor (glass) and a good thermal conductor (silicon). The probe is surrounded by air. The images is taken from [36].

The different temperatures at the contact on different substrate do not mean, that the temperature of the heater is changed, which would be detected by a changing heater resistance and thus compensated by the instrument. It means that a steeper thermal gradient in the tip occurs as indicated by the isolines in Figure 14. A similar dependence of the temperature reached in a polymer film on the substrate would mean that for thin polymer films a different temperature at the tip

polymer contact and in the polymer is expected than on thick films. The effect depends on the ratio of heat conductivity between the material and the substrate. PS (λ = 0.17 W·m^{-1}·K^{-1}is a bad heat conductor compared to silicon (λ = 148 W·m^{-1}·K^{-1}), so the expected temperature change in contact temperature with film thickness will not be as high as for the direct comparison of glass and silicon.

New approach: Separation of cantilever effects from sample effects

Both thermal effects caused in the cantilever and in the sample influence the recorded deflection. In the conventional approach, the heat induced changes in sample behavior are more prominent than expansion and bending of the cantilever. However, when reducing the thickness of the sample, the expansion and bending of the cantilever becomes more dominant. Therefore, I expanded the conventional analysis of TD-curves by removing the cantilever's influence from the recorded TD-curves. The result is a differential TD-curve (dTD-curve) (Figure 15).
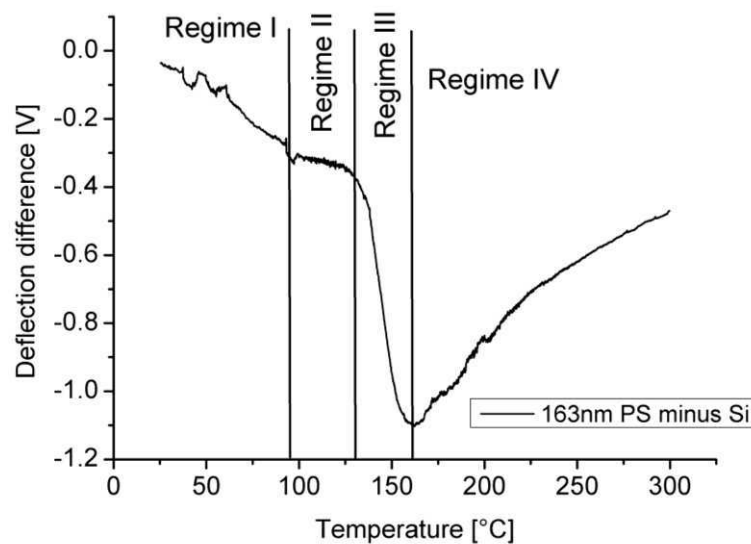

Figure 15: Difference between averaged TD-curves on 163 nm PS and on pure silicon. The jumps are caused by artefacts in the averaged TD-curve of silicon.

In order to separate the influence of the cantilever's thermal expansion and bending from the influence of PS indentation, I averaged TD-curves recorded on silicon and on PS with the same cantilever. The resulting silicon curve should include only deflection signals caused by expanding and bending of the cantilever. The PS curve includes deflection signals from the cantilever as well as expansion and indentation of the sample. In the next step I subtracted the silicon curve from the PS curve. The resulting curve shows then only the changes of deflection caused by sample expansion or indentation (Figure 15).

The curve resulting from subtracting the TD curves on silicon from the TD-curves on 163 nm PS shows four different regimes. In the beginning, the deflection decreases due to a decrease of the E-modulus (Regime I). At 95 ± 1 °C, the deflection decreases is reduced, as the rubber plateau of PS is reached (Regime II). At 126 ± 1 °C the deflection decreases again, as the PS is further softened and the E-modulus decreases again (Regime III). At temperatures above 160 ± 1 °C (Regime IV), the deflection increases again, due to thermal expansion of PS and bending of the cantilever.

Determination of T_G and melting regime of thin PS films

In order to determine glass transition temperatures and melting regimes for the thinner film I separated indentation of the PS film from cantilever expansion and bending again by subtracting the averaged TD-curve of silicon form the averaged TD-curves recorded on the PS film (Figure 16)
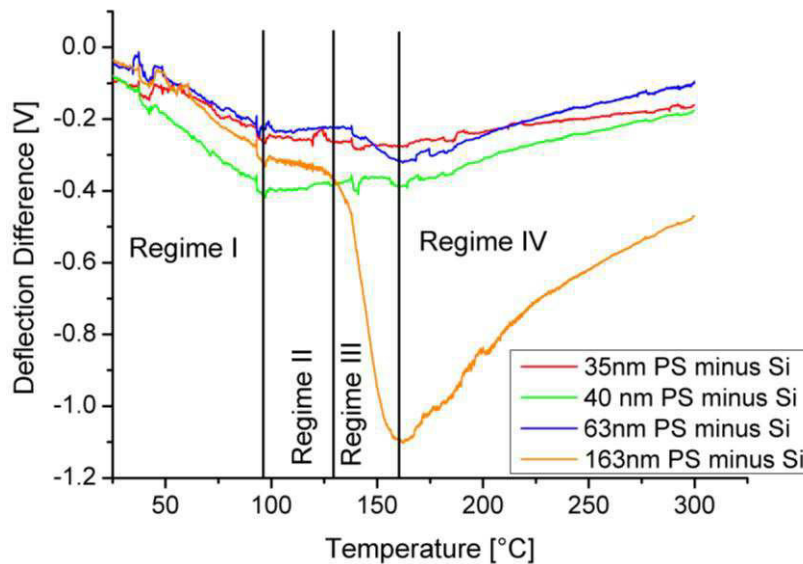

Figure 16: Difference between the averaged TD curves recorded on PS films with 35 nm, 40 nm, 63 nm and 163 nm thickness and the averaged TD curves recorded on Silicon. The jumps observed in all differential curves are causes by artefacts in the averaged TD-curve of silicon and appear therefore at the same temperature for all film thicknesses.

Regime I

From room temperature until 95 ± 1 °C (Figure 16, Regime I), all curves show now a negative slope, indicating, that the initial slope for curves recorded on PS were gentler than the slope of curves recorded on silicon. These negative slopes show that deformation of the PS takes place. The depth reached in Regime I can be calculated, as the deflection sensitivity (90 ± 2 nm/V) of the cantilever was

determined. For the 35 nm thick PS film the initial deflection decreased by 0.17 V (~15 nm) at a temperature of 95 °C. For the 40 nm PS film the deflection decreased by 0.33 V (~30 nm) at 95 °C. For the 63 nm PS film the deflection decreased by 0.2 V at 95 °C (~19 nm deformation). Finally, the 163 nm thick PS film showed a deflection decrease of 0.29 V (~26 nm) at 95 °C. Despite their different thicknesses all films were deformed by 15 nm to 30 nm. The variation of deformation observed may be caused by small differences in the initial force with which the tip was placed on the surface. However, the depth reached here was always lower than the film thickness, so in regime I there must still be PS present under the tip.

Regime II

At 95 ± 1 °C all curves showed a sudden reduction of the slope (Figure 16, Regime II). This temperature was again determined as the intersection of linear fits of the curve before and after the change of slope. This temperature of 95 ± 1°C is close to the expected T_G of PS. Therefore we can explain the reduction of slope observed for all PS films with the behavior of the E-modulus upon reaching the rubber plateau of PS. PS is in the rubber state, so the E-Modulus stays almost constant with increasing temperature. According to the Hertz model, then the indentation depth should stay constant.

However, there is a difference in the curves recorded on 35 nm, 40 nm and 63 nm thick PS films compared to the curve recorded on 163 nm thick PS. The 35 nm, 40 nm and 63 nm thick films were not further indented or even expanded slightly, while the 163 nm thick film showed further, although little, indentation. I attribute the different behavior for the thin and the thick film in the rubber regime to the different thicknesses of the PS layer left beneath the top. For the thinner films only very few layers of PS molecules (the mean square radius of gyration of PS molecules with a molecular weight around 100.000 has been reported to be ~9 nm [90, 91]) remain under the tip. For the 163 nm film, more PS is still present under the tip. For SPM based indentation experiments probing Young's modulus it is suggested that the maximum indentation depths should not exceed 10 % of the films thickness in order to avoid contributions from the substrate [92]. The substrate contributions are explained with a complete compression of thin films, thus they act like the stiff substrate [93]. The same explanation can hold for the TD curves in regime II. Upon increasing temperature here, the applied force increases slightly due to thermal expansion, while the E-modulus drops slightly. The 163 nm PS film is therefore further compressed or even indented. For the thinner films, where only a few molecules are left beneath the tip, further compression is difficult. On the one hand, the molecules can already be completely compressed; on the other hand one molecule could stick to the

tip and one to the silicon substrate because of their adhesion, so the tip will not be able to penetrate through that remaining layer.

Assuming, that the tip rests on a fully compressed layer of PS, the deflection increase observed for the 35 nm and 40 nm thick PS film can be explained with thermal expansion of the PS.

Regime III

The dependence of deflection with temperature observed on all PS films after the rubber plateau depended on the PS film's thickness (Figure 16, Regime III). The 163 nm thick film showed another abrupt change of deflection at 135 ± 2 °C. The 63 nm film showed a similar decrease in deflection, which occurs at 138 ± 2 °C. For the 35 nm and 40 nm thick PS films no distinct change in slope could be determined, instead the deflection increased slightly with temperature due to thermal expansion.

For the 63 nm PS film the deflection reached the maximum decrease of 0.28 V (25 nm deformation) at 160 ± 1 °C. Here, this temperature was determined as the temperature corresponding to the minimum deflection value. The indentation of 25 nm is well below the film's thickness of 63 nm. The 163 nm thick PS film showed the maximum decrease of 1.06 V (95 nm) at 160 ± 1 °C. This indentation depth is well below the films thickness, indicating that a considerable amount of PS is present between tip and silicon substrate. The decrease in deflection observed for the two thicker films can be attributed to the decrease of E-modulus after the rubber plateau. As the E-modulus drops, the tip can further indent the film according to Hertz-model. For the two thinner films, this further indentation is not possible because only few molecules are left between probe and substrate which cannot move. It is again possible, that for the thin films the temperature reached beneath the tip differ from the temperatures reached for the thick film, due to the dissipation of heat in the silicon substrate.

Regime IV

Here, all curves showed again positive slopes, indicating that the curves recorded on PS had steeper slopes than the curves recorded on silicon. The first distinct feature of the curves in regime IV is that the slopes seem to scale with film thickness. Linear fits of the curves in regime IV revealed slopes of 0.00075 ± 0.00002 V/K for the 35 nm, 0.0015 ± 0.0001 V/K for the 40 nm, 0.0016 ± 0.0001 V/K for 63 nm and 0.0044 ± 0.0002 V/K for the 163 nm PS film. As the slope of the curve in the end increases with the thickness of the PS layer I attribute the increase of deflection in regime IV to the thermal expansion of residual PS under the tip and the isolation effect of the residual PS. For a thicker film a

thicker residual layer is present (comparing the difference between film thickness and calculated indentation depth) which also expands more upon heating. In addition, it can be assumed that thicker PS film isolate the tip and the cantilever better from the substrate than thinner films. Thus, higher temperatures are reached in the cantilever and thus more or stronger expansion and bending of the cantilever is expected, which can lead to an increased deflection.

I tried to image the films after heating, in order to check for a permanent indentation. Instead of indentations I found large elevated circular structures with sizes of up to 100 nm (Figure 18). The structures were much larger than the size of the probe tip, which had radii of < 30 nm. Although elevated structures are puzzling at the first glance, there is a good explanation. Before recording the image, the hot probe has to be retracted from the surface to avoid freezing it into the soft PS. Upon pulling the hot probe out of the softened PS, the PS is pulled upwards. This deformation of the soft material is then much larger than the tip size.

Alternative models

The first model I explained in detail assumed, that both changes in the deflection slope are related to a distinct change in the mechanical properties of the polymers which are detected by different rates at which the tip penetrates the surfaces (Figure 17 a). However, the curve resulting from subtracting the silicon background from the curves recorded on PS film can also be explained with two different models (Figure 17 b and c).

The second model (Figure 17 b) is based on the assumption that the tip can move easily across a silicon surface, whereas it is slightly attached to the PS surface. Upon thermal expansion, this fixing of the tip to the PS forces the cantilever to buckle, which is detected as a decrease of deflection. As the thermal expansion is almost linear, a linear decrease of deflection could be expected. Upon reaching T_G, the polymer softens, thus allowing the tip to move horizontally through the material like a plough. Therefore, the measured cantilever deflection stays constant. Note that this interpretation of the curve will lead to the same glass transition temperature as the first model. At the end of the rubber plateau, the polymer softens further, thus the tip can now also penetrate the PS vertically which is detected as the second decrease in deflection
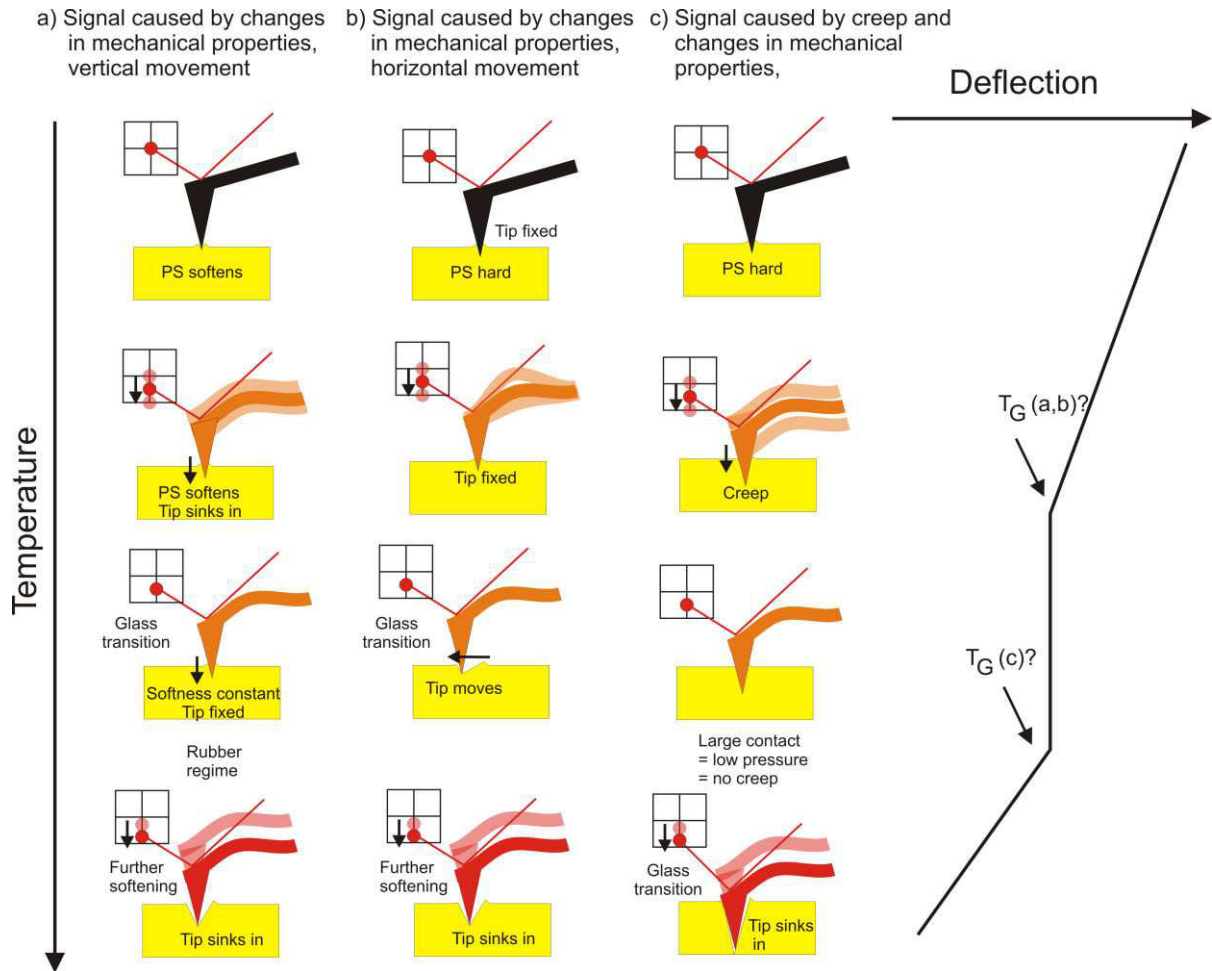
Figure 17: Three models explaining the observed temperature-deflection curve resulting from subtracting curves recorded on silicon from curves recorded on PS. a) Distinct changes at the glass transition temperature and the further softening lead to a change in the rate of tip penetration, thus a change in the observed slope. b) Buckling of the tip, which is fixed by the PS, causes the first deflection to decrease. After the glass transition, the tip moves forward through the PS. When the PS further softens, vertical penetration is possible, thus the deflection decreases again. c) Slow creep of the tip into the polymer causes the first deflection decrease. After a certain contact area is reached the pressure is reduced below the yield strength of PS and the tip cannot move deeper. After the glass transition the tip penetrates deeper into the polymer, thus a second decrease of deflection occurs.

The third model (Figure 17 c) is based on creep. Due to the high pressure beneath the tip, the tip sinks slowly into the material. The penetration is possibly assisted by increasing applied force due to thermal expansion of the lever. As with indentation depth the contact are increases, the pressure decreases and is eventually not sufficient enough to cause additional indentation. Therefore the deflection stays constant. When the glass transition is reached, the PS softens and allows further penetration. This is detected as the second decrease in deflection. This model would result in a TG of

PS of ~135 °C to 145 °C depending on the film thickness. The film thickness dependence and the deviation from macroscopic experiments can be explained with effective heat dissipation in the substrate. This heat dissipation leads to an effective temperature in the film which is lower than the temperature expected from the calibration experiment.

4.2 Adhesion based probing

The heightening of the PS upon retracting the hot tip from the surface indicates that the heated, thus soft, PS sticks to the tip. Imaging a PS sample on which an array of 15 x 15 (225) FD-curves was recorded while ramping the tip temperature from 25 ° to 190 °C revealed that a certain temperature is needed for the PS to stick to the tip during withdraw from the surface (Figure 18).
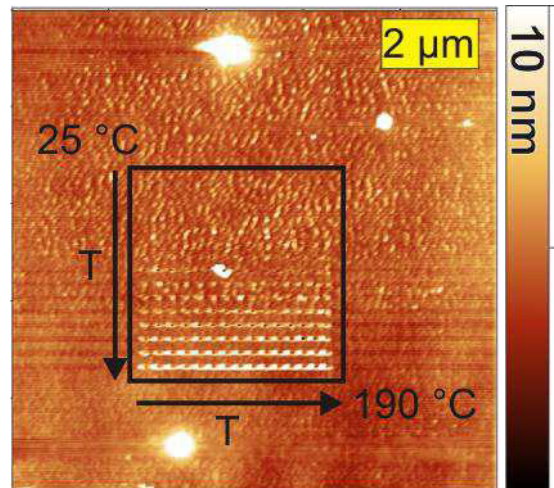

Figure 18: 10 µm sized image of PS after recording 225 FD-curves while ramping the tip temperature from 25 °C to 190 °C. The area on which the FD-curves were recorded is indicated by the black square. The temperature increased from top to bottom and from left to right. The structures formed by pulling of PS from the surface during tip withdrawal can be seen as small white dots which increase in size and height with temperature.

I tried to analyze this adhesion between the PS and the tip in a second approach to directly measure glass transition or softening temperatures of PS. When applying a constant force on a SPM cantilever in contact with a polymer sample, the contact radius of the tip-surface contact should scale with temperature, due to the fact, that the E-modulus of the polymer changes with temperature (Hertz model). Changes of the contact area lead to changes in adhesion between tip and sample. Exemplarily, the different adhesion between PS and tip at different temperatures leads to changes in

behavior of FD-curves recorded at different temperatures. FD-curves recorded on the same PS sample at 30 °C and at 150 °C differ strongly in the retraction part (Figure 19). The adhesion is stronger for the curves recorded at 150 °C than for the curves recorded at room temperature (grey areas in Figure 19).
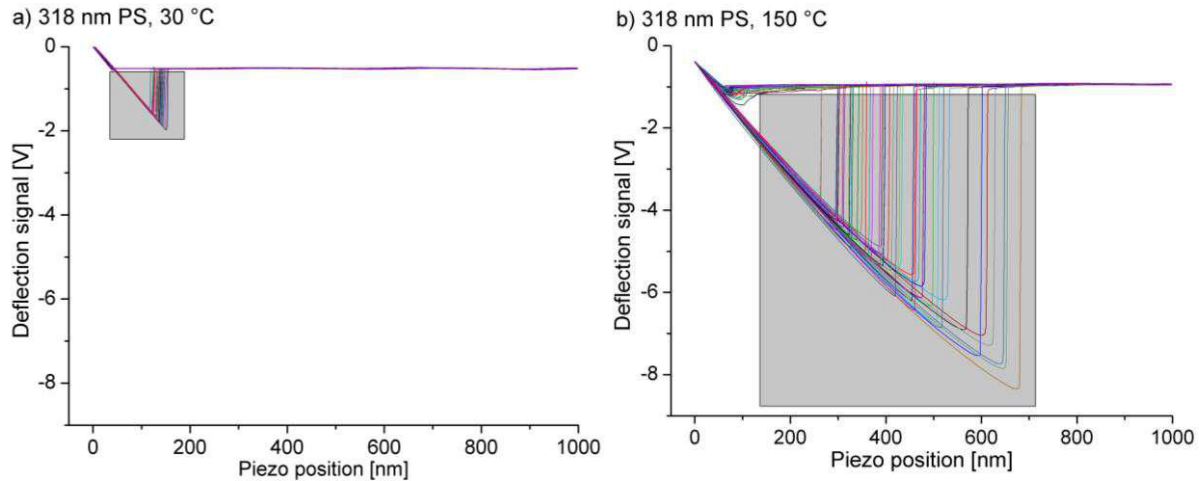

Figure 19: FD-curves recorded on 318 nm thick PS sample at a) 30°C and b) 150 °C. The curves recorded at 150 °C show more deformation and more adhesion than the curves recorded at 30 °C

At temperatures like the glass transition or the further softening, where changes in the elastic modulus occur, changes in adhesion are expected. To identify such temperatures, I recorded arrays of FD-curves on the samples at defined temperatures. One FD-curve array consisted of 100 FD-curves which were recorded in 10 columns and ten rows which were each separated by 100 nm spacing. Thus, each FD-curve was recorded on a pristine area of the surface. The array therefore covered an area of 1 μm² on the surface, so statistical information was obtained. As a reference one FD-curve array was measured on silicon at each temperature. From the force distance curves, the adhesion at each temperature was calculated using the "Force analysis (FA) software" (Michael Kappl, MPIP Mainz, Germany). By plotting the calculated adhesion against the measurement temperature, temperatures at which adhesion changes can be identified.

From the behavior of the elastic modulus with temperature (Figure 11) as well as from the behavior of the TD-curves (Figure 16) the deformation of PS (applying a constant force) increases with temperature until T_G is reached, stays then constant until the end of the rubber plateau and increases then again upon further softening. As the adhesion should scale with the contact area, the adhesion should show scale with the lowering of the elastic modulus with temperature. The analysis of FD-

curves recorded at defined temperatures (Figure 20) did not show the expected change at two different temperatures but only one change.
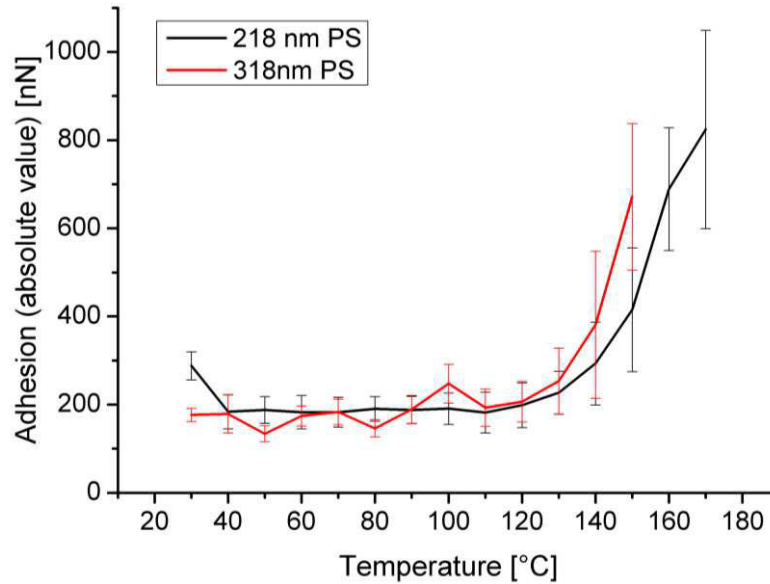

Figure 20: Adhesion calculated from arrays of FD-curves recorded at different temperatures on 218 nm and 318 nm thick PS films. Both films show an increase of adhesion above 110 °C.

For thick PS (thickness 218 nm and 318 nm), the calculated adhesion stayed almost constant at 190 ± 20 nN from 25 °C until 110 - 130°C where it started to increase. In order to reproducibly determine the temperature at which the adhesion changes, I used the following procedure: Lines were fitted through the linear parts in the beginning and in the end of each curve. The temperature, at which the fits intersect, was then taken as the temperature at which adhesion changed. For the 218 nm thick PS sample I determined a temperature of 133 ± 5 °C, for the 318 nm a temperature of 138 ± 5 °C at which the deflection changed. However, the temperature at which the adhesion first deviates from the linear fit of the initial values is lower than the temperatures determined by the intersections. For the FD-curves on 218 nm and 318 nm PS, the measured adhesion was higher than the initial 190 ± 20 nN for all temperatures above 110 °C.

The temperatures of 133 ± 5 °C and 138 ± 5° correspond well to the second change in deflection observed in the TD-curves in the previous chapter (Figure 16, regime III), which I attributed to further softening of PS after the rubber plateau. However, the beginning of adhesion increase at 110 °C could also correspond to the glass transition temperature which is shifted to higher values here due to the higher attempt frequencies, according to time-temperature-superposition. The frequency at which the he force distance curves were recorded was only about 1 Hz, so a T_G of 110 °C is within the range

expected from mechanical spectroscopy. Frequency depending shifts of material properties have been observed when measuring force distance curves with different speeds and heating the sample using a heatable stage (bulk heating) [92]. Here, the heat was applied very locally and only for the short time, during which the probe is in contact with the surface. Therefore, again size effects of the heated area can arise, especially when the film thickness is in the same range than the tip radius. The next experiment was therefore to reduce the film thickness and investigate how this reduced film thickness influences the adhesion between tip and sample.

The same experiment described for thick PS films was repeated on thin films. Again, arrays of FD-curves were recorded on the PS films and on silicon every 10 °C between 30 °C and 180 °C. From this curves the adhesion was calculated and plotted against the temperature (Figure 21).
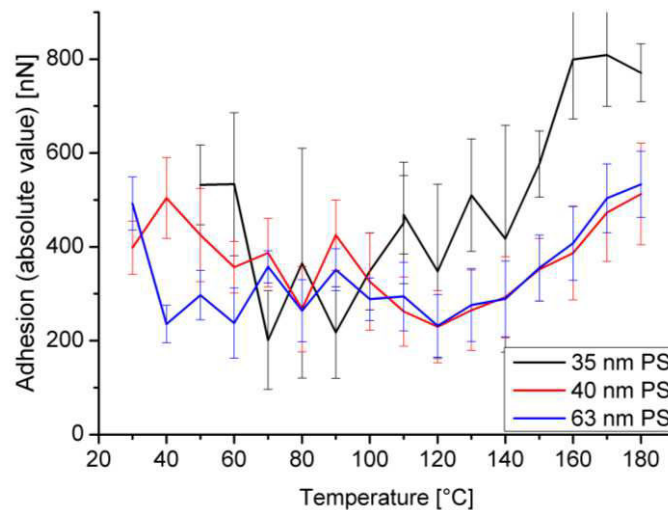

Figure 21: Adhesion calculated from sets of FD-curves recorded on 35 nm, 40 nm and 63 nm thick PS films on Si substrates. The adhesion became stronger at temperatures above 120 °C but the increase is less pronounced than thicker films.

The adhesion calculated for all thin films increased by~ 200 nN between the initial value and the value at 180 °C. The increase temperature, determined as intersection of linear fits of the curves in the beginning and in the end, was 125 ± 5 °C. For the 40 nm and 63 nm thick films deviation from the almost linear part in the beginning took place after 110°C, which is in accordance with the temperatures measured on the 218 nm and 318 nm. For the 35 nm thin film the fluctuations in the beginning were stronger than for the other films. The adhesion calculated for the 35 nm thick PS film (black curve in Figure 21) reached a maximum at 150 °C. Above 150 °C the adhesion stayed almost constant for the 35 nm PS film, while all other films showed a further increase. I attribute the

constant adhesion on 35 nm PS above 150 °C to the small film thickness which does not allow further indentation even at higher temperatures due to the fact that only one to two polymer chains are left beneath the tip. Upon reaching the maximum possible indentation depth, the contact area and therefore the adhesion stays constant.

Comparing the adhesion changes on PS films with above 200 nm thickness (Figure 20) and with thickness below 100 nm (Figure 21) shows, that the expected increase in adhesion is less pronounced for the thinner films. On the thick films, an increase in adhesion of up to 600 nN was observed, on the thin films the increase in adhesion was around 200 nN. This is comparable to the results of the deflection based measurements, where the expected deflection decrease was less pronounced for thinner films. At a temperature of 95 °C, where the deflection showed a change of slope, the adhesion did not show a distinct signal, neither on the thin nor on the thicker PS films.

The length scale seems to influence the result of the measurement. There are two questions: Why and how does the layer thickness influence the measured adhesion and why does the deflection measurement show changes at temperatures at which the adhesion does not change?

For the thickness dependence of the strength of the adhesion signal, similar considerations than for the thickness dependence of the deflection signal can be made, when we assume that the changes in adhesion are mainly based on changes of the contact area. The contact area between the probe and the PS surface depends on the deformation of the surface by the probe. Upon indenting of the sample surface, the contact area between surface and probe increases. For the deflection based approach, thin films cannot be deformed as much as thicker ones, due to less compressibility. Therefore, the contact area, and the adhesion, increases not as strong on thin films as expected from experiments on thicker films. In addition, the heat distribution and dissipation in the film and in the substrate scales with the film thickness and influences the temperature reached at the tip-sample contact.

The different behavior of the deflection and the adhesion based approach at 95 °C may arise from the different heating rates and the different pressure development in the two experiments. In the deflection based approach, the tip is in permanent contact with the sample, and the temperature is increased steadily. The pressure increases with temperature due to thermal expansion. Although I conducted the deflection based experiments at comparably fast heating rates of 1 °C/s, the heating rate in the adhesion based approach is faster: Assuming the sample to have room temperature and the probing temperature to be 100 °C and a recording rate of 1 Hz for the complete FD curve results

in a heating rate above 75°C/s. From the change in the experimental time-scale it could therefore be concluded, that the change in adhesion measured here can be attributed to the glass transition, while further softening takes place at even higher temperatures.

In the adhesion based experiments, the tip temperature is constant all the time, but the pressure increase in the course of the FD-experiment (chapter 2.2.1) due to the tips approach on the surface. Therefore, the main deformation of the sample, thus the main change in contact area, can be caused by the increasing load F_N during FD-curve recording, so a change in Young's modulus due to increased temperature does not cause much additional contact area. In the deflection based experiment the tip is in permanent contact with the surface, in the adhesion based experiment, the contact times are less than one second. Assuming, that the change in the E-Modulus detected by the deflection based method at 95 °C is slow, we cannot detect it using FD-curves due to the fast timescale of each experiment.

4.3   Outlook

In order to investigate whether substrate cooling or mechanical/structural effects cause the different behavior of thick and thin films, substrate heating could be used to avoid cooling of the thin films. By keeping substrate and tip temperature equal, local cooling at the tip sample contact area is avoided. Therefore, the effect of substrate cooling should disappear. Heating the substrate has the disadvantage that it neglects some of the benefits of the nTA. The nTA experiments, owed to the small heated volume, allow high heating and cooling rates of the cantilever, thus fast ramping of the temperature during the experiments. When the substrate has to be heated synchronized, the temperature changes are slow and comparable long times are needed until the whole system is in equilibrium. By substrate heating, the sample is not heated locally anymore, so the experiment is basically changed into a macroscopic experiment. Of course, a high lateral resolution, for example to identify different domains, would still be possible. Another idea that was not tested in detail is to deposit the thin films on top of material which is less heat conducting, e.g. Teflon. Preliminary results of an analysis of thin PS films on Teflon substrates however showed that the behavior of the PS film did not differ from the behavior on Si-wafer pieces.

Still, these results show that the behavior of thin polymer films, especially under very local stress, remains an interesting research field. Especially the substrates effect should be tested using substrate materials with different heat conductivity and with different thicknesses. Furthermore other

polymers with lower and higher glass transition temperatures or PS with different molecular weights should be analyzed in order to examine, whether there is an additional material dependent effect involved. Of special interest would be to investigate materials which show a clear T_G and T_M, e.g. isotactic PS, in order to investigate whether the changes in slope observed for the differential TD-curve can be used to determine both temperatures reliable.

4.4   Main findings

- Conventional nTA, the recording and analysis of TD-curves in order to determine temperatures at which the mechanical behavior of polymer changes fails for films thinner than 100 nm. By recording reference TD-curves on silicon, thus recording the cantilevers behavior with temperature, and subtracting this "background" from the TD-curves recorded on the sample allows the analysis of films with thicknesses below 100 nm. With this method I determined the glass transition temperature for all investigated PS films to be ~95 °C. For the thicker films I identified the end of the rubber plateau at ~135 °C. However, assuming a different model to explain the observed curves could lead to a different temperature determination. Additional experiments are needed to clarify which model is correct.

- For films with thicknesses in the range of few layers of polymer, the observed signals are weaker of even absent. My explanation is that few polymer chains cannot be deformed or indented as easily as a bulk material. On thin films much of the heat is transferred to the substrate and dissipates there because of the better heat conductivity of the substrate.

- The slopes of the TD-curves as well as the indentation depth calculated from the observed deflection decrease proved that the tip does not penetrate through the film in the course of the experiment. For thin films, the remaining layer consists of only 1 to 2 polymer chains.

- The utilization of changes in adhesion upon heating can be used for detecting softening temperatures. Due to the fact that the main source of changing adhesion in SPM based measurements is the change of contact area, the changes in adhesion are based on deformation of PS. The E-Modulus of PS decreases with temperature, thus stronger deformation occurs at higher temperatures. The stronger deformation leads to an increased contact area and therefore to an increase of adhesion. Thin films cannot be deformed as

easily as thick films; therefore the changes in contact area are smaller. Thus, the measured change in adhesion remains small.

- The adhesion based approach showed, even for the thinnest films I investigated, a change in deflection at ~ 135 °C. I cannot clearly attribute this adhesion increase to either glass transition or further softening. The differences to the deflection based measurement can arise from the different time scales of the experiments and from the different force and temperature changes during the experiments.

.

5.   Thermal modification of surfaces

On a thick PS film, the heat from the probe radially heats the surrounding material. With time, a larger and larger area is heated. This heated area will eventually exceed the contact area between the tip and the surface (Figure 22). On a thin film, the material will be heated radially as well, but the heat will reach the silicon very fast (Figure 22). As silicon is a much better heat conductor than polymers, most of the heat will then be dissipated in the silicon. Therefore, the heated area will stay smaller. This small heated area is beneficial for the local modification of surfaces. The surface modifications and analysis methods I presented so far were based on mechanical deformation of the samples surface at different temperatures.
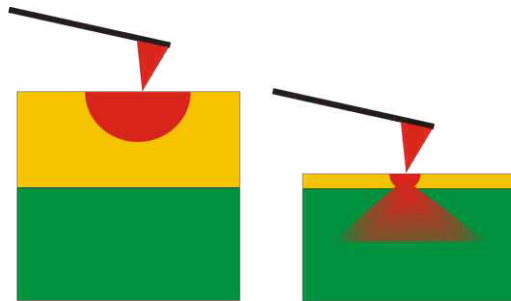

Figure 22: Heat distribution in thick and thin films with lesser heat conductivity (yellow) on a good heat conductor (green) upon heating with a small probe. For thick films (left image) a large area of material is heated. For thin films thickness the heated area is smaller because the heat is dissipated in the substrate, which is a better heat conductor.

Here, I will show how the heatable probe can be used to initialize chemical reactions on a surface. These chemical reactions can be exploited to form structures on the surface. Because of the good heat conductivity of the substrate most of the heat is not distributed laterally in the film but vertically into the substrate (Figure 22). Therefore, the volume which is heated by the probe is small, thus the reaction initiated will take place only very locally. I investigated, how locally initiated reactions can be exploited for nanoscale thermal lithography and how length or time scale depending events influence the experiments.

5.1 Patterning of conductive structures

State of the art

One approach is to use thermoresists, which decompose upon heating into volatile material, forming the desired structures by controlled removal of material. This method was used by Pires et. al. who demonstrated three dimensional lithography using a heated SPM tip on a molecular resist by forming a nanoscale 3d image of the "Matterhorn" (Switzerland) in the used resist [4]. Furthermore, they showed that structures written in the resist can be transferred into the silicon substrate using reactive ion etching.

New approach

Another approach is to initiate a reaction in the precursor film which leads to a product with different solubility. Then the patterning step can be followed by dissolving the residual precursor so that free standing structures are formed. In addition to just change the surface topography, "functional" structures, like small conductors can be formed. In order to gain conductive structures I used 13,6-N-Sulfinylacetamidopentacene (Figure 23) (97%, Sigma-Aldrich) as a precursor.
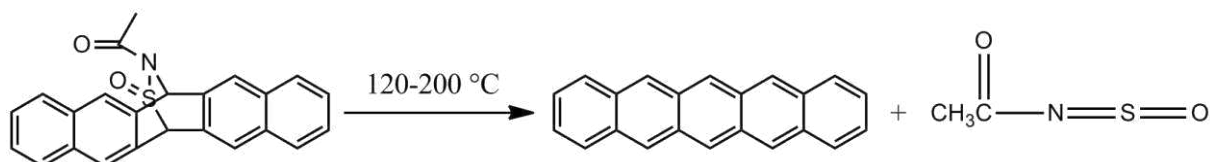

Figure 23: Decomposition of the precursor material 13,6-N-Sulfinylacetamidopentacene into pentacene and N-sulfinylacetamide [94]

13,6-N-Sulfinylacetamidopentacene is commercially available and can be spincoated from halogenated solvents like chloroform. According to the manufacture [95], thin films of this material convert into pentacene by heating to 120-200 °C in 5-15 minutes under nitrogen atmosphere (Figure 23). Nitrogen atmosphere is used to avoid side reactions with atmospheric oxygen. This precursor is used for the fabrication of organic thin film transistors [94]. Pentacene does not solve in chloroform and is known to form electrically conductive structures. The melting temperature of pentacene is around 300 °C, the sublimation occurs at 372 °C (Figure 24). Thus, the precursor material can be thermally decomposed without melting the formed pentacene. Operating the probe below the

melting temperature of the formed material is important, because otherwise the probe would penetrate the film causing defects in the structure which is not desired.
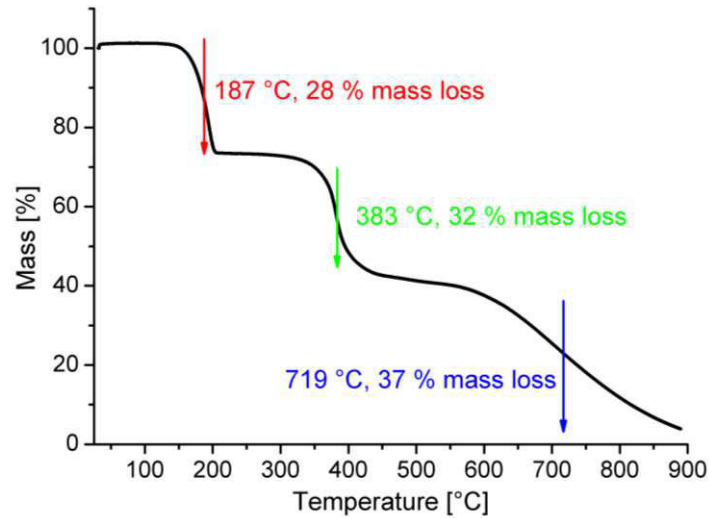

Figure 24: TGA results of 13,6-N-Sulfinylacetamidopentacene. The mass loss with center at 187 °C is the decomposition of 13,6-N-Sulfinylacetamidopentacene to pentacene and the N-sulfinylacetamide which is gaseous above 120 °C. The leaving N-sulfinylacetamide causes the mass loss. The mass loss with center at 383 °C is attributed to the sublimation of pentacene. The slow decay afterwards is caused by the slow thermal decomposition of residual material.

The recorded mass loss with temperature shows two distinct temperatures at which mass loss occur (Figure 24). Both temperatures were determined as the inflection points of the recorded curve's slope. The first mass loss at 187 °C is attributed to the conversion of the 13,6-N-Sulfinylacetamidopentacene into pentacene. The formed N-sulfinylacetamide is gaseous above 120 °C and therefore leaves, thus mass is lost. At 380 °C the second mass loss occurs. This is close to the sublimation temperature expected for pentacene (372 °C), therefore the second mass loss is attributed to pentacene sublimation. The TGA results showed that operating the probe at temperatures of 200 °C should lead to a local thermal decomposition of the precursor without sublimation of the pentacene. A temperature of 200 °C is well below the expected melting temperature of 300 °C. On the other hand, as the temperature may well drop close to the gold or silicon surface [36] so a higher temperature might be needed to cause a complete reaction of the precursor into pentacene across the whole film's thickness. Assuming a linear scaling of the temperature with film thickness, (Eq 2) can be rearranged to estimate a suitable film thickness d_{Film}:

$$d_{\text{Film}} = R\,\frac{\Delta T_{\text{Probe}}}{\Delta T_{\text{Int}}} - R \qquad\qquad \text{(Eq 11)}$$

With tip radius R = 30 nm, a maximum tip temperature T_{Probe} of 300 °C to avoid melting of pentacene and a minimum temperature at the interface T_{Int} of 200°C needed for thermal decomposition of the precursor, the precursor film should have a thickness d_{Film} of ∼ 15 nm according to (Eq 11). However, thicker films may also work, when the patterning step is repeated several times due to the expected higher thermal conductivity of formed pentacene and due to the loss of N-sulfinylacetamide causing the film to shrink.

5.1.1 Results and Discussion

For the SPM experiments I spincoated the precursor on to silicon wafers or gold covered silicon wafers. Gold coated substrates are used in order to be able to measure the local conductivity in further experiments using conductive SPM.

In a first experiment I characterized the films before and after bulk annealing in order to get information about the expected changes in film thickness and surface roughness. These measurements showed that the mean film thickness as determined from measuring the topography across scratches shrank from ∼ 60 nm for the precursor to ∼ 45 nm (height loss ∼ 25%) for the pentacene after bulk heating the whole sample to 200° C for 10 min on a heater plate in a glass vessel flushed with nitrogen. The surface roughness determined from 1 µm x 1 µm squares changed from 0.57 nm to 3.14 nm for the pentacene film after the heating. The increased roughness may be caused by the leaving gaseous N-sulfinylacetamide. The leaving N-sulfinylacetamide causes shrinkage of the film and can lead to the formation of cavities inside the film. The formed pentacene can form π-stacked layers, because they are energetic favorable. The rearrangement of molecules in the film is another reason for increased surface roughness.

Temperature dependence on patterning

To compare the macroscopic results gained from bulk heating I patterned four 4 µm x 4 µm squares in the vicinity of a mechanical made scratch into a pentacene-precursor film (Figure 25) on silicon. The films thickness was ∼ 40 nm determined from profiles across the scratch. All squares were patterned using the same tip in contact mode at a velocity of 0.5 Hz (probe velocity 4 µm/s) and the minimal possible force. The patterns were written at 500 °C, 400° C, 300 °C and 200 °C respectively. Around the patterns, a lot of residual material is visible forming numerous elevated small structures. Such

lumps have not been observed in the bulk experiment. The lumps are most probably N-sulfinylacetamide. As this material is gaseous above 120 °C and in the bulk experiment the whole surface is above this 120 °C it cannot condense on the surface and is removed in the nitrogen stream. During the patterning with the hot probe, the surface is only heated very locally so the escaping N-sulfinylacetamide condenses on the cold surface around the patterned area.
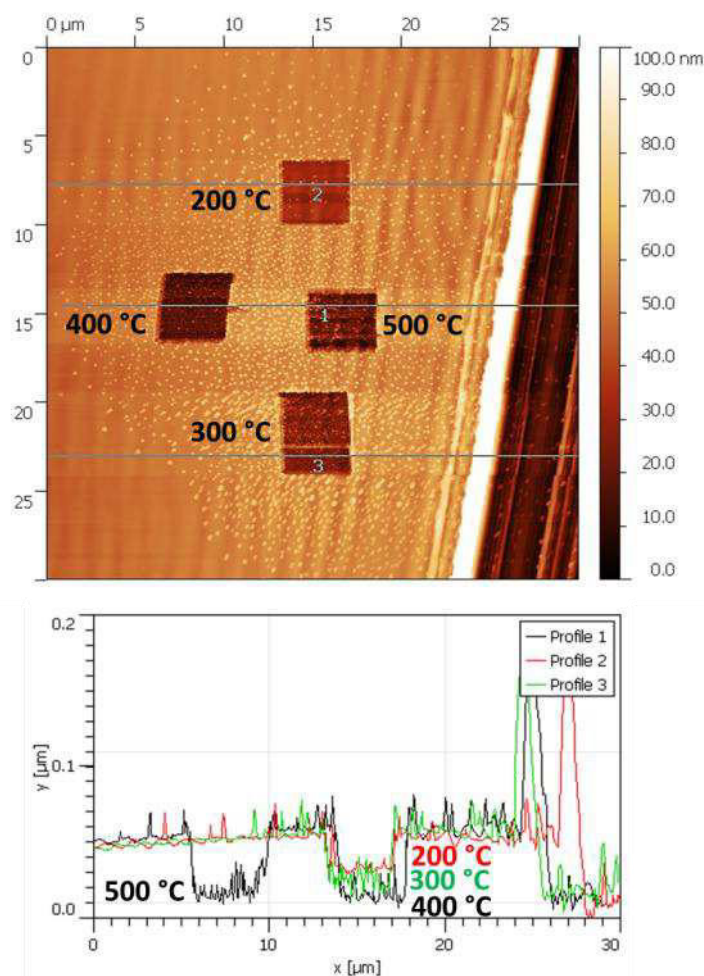

Figure 25: Top: Pentacene precursor film after patterning 4 µm squares at 500 °C, 400 °C, 300 °C and 200 °C. Formed N-sulfinylacetamide material can be seen on the SPM image as small bright dots of elevated height. On the left, the precursor was removed mechanically by scratching with a needle. Bottom: Profiles through the patterned areas and the scratch.

The depth of the patterns scales with the patterning temperature. The depth of the patterns is 15 ± 5 nm (200 °C), 30 ± 5 nm (300 °C), 35 ± 5 nm (400 °C), and 35 ± 5 nm (500 °C). For the two temperatures above the sublimation temperature of pentacene (372 °C), there is only residual material left, which is expected due to the sublimation of pentacene. The different depth of the

pattern written at 200 °C and 300 °C can be explained by two effects: First, the temperature will decrease with distance from the tip, especially close to the interface to the good head conducting silicon. Therefore, the first explanation is that for a probe temperature of 300 °C, the whole precursor film reaches the decomposition temperature and forms pentacene. For the lower temperature of 200 °C, only the first molecule layers decompose, while the molecules close to the substrate stay. Therefore the height loss is less pronounced. The second explanation is that with increasing temperature, the probe induced wear increases, for example due to a lowered Young's modulus. As 300 °C is close to the expected melting temperature of pentacene, an increased removal of material from the patterned area is expected. The latter explanation, increased wear due to higher temperature, is supported by the fact that the rims formed to the left and right of the patterned area are more pronounced for the area patterned at 300 °C. Another hint, that wear induced by the moving probe alters the resulting thickness is the fact that for all patterning temperatures the resulting height loss is above the expected 25 % I calculated for the bulk experiment.

The RMS roughness inside the pattern area increased with the patterning temperature. I determined the RMS roughness from 4 µm x 4 µm squares inside the patterned area. For comparison I determined the roughness for the non-patterned film from the lower left corner. The non-patterned film showed a RMS roughness of 1.2 nm. For patterning at 200 °C the roughness was 4.0 nm, for 300 °C it was 8.8 nm, for 400 °C it was 6.2 nm and for 500 °C the roughness was 9.6 nm. The RMS roughness measured after bulk annealing at room temperature was 3.14 nm, so only the roughness of the pattern formed at 200 °C is in the same range. Patterning at higher temperatures lead to much higher roughness. This higher roughness is caused by sublimation of material above 300 °C and the increased surface wear induced by the probe.

Contact time dependence of patterning

The contact time between the tip and a given area depends on the tip velocity and the operation mode. For contact time shorter than the time needed to reach thermal equilibrium between tip and surface, tip temperatures higher than the desired surface temperature have to be used. All previous experiments with the heatable probes were performed in contact mode. However, here surface wear might play a role so patterning in intermittent contact mode might lead to better results. In intermittent contact mode, the contact time between probe and surface is further reduced, as the contact time is only 10 to 30 % of the oscillation period under usual working conditions [96]. Therefore, higher probe temperatures may be needed to reach the necessary decomposition temperature throughout the film. I used a probe temperature of 500 °C, which lead to almost

complete removal of both precursor and formed pentacene in contact mode and used different patterning speeds and operation modes on a 60 nm thick precursor film (Figure 26) on a gold coated silicon wafer in order to perform conductivity measurements later. The patterned areas were chosen to be large 10 µm x 10 µm squares in order to locate them easily under an optical microscope (Figure 26). This helps to find the exact position after mounting the sample into another microscope for conductivity measurements.
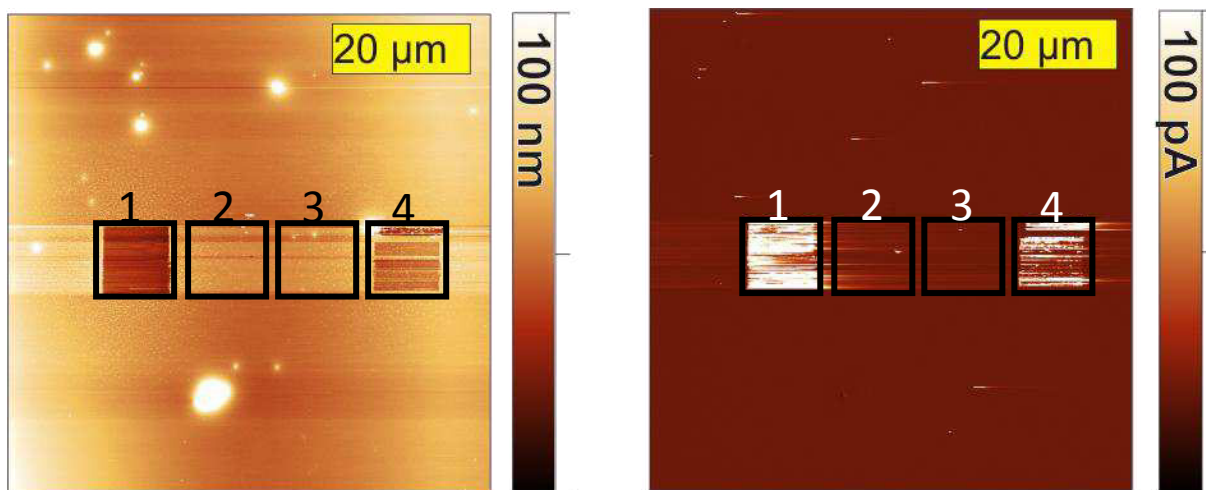

Figure 26: Topography image and conductivity image after patterning the 60 nm pentacene precursor film on a 40 nm gold layer. Patterning was done with a tip temperature of 500 °C at different conditions. Area 1: Patterning in contact mode, tip velocity 0.5 Hz tip (10 µm/s), single pass. Area 2: Patterning in tapping mode, tip velocity 1 Hz (20 µm/s), five passes. Area 3: Patterning in tapping mode, tip velocity 0.1 Hz (2 µm/s), five passes times. Area 4: Patterning in contact mode, tip velocity 0.1 Hz (2 µm/s), five passes. Only the areas patterned in contact mode show a change in topography and conductivity. Again, residual material is found in the surroundings of the patterned areas.

The first result of this experiment was that patterning in intermittent contact mode was not successful, regardless of the speed (Figure 26). At the positions where intermittent contact patterning was used, the topography did not change, neither showing the expected deepened squares nor the surrounding residual materials. Consecutive patterning in intermittent contact mode, i.e. 5 times scanning the same area did not lead to decomposition, too. The squares patterned in contact mode are clearly visible.

The failure of patterning in tapping mode can be explained with the short contact times between tip and sample. The temperature that has to be reached for decomposition is 186 °C. Assuming a sample surface at room temperature (25 °C), a temperature difference of~ 160 °C has to be caused during the

probe surface contact. The probes resonant frequency is ~70 kHz. Each oscillation period has a length of ~ 14 μs, the contact time is then between 1.4 and 4.2 μs. This contact time is even shorter than the contact time of 10 μs used for the indentation experiments in SPM bases thermomechanical data storage (chapter 6). Furthermore, in thermomechanical data storage the tip is pulled into the surface, thus a larger contact area and a better contact is formed, which then leads to a better heat transfer. In intermittent contact mode, the contact forces are much lower, leading to smaller contact areas. Through a smaller contact area less heat is transferred, thus the film cannot reach the required decomposition temperature.

Patterning in contact mode worked as expected (Figure 26). The changes in topography and conductivity depended on the speed of the tip and the number of consecutive scanning. The height in the patterned area was reduced by 20 ± 5 nm for scanning at 0.5 Hz for once (pattern 1) and by 30 ± 5 nm for scanning at 0.1 Hz for five times (pattern 4) (heights determined from profiles averaged across the width of the squares). The RMS roughness inside pattern 1 was 9.2 nm, in pattern 4 the roughness was 4.5 nm. Outside the patterned areas and away from the residual material, the roughness was 3.8 nm. The RMS roughness values were determined from 7.5 μm x 7.5 μm squares. In this experiment, the films were not completely removed due to decomposition of the precursor followed by sublimation of the formed pentacene as one could expect from TGA and the first set of experiments. Even for the copious time scanning at a low tip speed of 2 μm/s, the films thickness was reduced by only ~ 50%. This different behavior between the two experiments may be based on the different substrates: Gold is an even better heat conductor than silicon (thermal conductivity of gold: 310 $W \cdot m^{-1} \cdot K^{-1}$), so following Haeberle et al the temperature gradient in the probes tip and the film should be even steeper (Figure 14), thus the temperatures reached in the film might be lower here.

Conductivity measurements of patterned areas

Both patterns made in contact mode (Figure 26) showed the same maximal current flow of 10 nA during conductivity measurements (9 V applied bias). This is the upper limit of the current amplifier. The average current in pattern 1 (0.5 Hz, 1 time) was 1.2 nA, in pattern 5 (0.1 Hz, 5 times) the average measured current was 3.3 nA. The less or even non-conducting stripes in pattern 1 are the same areas in which less or no change in height was observed. These stripes may be caused by measurement artifacts caused by the high tip velocity, for example short periods in which the probe was retracted from the surface.

Both patterns showed, independent of their thickness, the same maximum current of 10 nA, however pattern 4 (slower scan speed) showed larger areas with this maximum current. The maximum current of 10 nA is based on the upper limit of the amplifier. Therefore, I cannot exclude that the different conductivity is caused by tunnelling through the remaining pentacene/precursor layer. Tunnelling should scale exponential with the probe-substrate distance, but for measurements results in the saturation of the amplifier no dependence can be determined.

Following these results I consecutive washed films with patterns prepared using contact mode with chloroform in order to release free standing pillars. Although the patterning process itself seemed to work, I could not demonstrate the consecutive removal of the precursor successfully. All attempts to remove the precursor releasing free standing structures failed, as in all cases the patterned areas were removed, too. Experiments with the bulk annealed films showed, that these films seemed to be stable upon washing with chloroform.

There are several explanations for the removal of the patterned areas: First, due to the short timescales of the experiment and the small contact area between tip and sample, there might not be enough heat transferred between the tip and the sample to convert all precursor material from the surface to the interface. I reduced the film thickness down to 20 nm which is in the range of the calculated maximal film thickness, but patterns on these thin films were removed completely, too. As already, discussed the thermal conductivity of the silicon is much better than the thermal conductivity of the precursor or the pentacene, thus a tremendous cooling via the substrate is expected (Figure 14). These effects add up, thus the temperature down in the layer is insufficient to cause decomposition. Therefore residues of precursor material remain beneath the formed pentacene layer. This thin precursor layer will be dissolved in the solvent and the formed pentacene will be washed away as there is no bonding between pentacene and the silicon wafer. These considerations indicate two possible solutions: Even thinner precursor films and/or the utilization of a heatable stage.

Second, although pentacene should not solve very well in chloroform, the patterned areas are in the size of few square micrometers with a thickness of few tens of nanometer, so the amount of material is very small. Small amounts of pentacene might be dissolved in the huge excess of solvent used to wash away the precursor. This issue can be solved by using cooled chloroform or chloroform solution saturated with pentacene itself. However, using chloroform cooled in the fridge and chloroform saturated by stirring it with pentacene for 30 minutes followed by filtration led to a complete removal of the film, too.

Third, even in the case of pentacene formation across the whole thickness of the film, the adhesion between pentacene and the surface might be so weak, that the pentacene is just physically washed away without being dissolved. The first approach to solve the issue of complete removal was investigating different substrates, as the different surface properties might lead to better adhesion of formed pentacene on the surface. I tested mica and silicon wafers (i.e. SiO_x surfaces), although those surfaces would not allow direct c-SPM measurements. Also on these surfaces the removal of only the precursor could not be demonstrated. HOPG was tested as a substrate as well, but the spincoating of the precursor did not result in homogenous films.

5.1.2 Outlook

I want to present two other approaches which could lead to a successful demonstration of freestanding structures, which did not fit into the scope of my PhD but should be addressed in the future. The first idea is to place the samples on top of a heatable sample stage and heat this stage to a temperature close to the decomposition temperature of the precursor. By this substrate heating, the temperature difference between sample temperature and decomposition temperature becomes smaller, thus less heat needs to be transferred from the heated tip to the sample in order to achieve a complete decomposition of all precursor molecules in the patterned area. This should avoid precursor residues beneath the formed pentacene.

In order to prepare this experiment, a second TGA experiment with the precursor was performed. In this long term experiment the temperature was ramped quickly to 100 °C and was then kept constant for 240 minutes. In consecutive steps, the temperate was ramped by steps of 10 °C and each temperature was kept constant for 240 minutes. The final temperature was set to 140 °C. The total mass loss was about 20 %, comparable with the mass los observed in the first step of the fast experiment. For a temperature of 100 °C a mass loss of about 5% was observed during the 240 minutes. As the patterning experiment will take much less than 240 minutes, a substrate temperature of 100 °C should not lead to considerable decomposition of the precursor, but should help to reach a complete decomposition in the patterned area induced by the heatable tip.

I also started experiments using a bilayered approach: A thick sublayer spincoated from aqueous PEDOT:PSS solution covered by a thin pentacene-precursor layer on top of it. PEDOT:PSS films are conductive, thus conductivity measurements should be possible. The formed pentacene should attach better to other organic materials than to silicon or gold. And last, the PEDOT:PSS layer can act as thermal isolation layer, avoiding the cooling of the patterned area via the substrate. Patterning of

structures into these bilayers was performed successfully at 200 °C and tip speeds of 2 µm/s in contact mode. However, the removing step has not been tested successfully up to now. Therefore this approach should be fully tested in the future.

5.2   Main findings

- Patterning of the pentacene precursor 13,6-N-Sulfinylacetamidopentacene was in principal successful. Topography and conductivity differences between patterned and non-patterned areas were observed.

- The amount of decomposed precursor material depends strongly on the contact time between hot tip and surface.

- The consecutive removal of residual precursor led to a removal of the patterned areas. Therefore, the goal to yield freestanding conductive structures was not achieved until now. Main reasons for the unsuccessful removal step are remaining precursor beneath the formed pentacene, solution of pentacene in the solvent excess and low adhesion between pentacene and substrate.

6.   Thermomechanical investigations on bilayers

Ultra high density data storage [97, 98] or nanoscale lithography [3] based on SPM attracted most attention in the recent past [9, 99, 100]. The basis for thermomechanical probe data storage as well as for thermomechanical probe nanolithography is nano-embossing. The information or structures are engraved into a deformable medium – typically a polymer - using a hot scanning probe microscope (SPM) tip of nanometer scale radius and applying a defined load. The yield strength of the polymer is locally exceeded and permanent indents are created. The lateral size of the contact is set by the required data storage densities of about 10 Tbit/in^2, which translates into indent geometries of less than 5 nm radius. To achieve an indent depth of several nm, the tip's apex radius should be~ 5 nm according to (Eq 1). Having a contact area of smaller than 64 nm² (for a density of 10 TBit/in²) requires minute forces of 10 nN to produce contact pressures higher than 100 MPa, exceeding the yield stress of common polymers, e.g. PS. However, due to the short contact times a shift to higher values is expected.
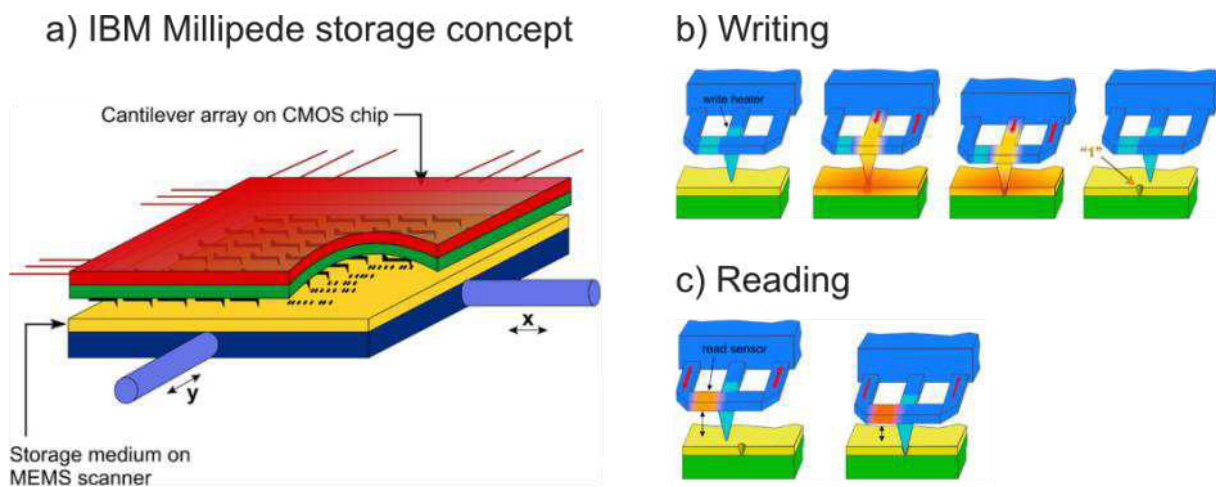

Figure 27: Concept of the IBM Millipede SPM based data storage device (Modified from http://www.zurich.ibm.com/st/storage/concept.html [101]). a) Array of cantilevers operated in parallel to emboss and read data into a medium mounted on an x-y scanner. The array increases data transfer rates due to high parallelization. b) Writing data with heated tip. c) Reading data using thermal height sensing.

In the "Millipede approach" (Figure 27), the SPM tip is pulled into the material using electrostatic excitation, thus applying a voltage between the tip and a conductive substrate beneath the polymer. This substrate is made from highly doped silicon. Simultaneously, a joule heater above the tip is heated by applying a heating voltage. The tip reaches the desired temperature almost immediately, and is pulled into the surface by the electrostatic forces, embossing a single indent in the polymer

(Figure 27 b). One of this writing impulses consisting of a heating and an excitation voltage pulse has a duration of a few microseconds. In order to achieve acceptable data transfer rates, arrays of cantilevers are used (Figure 27 a). In the most recent device an array of 64 x 64 cantilevers, in sum 4096, are operated in parallel [12].

To read back the written information in SPM based data storage, the surface is scanned using the same tips used for writing. This scanning is done with the tip in contact to the surface. As a feedback the changes in resistivity of a heating element, which result from changes in its temperature due to the dependence of heat transfer rates on the distance between surface and heater (thermal height sensing as described in chapter 2.3) is used [57] (Figure 27 c). Thermal height sensing is used because sensing the deflection of the cantilever using the optical lever principle would require a laser and a photodiode for every cantilever in the array which would make the whole device more complex, big and expensive. Cantilevers with integrated Joule heaters for writing and height sensing can be manufactured with existing technology from silicon based electronics production.

6.1   Advantages of bilayered materials

To keep the forces and temperatures needed to indent the medium as low as possible, a soft medium which indents easily at low temperatures would be required. Using low forces and temperatures would keep tip wear as low as possible to guarantee that the size of the indents and the precision of reading would not change during the life time of an SPM based storage device. Concerning these aspects, for example, polystyrene (PS) films should be suitable storage media, owing to its low glass transition temperature T_G of 100°C. A tip temperature of 100 °C is easily achieved, and indenting PS at temperatures higher than 100 °C should be possible at low forces. However, because of the short time scales of indenting, the glass transition temperatures may be shifted to considerably higher temperatures. PS is hydrophobic which is desirable as the water films formed on hydrophilic materials can lead to increased tip wear [102]. On the other hand, on soft materials, like PS, scanning in contact mode (Figure 28a) leads to the formation of ripples [22, 103], which are detrimental for all sorts of applications, but especially for data storage. Furthermore, surface rippling is strongly temperature dependent following an exponential activation law [104]. Any topography information that is written in the polymer layer would be lost after several read-back scans of the same area (Figure 28b). Also, when the heated, thus soft, PS sticks to the tip upon retracting, undesired structures are formed.

To prevent such effects, high crosslinking of the storage medium was proposed and explored [105]. However, a high cross-link density of the polymer leads to an inevitable high-temperature shift and broadening of the glass transition and to an increase of the elastic modulus of the polymer, which makes the writing process more difficult and can lead to an increased tip wear. From an SPM based data storage perspective, the conflicting requirements of high surface toughness and ease of writing are difficult to reconcile in homogeneous polymers [106]
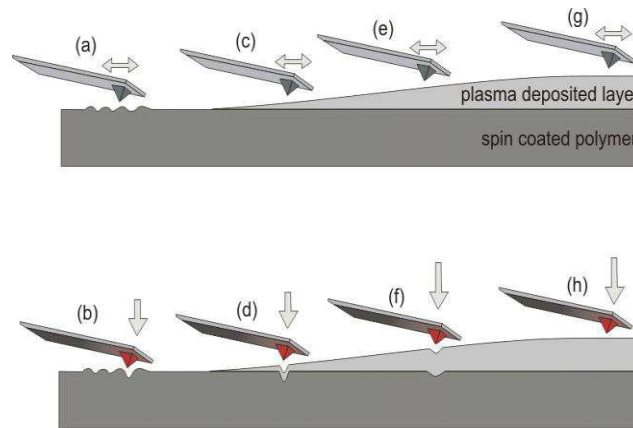

Figure 28: Bilayered material for data storage application. Upper row: Reading, Lower row: Writing

These difficulties can be potentially avoided by resorting to a bilayered material consisting of an easy to indent storage layer and a protective coating (Figure 28). Assuming that macroscopic principles can be applied [107], the properties of the coating can be tailored in a way that the plastic deformation required for permanent data storage nucleates in the substrate polymer, close to the interface to the coating. The coating can be optimized for reading purposes, i.e. to minimize friction and to carry the loading force during read-back scans without causing plastic deformation of the system (Figure 28 c, e, and g). The coating can also be optimized to be hydrophobic, whereas the sublayer can then be made from a hydrophilic material, should a different hydrophobicity of sublayer and protection layer be required. In addition, for the sublayer cross-linking is no longer required, which means that the polymer for the sublayer can be chosen from the wealth of (commercially) available polymers. The sublayer properties can be optimized to find the best combination of softness, glass transition temperature and retention capabilities of stored data [108].

Summarized, the coating needs to provide additional functionality, in this specific case increased resistivity against nanomechanical wear and hydrophobicity [102], but must not alter the mechanical properties regarding indentation of the sublayer. For data storage application, the protective layer must have a root mean square roughness of less than 1 nm per µm² (Figure 28 c and d) to preserve

the smoothness of the surface which directly determines the signal to noise ratio for data storage applications. [28]. The protective layer must not dewet nor delaminate from the sublayer during the lifetime of the device, which can happen, when the plastic deformation is nucleated at the interface between two layers [107]. The protective layer needs to be flexible and non-brittle in order to easily follow the indents embossed into the sublayer and still maintain a closed film. The formation of cracks or holes in the protection layer would reduce its lifetime significantly [8]. The protection layer material should not melt or yield during the writing to avoid the formation of holes in the layer. For protection layers, which are stable solids during at the writing conditions, tip contamination is reduced, as no melted material is in direct contact with the writing tip. Finally, the thickness of the protection layer should be as thin as possible in order to allow thermomechanical indentations at low temperatures and forces (Figure 28 d), i.e. not to change the thermomechanical properties of the sublayer. Increasing the protection layer thickness (Figure 28 f) is associated with an increase in temperature or force required to indent into the polymer layer to the same depth. In addition, the lateral size of the indents become larger thus increasing the minimum possible distance between two indents (Figure 28 f). Further increasing the protection layer thickness (Figure 28 h) would exceed the maximum applied loads that can be used for thermomechanical loading, rendering indentation of the sublayer impossible. For the reading, the thickness of the protection layer is less important, as long as the protection layer stays as a closed film and follows the topography of the sublayer (Figure 28 c, e, and g).

The goal of our joint project with the IBM research Laboratory Rüschlikon (Zurich, Switzerland) was to develop a suitable storage medium for IBM's SPM based data storage system "Millipede" [11, 13]. Plasma polymerization is a convenient way for the deposition of thin and highly crosslinked, thus wear stable films [22]. Thin plasma polymer layers should not increase the surface roughness of the sublayer too much. Thus, the use of a thin plasma polymer layer to protect a soft sublayer made of a spincoated polymer is a promising concept which will be discussed in the following chapter.

6.2   Material preparation and characterization

The decision, which polymers to use for the two layers of the bilayered stack was based on several considerations. For the sublayer, I wanted to use a well characterized polymer which can be easily spincoated in order to form homogenous, smooth films with a thickness of ~ 100nm. The polymer should have a low T_G for easy indentation and should show a clear wear behavior upon nanomechanical wear. The reason for the latter is that, to demonstrate the functionality of a

protection layer, the protected film itself should show wear in order to have clear differences in the wear behavior with and without the protection layer. A low T_G of the sublayer is of particular importance in a bilayered system, as the protection layer will inevitably act as thermal isolator. Thus, higher tip temperatures will be needed in order to intend the sublayer. For these reasons, we decided to use polystyrene (PS) for the sublayer. PS is known to show a clear rippling wear behavior [22, 49, 55, 109-111] and has a comparably low T_G of 100 °C. PS can be spincoated from toluene solution, is well described in literature and is available in different molar masses. PS spincoated on silicon wafers exhibits a very low RMS roughness, the formed films are homogenous and do not dewet from the substrate.

For the protection layer we wanted to use a monomer that will lead to a hydrophobic surface. Therefore, all commonly used monomers that contain oxygen like hexamethyldisiloxane (HMDSO) cannot be used. Another consideration was that the plasma power during deposition should be as low as possible in order to avoid sputtering, and therefore roughening, of the sublayer during the deposition process. This roughening of a soft layer during deposition of another layer using high power plasma was for example observed for the plasma deposition of HMDSO [74]. A roughening of the sublayer surface, which becomes the interface between sublayer and protection layer might negatively influence the formation of indents in the sublayer during the thermomechanical writing. Styrene was used as a monomer for plasma deposition in previous work [22] and yielded in smooth polystyrene (PS) films. In order to achieve wear stable films, a plasma power of at least 120 W had to be used. Films deposited at lower powers still showed considerable rippling wear [22]. Plasma polymerized PS might have a similar T_G than the conventional polymerized PS which is a problem as that would mean that the protection layer will melt during the indentation, possibly causing holes in the layer and contamination of the writing tip with material from the protection layer. One idea would be to form Teflon like films, by using tetrafluoro cyclobutadiene (C_4F_4) as a monomer for the plasma process. Teflon has a high melting temperature of 330°C and is known to be hydrophobic, which is why it is used commonly for antisticking purposes. Although the use of C_4F_4 monomers as precursor gases for forming a hydrophobic protection layer is tempting, Teflon layers lack good mechanical stability and are very sensitive towards mechanical wear, due to the weak bonding between Teflon and the given substrate. For applications like frying pans this disadvantage is overcome by roughening the metal substrate and applying the Teflon coating using high pressure in order to physically bind it to the substrate. But this approach is not suitable for systems, where the surface roughness must not be changed by the coating process. Therefore, we proposed the use of norbornene (C_7H_{10}), a bridged cyclic hydrocarbon. The high ring tension of this molecule should lead

to strong fragmentation and formation of radicals during plasma deposition at lower powers than for the aromatic, thus stable, styrene. Radicals formed during the plasma deposition from styrene and other aromatics are stabilized by the delocalized π-electron system of the aromatic and are therefore less reactive. Radicals formed from norbornene are less stabilized and are thus more reactive. Therefore, even at low plasma power deposited films of plasma polymerized norbornene (ppNb) should exhibit stronger crosslinking and thus a higher nano-wear resistivity than plasma polymerized PS. For the same reason, the ring tension in the bridged ring with a double bond, norbornene should be more reactive than simple aliphates like methane or propane, which have been successfully used for plasma polymerization. Conventional polynorbornenes, usually produced using Grubb's catalysts in a ring opening metathesis polymerization (ROMP), show a high glass transition temperature or melting points, which can reach up to 400 °C [112, 113], depending on the polymerization process. The expected high glass transition temperatures are much higher than the T_G of 100 °C reported for PS, so the ppNb protection layer should not melt or yield during the writing process. Despite these promising properties, the use of norbornene for a plasma deposition process was not reported so far.

6.3 Surface stability

6.3.1 Nanowear behavior

In a first experiment we tested the wear resistivity of both materials, spincoated PS and plasma polymerized norbornene (ppNb), separately. For the test, a 3 µm x 3 µm area was scanned hundred times at an applied load of 10 nN and a tip velocity of 50 µm/s. Then, a 5 µm square with the test area in the middle was imaged. The results of the wear tests on unprotected PS were used as a reference in order to judge the beneficial effects of the deposited ppNb layer. ppNb was tested to verify that our assumptions regarding its suitability for the plasma deposition process were correct. Especially we wanted to find out, whether the plasma polymerization of norbornene leads to stable films at lower powers than the plasma polymerization of styrene. Therefore I also compared the results of the nanowear tests on spincoated PS and ppNb with the results obtained by Berger et. al. on plasma polymerized PS (Figure 29). As expected and known from literature [22], the spincoated polystyrene showed a considerable surface wear (Figure 29). The surface in the tested area showed an RMS roughness which is increased by 360 % compared to the non-tested area around. The characteristic wavy or rippling pattern was clearly observed. Compared to the spincoated PS, the plasma polymerized norbornene PS deposited in pulsed mode at 80 W (taken from [22]) exhibited

reduced, but still pronounced rippling wear. This reduction was explained with increased crosslinking in the film. The ppNb, even though deposited in pulsed mode at 50 W did not show any change in surface roughness or topography at all, despite the fact that the deposition power was lower than for styrene (Figure 29). The next step was to investigate, whether the deposition of a thin (5 nm to 20 nm) ppNb layer on top of a thick (~100 nm) PS layer will significantly reduce the surface nano-wear. Upon succeeding with the fabrication of nano-wear resistive stacks, these stacks were tested concerning their indentation properties.
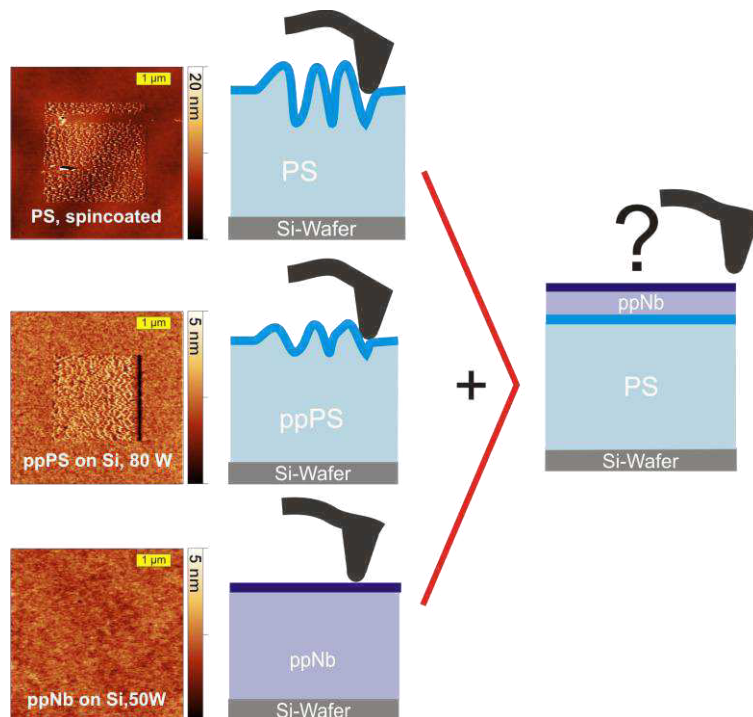

Figure 29: SPM wear test on a non-crosslinked, spincoated (up) PS sample, a crosslinked (middle) PS sample deposited using plasma polymerization at 80W [22] and a crosslinked (down) ppNb sample deposited using plasma polymerization at 50W. The non crosslinked PS sample shows a periodic "ripple" pattern, which is considerably reduced for the plasma polymerized PS sample. The plasma deposited norbornene film showed no surface modification. In order to protect wear sensitive materials like PS, a thin layer of wear resistive ppNb was deposited on top of the wear sensitive material and the wear behavior was investigated.

The wear test on a layered system made of PS covered by ppNb deposited at 50 W in pulsed mode (t_{on} = 20ms, t_{off} = 50 ms) revealed an increase in RMS roughness of 130 % (Figure 30 left). This roughness is lower than the increase measured on unprotected PS (360 %), but still much too high for thermomechanical data storage.

Despite the fact that the ppNb protected PS was more wear stable than non-protected PS, there was a big difference between the behavior of the ppNb layer on a Si-wafer on one hand and on PS on the other hand. This different behavior of ppNb on different substrates, although deposited using identical deposition parameters, indicated that the substrate and its interface to the ppNb layer played a crucial role in the appearance in nano-wear.

Influence of t_{on} and t_{off} ratio on the nano-wear resistivity

The first attempt to increase the wear-resistivity was to keep the deposition power constant at 50 W and increase t_{on}. A higher percentage of t_{on} time might lead to more fragmentation and radical formation, which could yield in higher crosslinked or better anchored ppNb layers. On the other hand, a higher percentage of t_{off} times would give the formed fragments more time to react with the PS surface, and might lead to more bonds between both layers. The nano-wear tests on stacks made of PS and ppNb deposited at 50 W using different pulse parameters (Figure 30) revealed, that all stacks exhibited nano-wear in different degrees. A larger rate of t_{on} time reduces the nanowear, while a larger rate of t_{off} time did not change the nanowear considerably. Thus, more fragmentation and radical formation is the critical parameter for gaining a more wear resistive stack. The recombination of the fragments formed in the plasma is so fast, that even short t_{off} times are sufficient for the deposition of smooth, homogenous films (Figure 30).
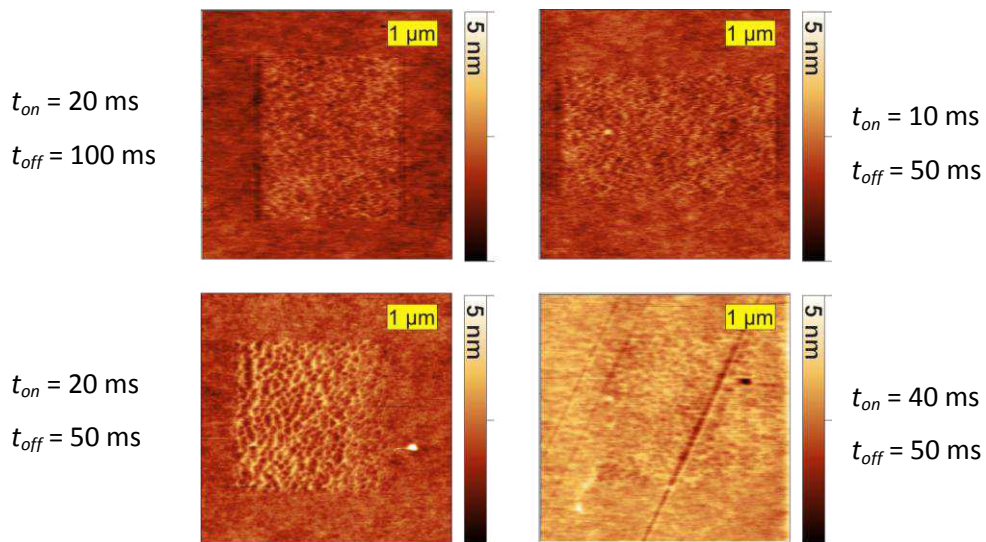

Figure 30: Nano-wear of a bilayered stack consisting of spin cast PS and ppNb deposited at 50 W in pulsed mode. The pulse times were modified. Although all films showed nano-wear, the nano-wear was slightly reduced for higher percentages of t_{on} times. Increasing the t_{off} time relative to the t_{on} time did not have a beneficial effect.

Influence of the plasma power

The fragmentation and radical formation is the crucial step in the deposition of wear resistive ppNb layers. In the next step, I kept the pulse duration constant at t_{on} = 20 ms and t_{off} = 50 ms and deposited ppNb at higher powers (Figure 31). Higher plasma powers should then lead to more wear resistive stacks, which was confirmed by nano-wear tests (Figure 31). Although higher deposition powers reduced the nano-wear, which was again quantified by the change in RMS roughness in the tested area (Figure 32), nano-wear was still clearly observed even at the maximum deposition power of 150 W. Depositing ppNb in pulsed mode (t_{on} = 20 ms, t_{off} = 50 ms) at 150W resulted in films showing an increase in RMS roughness of 40 % after the tested area. Although this result is better than for ppNb deposited at 50 W and much better than the results on unprotected PS, even this reduced wear is too much for data storage applications
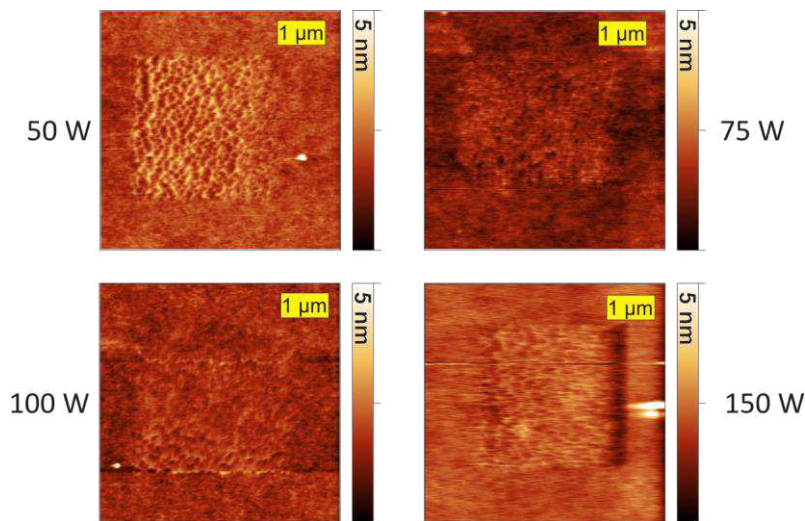

Figure 31: Nano wear of a bilayered stack consisting of spincoated PS covered by ppNb deposited at different powers in pulsed mode (t_{on} = 20 ms, t_{off} = 50 ms All films show considerable surface wear, although ppNb deposited at 50 W on Si-wafers was wear stable. The wear is reduced for increased plasma powers.

Continuous mode deposition

The results from nanowear tests on stacks made of PS and ppNb deposited using 50 W and different pulse modes and stacks made of PS protected by ppNb deposited using constant pulse mode and increasing deposition power (Figure 30 and Figure 31) indicated that a high ratio of t_{on} times to t_{off} times and high deposition powers for the ppNb layer increase the wear resistivity of the stack. In a last attempt to gain wear resistive stacks I increased the t_{on} to the maximum, i.e. operated the plasma reactor in continuous mode.
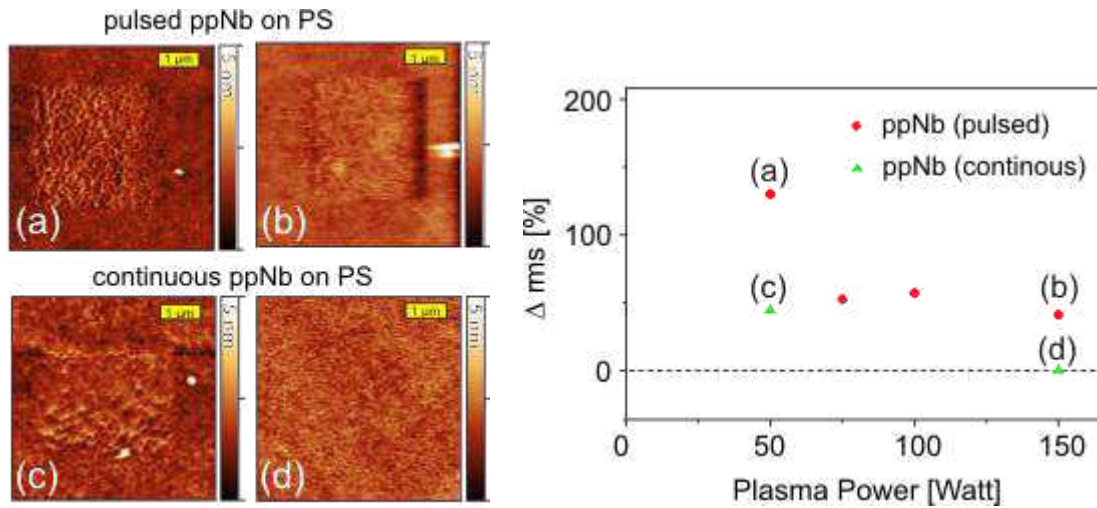
Figure 32: Wear experiment on stacks made of spincoated PS and ppNb deposited at different parameters. Comparison of a) PS + ppNb (50 W, pulsed mode), b) PS + ppNb (150 W, pulsed mode), c) PS + ppNb (50 W, continuous mode), c) PS + ppNb (150 W, continuous mode). Only stacks made of PS protected with ppNb deposited at high plasma powers and in continuous mode did not show any wear.

ppNb films on PS deposited at 50 W in continuous mode showed an increase in RMS roughness of 45 % in the tested area, which is almost as low as the values observed for ppNb deposited in pulsed mode at 150 W (Figure 32). Upon increasing the plasma power in continuous mode to 150 W, wear stable ppNb layers were formed on PS (Figure 32). The stacks neither showed changes in RMS roughness nor in height in the tested area. Therefore the stacks were further investigated as promising candidates for thermomechanical data storage.

As it is known that high deposition powers may lead to an increase in interfacial roughness [74], I used XRR measurements to gain insight into the interface roughness between the two layers.

XRR measurements (Figure 33) revealed that the PS-ppNb interfaces roughness (0.90 nm) after the plasma deposition was higher than the roughness of the pristine PS surfaces (0.6 nm) that was determined before the plasma deposition process. For some PS films, the PS roughness before the deposition was as low as 0.48 nm, while after the deposition of ppNb in continuous mode at 150 W the PS-ppNb interface roughness was again 0.9 nm. The surface of the ppNb film showed a lower roughness of 0.40 nm to 0.90 nm, which was in all cases lower or equal than the roughness of the corresponding interface. These findings are in accordance with the work of Zhang et. al [74].
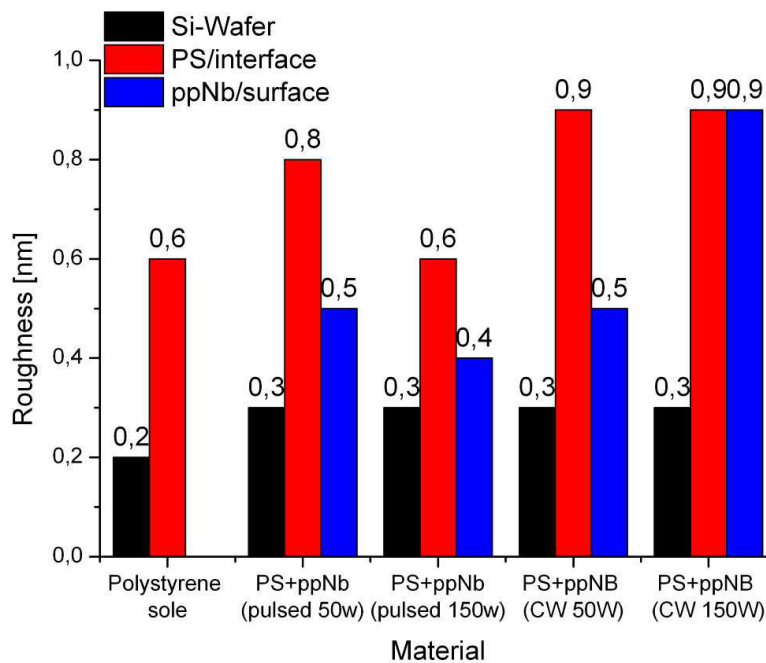
Figure 33: Interfacial and surface roughness of different PS-ppNb stacks determined using XRR measurements. The roughness of the PS is increased during the plasma deposition of ppNb. The ppNb surface exhibits roughnesses equal or smaller than the interfacial roughness. The silicon substrates roughness did not change during the deposition, as expected.

We associate the roughness increase in our samples to sputtering processes in the beginning of the plasma deposition process. The effect is more pronounced for the films deposited in continuous mode.

6.3.2 Origin of the nano-wear on PS-ppNb stacks

Nano-wear on polymer surfaces can originate from different mechanisms (chapter 2.2.2). Stick-slip mechanism, the accumulation of polymer chains in front of the moving tip ("molecular broom") [20, 24], would lead to nano-wear without an increase of the height in the tested area, as no material is added or removed from the zone. Crack propagation inside the polymer [23] or delamination of the ppNb layer from the PS sublayer [55] would lead to nano-wear with increase of the average height of the tested area due to the fact that the volume is increased.
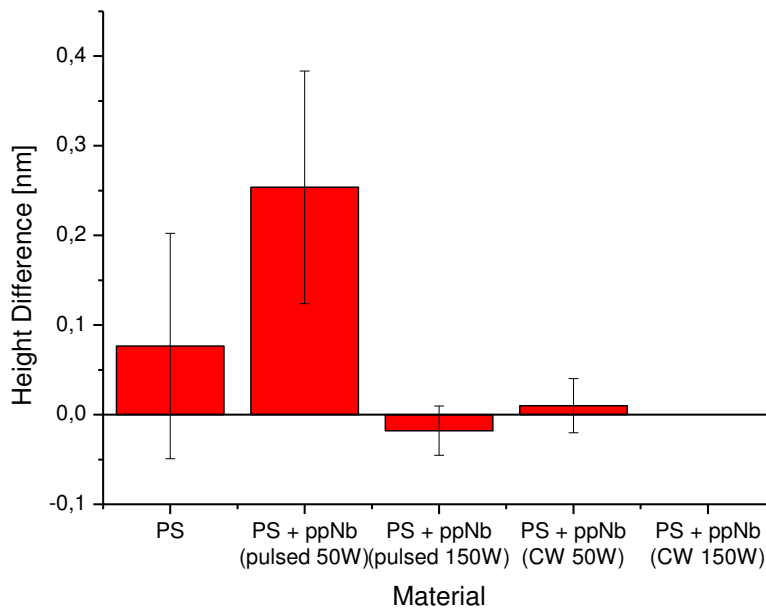
Figure 34: Height difference between patterned and non-patterned areas on blank PS and PS covered with ppNb at different plasma deposition parameters. Only for PS covered with ppNb at 50W in pulsed mode, a significant height difference was measured.

In the case of delamination the sample material is peeled by the SPM tip forming bundle structures [23]. Crack propagation is process similar to delamination. Again, the moving tip pushes the polymer ahead in its moving direction. Instead of peeling the material, the induced constraint is released by the formation of a crack under the tip [23]. This crack propagates in moving direction in front of the tip, leading to a reduced density in the bulk material in the worn area, thus leading to an increased average height. The ppNb surface exhibited different nano-wear resistivity depending on the substrate. In order to analyze whether different mechanisms caused the observed substrate dependence of the nano-wear, I analyzed the height difference between the tested and the non-tested area [55] (Figure 34). For this analysis I determined the average height in the tested area and the average height of the not tested area. By subtracting the values I calculated the average height difference. For unprotected PS I did not find any distinct increase in the height of the tested area, so the stick-slip mechanism can well explain our findings on PS, which would be in accordance with the work of Dinelli et.al. [111].

However, there is another model, which can explain the experimental results: Instead of assuming the movement of loose material or polymer chains on the surface, we sketch a mechanism involving direct plastic deformation of the polystyrene. We have sketched the stick-slip mode by assuming a defined normal load F_N of the SFM-tip against the sample surface (Figure 35 a).
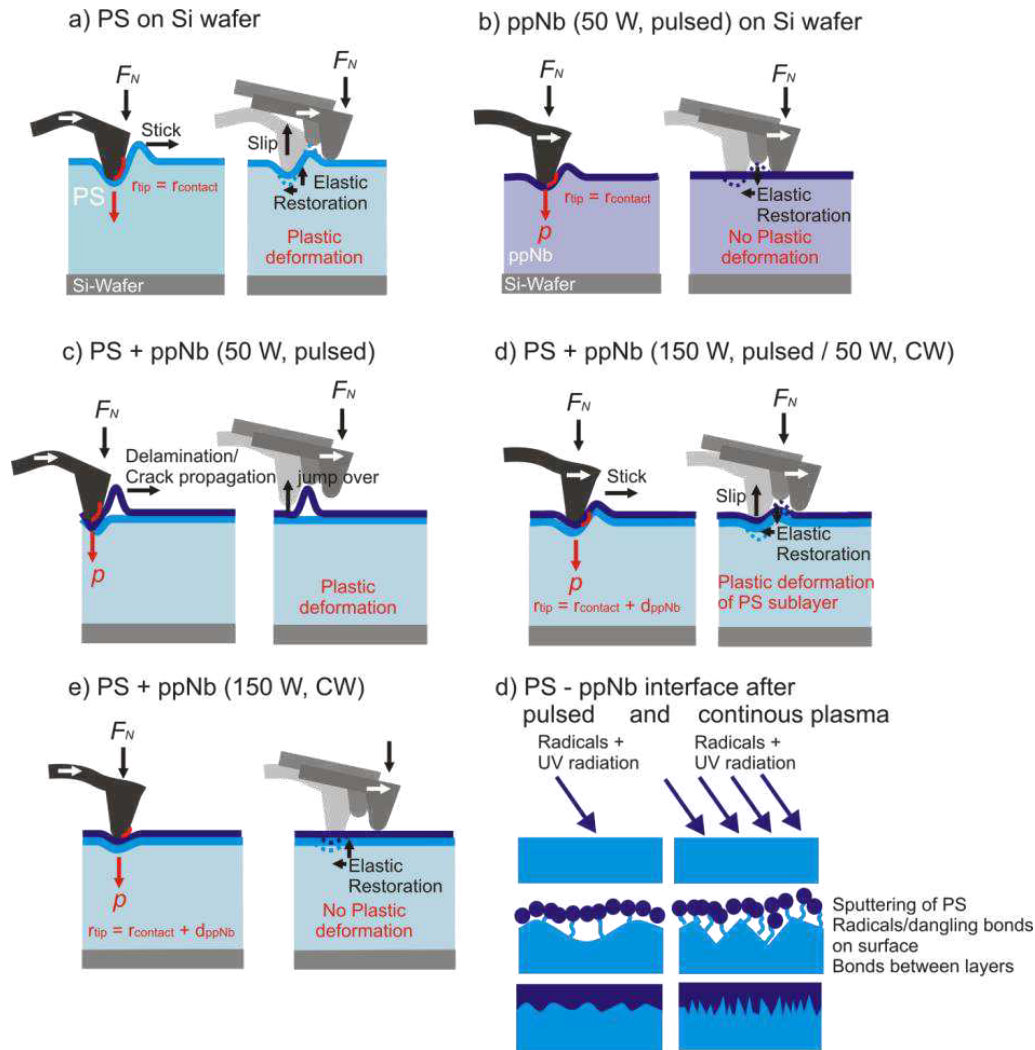
Figure 35: Schematics of the observed wear effects on different samples: a) Unprotected PS: considerable nano-wear but no increase in height due to a stick-slip mechanism or direct plastic deformation b) plasma deposited norbornene on silicon: no nano-wear due to high crosslinking c) ppNb in pulsed mode at 50 W on polystyrene: nano-wear and increased height in the patterned area due to delamination. d) ppNb in pulsed mode at high powers or in CW mode at low powers on PS: nano-wear but no increased height due to bonding between PS and ppNb. e) ppNb at 150W in continuous mode on PS: no nano-wear due to strong bonding between the PS and the highly crosslinked ppNb. f) Differences of interfaces between substrate and plasma polymer deposited in pulsed or in continuous mode. In continuous mode more sputtering increasing the interfacial roughness takes place, but also an increased number of bonds are formed.

a) Nano-wear on unprotected PS films

The PS surface is deformed by the tip with a radius R. The radius a of the contact area can be calculated using Hertz model with *R* being the tip's radius, *v* the Poisson's ratio and *E* the Young's modulus of the sample:

$$a^3 = \frac{3}{4} \frac{R(1-v^2)}{E} F_N \qquad \text{(Eq 12)}$$

For an applied force F_N of 10 nN, a tip radius R of 10 nm, a Young's modulus E of 3 GPa for PS, and Poisson's ratio v of 0.3, the contact area has an radius a of~ 3nm (Eq 12). The pressure p under the tip can then be calculated using the applied load F_N and the contact area:

$$p = \frac{F_N}{a^2 \pi} \qquad \text{(Eq 13)}$$

In addition to the normal force pressing the tip into the surface, there is also a tangential force as we move the tip across the surface. This shear stress can be calculated using a model introduced by Mindlin et. al [114]. Assuming a contact area with radius a, the distribution of shear stress σ in this area can be calculated using:

$$\sigma = \frac{3\mu F_N}{2\pi a^3} \sqrt{a^2 - r^2} \qquad \text{(Eq 14)}$$

Here, μ is the friction coefficient, and r is the distance of a point from the center of the contact area. The tangential traction is maximal at for r = 0, i.e. in the center of the contact area (Eq 14).

Using (Eq 13) and (Eq 14) we can calculate the maximal shear stress σ_{max} in the center of the contact area. F_N is 10 nN, R is the approximate tip radius of 10 nm, the Young's modulus E of PS is 3 GPa, and the Poisson's ratio v assumed as 0.3. With this values we calculate a stress σ_{max} of 595*μ MPa. The friction coefficient of a silicon SPM tip moving across a PS surface was reported to be ~0.46 [115], determined with friction force microscopy (FFM). Macroscopic experiments resulted in friction coefficients between 0.3 and 0.5 for silicon sliding over PS [116]. Even with the lowest value of μ = 0.3, (Eq 14) results in a shear stress of 178 MPa which would exceed the yield strength of PS, and could thus cause plastic deformation. Plastic deformation can take place very easily when raster scanning an polymer using a scanning probe microscope, but the tip induced wear is usually not observed immediately but only after a few scans. A few considerations concerning the time and length scales of the experiment have to be made to explain that nano-wear is seldom observed after the first scan. The tip is only in very short contact which each position of the polymer. Assuming a tip radius of 10 nm, a scanned area of 3 µm and a scan rate from 1 Hz (1 line/second), the tip moves with a speed of 6 µm/s, which means that every section in size of the tip (10 nm) is only in contact with the tip for 1.7 ms. According to the time-temperature superposition principle, the yield behavior of

the polymers at short time scales can well differ from the yield behavior observed on experiments with a duration of several 100 s. The yield stress may well shift to higher values when reducing the experiments timescale down to ms. Furthermore, macroscopic experiments probe, due to large size of the probe, a whole ensemble of polymer chains. In our experiment, the radius of the tip is of the same size as the radius of gyration of a single polymer chain. The behavior of single chain upon stress may differ from the behavior of bulk material. Especially, a single chain may recover a substantial part of tip induced displacement.

b) Nanowear on ppNb (pulsed mode, 50 W) deposited on silicon

In the case of low friction materials or materials that only elastically deform, temporary lumps are generated (Figure 35 b). A very low friction coefficient reduces the tangential forces below the force needed for plastic deformation (Eq 14). For highly crosslinked polymers the yield stresses needed for plastic deformation are too high to be reached during the experiment. The temporarily formed lumps can fully elastically recover leaving no plastic deformation behind (Figure 35 b, right side). Similar behavior is observed for a rubber sphere pushed along a hard surface or a rubber surface indented with a hard sphere and has been described as "Schallamach waves" [47, 117]. We find this behavior for ppNb that was deposited on a Si-substrate using a pulsed plasma power of 50 W (Figure 35 b).

c) Nanowear on ppNb (pulsed mode, 50 W) deposited on PS

The analysis of the difference in average height between worn and non-worn areas for ppNb deposited in pulsed mode (t_{on} = 20 ms, t_{off} = 50 ms) at 50 W plasma power on PS revealed a distinct increase of 0.25 ± 0.1 nm This indicates that nano-wear in this case is dominated by crack propagation or delamination (Figure 35 c). To distinguish between crack propagation and delamination, Schmidt et al used the relationship between the height discrepancy and the amplitude of the formed pattern. Schmidt et. al. used the definition of the RMS roughness for their approach. On a SPM image with a mean height of zero, he RMS roughness RRMS of the tested area is given as the standard deviation in height along m periods with a wavelength λ of a sinusoidal wave [55]:

$$R_{RMS} = \left[\frac{1}{m\lambda} \int_0^{m\lambda} A^2 \sin^2\left(\frac{2\pi}{\lambda} X \right) dX \right]^{1/2} = \frac{\sqrt{2}}{2} A \qquad \text{(Eq 15)}$$

Neglecting height variations not caused by nano-wear, the amplitude of the "waves" caused by nano-wear is equal to $2^{1/2}$RMS. For delamination, the height difference between the tested area and the

reference area should then equal $2^{1/2}$RMS of the tested area. For crack propagation, a different relation is expected [55]. Of course, this approach is only valid for materials which exhibit a sinusoidal pattern during nano-wear and assuming that the thickness of the layer does not change during delamination. I was not able to determine a distinct wavelength and amplitude for our patterns or to describe the patterns using a sinusoidal wave (Figure 30). Thus we attribute the observed rippling in the stack made of a 50 W ppNb film on PS to either delamination or crack propagation mechanism. Future experiments can help in distinguishing between both mechanisms, for example one method to directly prove the existence of delaminated parts or cracks would be ultrasonic force microscopy in combination with scanning force microscopy [52]. The most probable location for both crack propagation and delamination causing rippling on ppNb protected PS layers is the interface between the PS layer and the ppNb film. By increasing the binding strength between both layers, crack propagation or delamination should be hindered or even rendered impossible. An increase of deposition power increases the binding strength but yields in an increased interfacial roughness [74].

d) Nano-wear on ppNb (pulsed mode, 150 W, continuous mode, 50W) deposited on PS

The question remains, how the wear of the stacks consisting of spincoated PS and ppNb deposited at 150 W in pulsed mode or at 50 W in continuous mode is caused. There is no observed height difference, so a mechanism based on crack propagation or delamination seems unlikely. The ppNb on Si-Wafer was wear stable, so a stick-slip based mechanism should not occur neither, as it is unlikely that the ppNb's surface properties depend on the sublayer. XRR study suggested that the increase in the interfacial roughness is connected with the nano-wear behavior. The deposition of ppNb at 150 W deposition power in pulsed mode or at 50 W in continuous mode resulted in the formation of more radicals and dangling bonds at the surface of the PS, explaining the higher interface roughness. In addition to an increase of the crosslinking density in the ppNb film, there are more bonds formed between PS and ppNb at the interface between the two layers (Figure 35 f). Thus delamination of the ppNb film from the PS sublayer is suppressed.

In this case plastic deformation in the ppNb protected PS can be the reason for the observed surface wear. While the wear of a simple PS film can be explained with the movement of entangled polymer chains on the surface (stick-slip mechanism), the wear on a PS-ppNb stack has to be caused by plastic deformation of the PS. As there is no direct contact between the tip and the PS, the wear cannot be caused by the movement of PS chains by the tip. Also, the wear is most probably not caused by effects in the ppNb layer, as only ppNb showed to be wear resistive before.

We therefore can use the same calculations we used for the case of a simple PS film in the beginning. However, the contact area between the tip and the PS is layer is increased due to the ppNb protection layer (Figure 35d). A 10 nm protection layer would increase the contact radius a at the PS from 3 nm to 3.5 nm, by using again Hertz equation (Eq 12) and adding the protection layer thickness to the tip's radius resulting in a tip radius R of 20 nm. The pressure at the PS interface would then be 250 MPa (Eq 13), thus considerably reduced compared to the pressure induced by the tip on an unprotected PS film. Using (Eq 14) we can again calculate the lateral stress, assuming the same parameters as for unprotected PS and just assuming an increased tip radius of 20 nm. This results in σ_{max} of 375*µ MPa = 110 MPa, taking a μ of 0.3 into account. This stress is reduced compared to the lateral stress induced in unprotected PS, which was σ_{max} =178 MPa. The plasma deposited ppNb will have another E-modulus, which will most probably be higher due to the increased crosslinking, thus the stress induced in the PS will be additionally lowered. The lower induced stress could explain a decreased magnitude of surface wear which is in accordance with our measurements. The "wavelength" of the observed ripples is increased as the cantilever moves a longer distance, before the feedback system detects the surface modifications. The same model is valid for protective ppNb deposited at 50 W in continuous mode.

e) Nano-wear on ppNb (continuous mode, 15W) deposited on PS

Finally, PS protected with ppNb deposited in continuous mode at 150 W revealed neither an increase in RMS roughness nor an increase in height of the worn area (Figure 34). We attribute this mechanical stability to the strongest bonding achieved in all experiments between the layers and the strong crosslinking in the protection layer. In this case the ppNb layer not only increases the effective tip radius acting on the PS at the PS/ppNb interface, reducing the pressure in the PS substrate, it also resists the applied force due to its high crosslinking, further reducing the deformation of the PS. The strong linking between the layers prevents any delamination or crack propagation (Figure 35 e). The high plasma power and continuous mode operation can lead to a crosslinking of the PS surface itself, increasing the yield stress of the system. Thus in the nano-wear experiment no permanent change in surface topography is visible (Figure 34).

These results show, that nano-wear of stacked systems is an interesting topic which needs further investigations in order to clarify the exact mechanisms which lead to nano-wear. Although the nano-wear-sensitive layer in all investigated systems was made from the same polystyrene, the nano-wear mechanisms differ strongly. The investigations made here imply that further investigations on the wear of unprotected surfaces may be necessary to fully understand the mechanisms. Wear on PS is

still observed when stick-slip mechanism is definitely suppressed by a thin protection layer. The question rises, whether stick slip is really the main nano-wear mechanism for unprotected PS or whether other mechanisms should be considered. As the stacks made of ppNb deposited at 150 W in continuous mode on PS showed the required wear resistivity, only these stacks where further investigated concerning their indentation properties.

6.4 Thermomechanical behaviour of bilayers

Thermomechanical writing and temperature calibration

In order to have reproducible conditions, also for the comparison of the bilayered material with previous tested materials [27, 28, 106, 118], the tests were performed under controlled low humidity, <1%, in a nitrogen atmosphere. For writing, the tip is approached by mechanical means to its rest position at a distance of ~ 50-300 nm above the surface. The tip heater is heated to the writing temperature using a constant voltage excitation. For a write operation, the tip is pulled into contact by applying an electric potential between the conducting Si substrate and the capacitive platform of the silicon cantilever as described in the introduction (Figure 27).

The writing temperature of the heater is determined by measuring a current-voltage (IV) response curve of the heater. The resistance of the heater is plotted as a function of dissipated power. The temperature at which the maximum resistance occurs is a function of the silicon doping density and is known in the literature as inversion temperature [119]. We assume that all of the power dissipated in the cantilever contributes to the heating of the heater structure and that the temperatures change of the heater is a linear function of the dissipated power. For the doping values used here, the maximum resistance occurs at 550°C, and the heater temperature can thus be calculated [120].

The temperature reached in the polymer during a write operation is a complex function of the tip geometry, and depends on the heat resistance of the tip, the heat resistance of the interface between tip and polymer and the polymer's heat-spreading resistance, including the underlying substrate in the case of a thin polymer film (≤ 100 nm). In particular it depends on the contact radius and the opening angle of the tip (20-50 degrees for our tips) [120]. A rough estimation states that the increase in polymer temperature is approximately half the tip heater temperature relative to room temperature [28].

Thermomechanical Reading

The read resistor of the cantilever sensor is heated to ≈ 200˚C using a constant voltage excitation. The thermal time constant of the reader is ~5 µs and the overall noise level corresponds to a 0.1 nm RMS resolution of the tip-sample distance measurement. For topography imaging, an effective load force of ≤ 10 nN is applied. This load is lower than the load applied during my nanowear experiments (10 nN), so no damage of the surface during reading should occur.

6.4.1 Influence of sub and top layer on thermomechanical properties

In order to investigate the influence of the ppNb layer thickness, additional indentation experiments were performed. For reference a blank PS sample and a "bulk" ppNb sample (250 nm thick ppNb layer on PS) were investigated in addition to the two PS-ppNb stacks. The experiment consisted of writing an array of indents using varying applied forces (F_{app}) and temperatures of the tip heater (T). After writing, the topography of the written indents was recorded. The indents were grouped in patterns consisting of 32 lines comprising 200 indents in each line. The indent and line spacing was 40 nm in order to minimize interference. The 32 lines were divided into four blocks of 8 lines. Each 8-line block corresponded to a fixed writing temperature, which varied in equally spaced increments between room temperature, and an upper value of 350°C (for the unprotected PS sample) to 700°C (for the bulk ppNb sample). A subset of the blocks written with the respective highest temperature for each sample is depicted in Figure 36 a-d. The blocks themselves were divided into 4 sub-blocks of two lines. In each sub-block the writing force was constant, and the force was varied between the sub-blocks yielding no visible indents for the lowest force (~ 10 nN) to a remnant depth d_{rem} of ~5 nm for the highest force (up to 250 nN depending on the investigated sample) (Figure 36 a-d). For an exemplary analysis we discuss only the data of the uncoated PS sample in details. For better analysis and understanding, the topography of all written blocks was analyzed in terms of remnant indent depth d_{rem} and inner radius of the indent a (inset of Figure 36 g) at the different applied forces and writing temperatures.

The most straightforward representation of the gained data is a temperature map. Here, exemplarily plotted for unprotected PS, the applied force F_{app} is plotted against the resulting remnant indentation depth (Figure 36 e) for the different writing temperatures. Higher writing temperatures yield in lower F_{app} needed to gain an indent with a certain depth or yield in deeper indents at a given F_{app}, which is in accordance with expectations. Another representation of the data is an indentation map (Figure 36 f), which is a plot of the indentation depth in the force - temperature parameter space. The

contours represent isolines corresponding to indentation depths of d_{rem} = 2, 3, 4, and 5 nm. Similar plots have been measured for all other samples. For all samples we observed that the data points can be fitted with high quality to straight lines. The fitted lines intersect in a single point on the temperature axis at $T_s \approx$ 415°C and at approximately zero force. We identify this point with the softening transition of the sample at which it loses its resistance to plastic deformation. Hence this point corresponds to a point of vanishing yield strength.
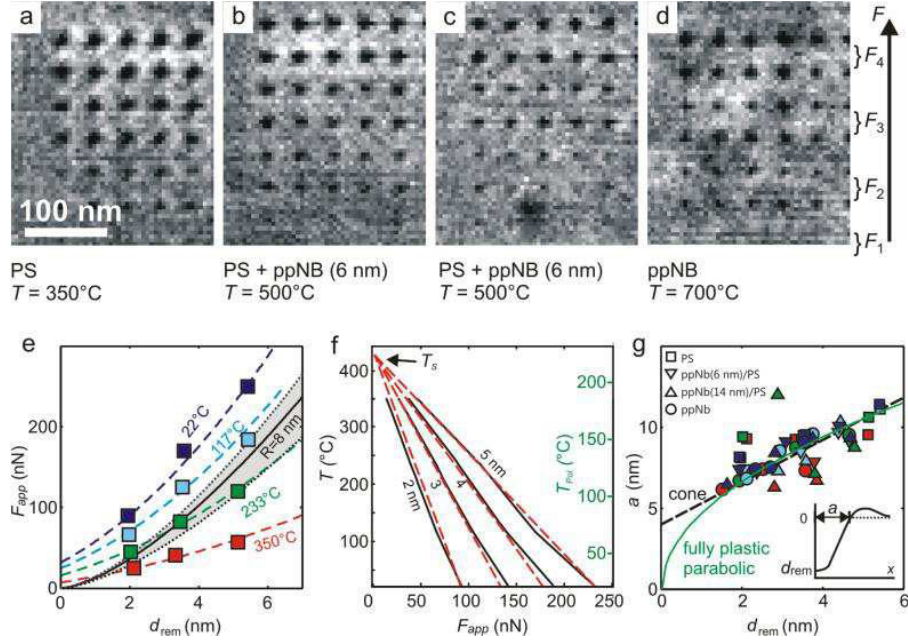

Figure 36: Thermomechanical writing and analysis of the indent data. (a)-(d) Topographic images of indent patterns written on (a) polystyrene, (b) 6 nm ppNb on PS, (c) 14 nm ppNb on PS and (d) bulk like ppNb (250 nm ppNb on PS). Only data for the hottest tip temperatures are shown. The force increases from bottom to top. The analysis of the bit pattern written into the bulk PS sample is shown in panels (e) and (f). (e) Contour plot and (f) scatter plot of the average indent depth as a function of applied force and tip heater temperature. The dashed lines in (e) and the solid lines in (f) represent the results of a global fit of our model to the data. (g) Inner radius _a_ of the indents (sketched in the inset) for all measured indents as a function of indent depth. The solid line is drawn according to the fit parameters obtained from the fit shown in panel (e) and (f).

The yield stress of polymers decreases with the temperature of the polymer [121, 122]. Based on this, we write the following linear Ansatz for the yield stress _Y_ as a function of the polymer temperature T_{Pol}

$$Y = Y_{RT} \left(\frac{T_s - T_{Pol}}{T_s - T_{RT}} \right)$$ (Eq 16)

Here, Y_{RT} is the yield stress at room temperature, T_S the polymers softening temperature and T_{RT} is room temperature. T_S is defined here as the temperature at which Y becomes 0.

The temperature values given in Figure 37 are the values of the silicon heater in contact with the tip. The best way to determine the exact temperature would be either a calibration as described in chapter 3.5.2, but this is difficult to achieve for cantilever arrays. The rise in temperature T_{pol} at the interface is approximately half the temperature difference of the heater T_{heater} to the environment T_{RT} [120], i.e. room temperature (right scale in Figure 36 f):

$$T_{pol} = (T_{heater} - T_{RT})/2 + T_{RT}$$ (Eq 17)

For further analysis, a mean indent shape was evaluated using cross-correlation averaging of the indents written under identical conditions (Figure 36 a-d, F1-F4). The radial profile (inset in Figure 36 g) was determined by an azimuthal averaging procedure assuming a centro-symmetric indent shape. The radial profile was characterized by a remnant indent depth d_{rem} and an inner indent radius a. The latter is defined by the first intersection of the background zero line with the profile which rises sharply from the negative indent depth $-d_{rem}$ to positive values due to the existence of a rim surrounding the indent.

A plot of the inner radius versus the indent depth revealed that all samples showed a similar behavior regardless of the probed system. PS (unprotected), PS protected with different thick ppNb layers, or even bulk ppNb, showed the linear correlation of inner radius with indent depth, within the accuracy of the experimental data (Figure 36 g). The data can be fitted with different models:

a) Self-similarity of nano-indents

In order to compare the new bilayered medium with previous presented media, a model introduced by IBM for other media [26] was used. This model is based on the concept of self-similarity in nanoindentation [26] and predicts that the inner radius a is a linear function of the indent depth d_{rem}:

$$a = a_0 + c\, d_{rem}$$ (Eq 18)

To describe the nano-indent, the geometrical factors a_0 and c are used. The a_0 corresponds to the limit of zero depth while c corresponds to the scaling of indent radius with depth.

(Eq 18) has been observed before for indentations in highly cross-linked PS [26]. Similar behavior is observed for non crosslinked PS, PS protected with ppNb and even for bulky ppNb, indicating, that the observed dependence is true for a wide range of materials. However, the geometrical factors gained from the fit (black dashed line in Figure 36 g) are $a_0 = 4$ nm and $c = 1.3$. These factors are much lower than the ones determined or highly cross-linked polystyrene systems, where values of $a_0 > 10$ nm and $c > 2.6$ were found [26]. The lower values gained for the PS-ppNb stacks indicate that much deeper indents could be written at the same lateral scale for the layered samples. The deeper indents could improve the signal to noise ratio during the reading, thus improving the reliability of the storage system.

b) Full plastic deformation during nanoindentation

The shape of the indents can be fitted equally well with a general model. Assuming a spherical tip indenting a polymer in the fully plastic regime, the contact radius can be calculated using an equation presented by Johnson [123]. For a tip with a spherical end of radius R the inner radius a at a given indent d_{rem} is given by

$$a = \left(Rd_{rem} \right)^{1/2} \qquad\qquad \text{(Eq 19)}$$

Fitting the results with this function (green continuous line in Figure 36 g) led to a tip radius of $R = 10$ nm, which is in the expected range.

There is no difference between the qualities of the two presented fit functions in the range of our experimental data. For smaller indent depth and thus smaller indent radii there would be a deviation since the model proposed by IBM [26] predicts a linear behavior while the model by Johnson [123] predicts a square root behavior. In order to prove one of the models over the other, i.e. showing the contribution of elasticity, smaller indents would need to be written and analyzed in future experiments.

6.4.2 Comparison of nanoscale and macroscopic results

The mean pressure p below the tip is given by the applied normal load F and the radius of the contact area a:

$$\overline{p} = \frac{F}{a^2 \pi}$$

(Eq 20)

The effective force F is given by the applied load F_{app} reduced by the restoring force of the tip at a given indent depth d_{ind}:

$$F = F_{app} - k_{tip} d_{ind}$$

(Eq 21)

To calculate the restoring force in (Eq 21), the spring constant k_{tip} of the cantilever is needed. The restoring spring force was of the order of 5 nN ($k_{tip} \approx 1$ N/m) and therefore influenced the effective force only in the order of 10% for indents written at low force using the highest heater temperatures. We estimated the correction by replacing the unknown depth d_{ind} during writing by the measured depth of the final indents d_{rem}. The mean pressure beneath the tip will be related linearly to the yield stress. The scaling factor will range from 2 ($p = 2Y$ for strong elastic recovery) to 3 ($p = 3$ Y for full plastic indentation) depending on the exact contribution of the elastic recovery. We analyzed the data again using two models. In the first model we considered elastic contribution. This model was already used by IBM for the analysis of other storage media. In the second model, we use a model which is only based on plastic deformation, following the approach of Johnson [123]

a) Model with elastic contribution:

As we assume some elastic contribution we will use a relation of $p = 2.5Y$ for the further analysis of the data using the model with elastic contribution. Assuming viscoelastic indentation, we can use the principal of self-similarity (Eq 18) [26] again. Combining (Eq 16), (Eq 18), (Eq 20) and (Eq 21) into $p = 2.5$ Y yields in:

$$\frac{F_{app} - k_{tip} d_{rem}}{\pi \left(c_0 + c d_{rem} \right)^2} = 2.5 Y_{RT} \left(\frac{T_S - T_{Pol}}{T_S - T_{RT}} \right)$$

(Eq 22)

(Eq 22) can be solved for d_{rem} and has been used to obtain the global fits for all the data corresponding to each sample (Figure 36 e and f). There are only two free parameters, the yield stress at room temperature Y_{RT} and the softening temperature T_S of the polymer. For PS, the dashed lines in

each panel of figure 5 correspond to the result of this global fit using (Eq 22). We find good agreement of the fit lines to the experimental data. One would expect that the fit would go through zero, however, this is not the case, because there is a force threshold that is needed to cause a measurable indent, which is larger than zero.

This model fit for the PS data yields a softening point at a heater temperature of T = 417˚C, corresponding to an approximated polymer temperature of 221˚C. The yield stress at room temperature is Y_{RT} = 184 MPa. The extrapolation from different depth isolines makes the determination of the temperature independent of systematic errors in the force calibration.

By reinserting the mean pressure p (using (Eq 20) and (Eq 21)), and solving (Eq 22) for the polymer temperature T_{Pol} we get the following equation for the dependence of polymer temperature T_{pol} and mean pressure p

$$T_{Pol} = T_S - \frac{\overline{p} \left(T_S - T_{RT} \right)}{2.5 Y_{RT}} \qquad \text{(Eq 23)}$$

(Eq 23) predicts that all data gained from the indentation experiments at different heater temperatures and forces (exemplarily for PS, the contour lines in Figure 36 f) can be projected onto one linear master curve by the transformation of the indentation force into a mean contact pressure using (Eq 20). This prediction is confirmed by the measured data as shown in Figure 37 for all samples investigated. The intersection of the master curve with the x-axis yields the yield stress at room temperature, Y'_{RT}. The intersection with the y- axis yields the softening temperature, T_s of the sample material. Note that Y'_{RT} is not influenced by the calibration factor used for converting the heater temperature into the polymer temperature. The uncertainty of the calibration factor only adds a proportional systematic error to the temperature axis.
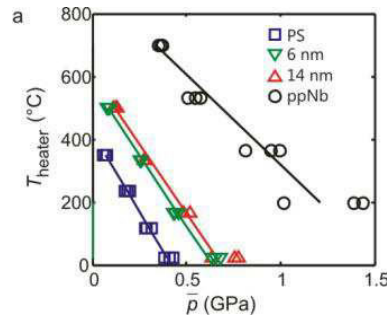

Figure 37: Linear master curves obtained by calculating the mean pressure under the tip for all indentation experiments on all samples and plotting this mean pressure against the heater temperature.

The yield stress Y'_{RT} at room temperature and the softening temperature T_s obtained from the master curve fit to the measured data. As expected, bulk ppNb is a significantly harder and thermally more robust material than PS. The Y'_{RT} value for ppNb is four times higher than for PS, 690 MPa vs. 184 MPa, respectively, and the softening temperature of 457°C is two times higher than the softening temperature of PS of 221°C. For the layered materials with a 6 and 14 nm thick ppNb protective coating we obtain effective softening temperatures of 299 and 314°C, respectively, and yield stress values at room temperature of 280 and 300 MPa, respectively.

b) Full plastic model

Assuming full plastic indentation, we use a slightly different model. The model differs mainly in the calculation of the contact radius between tip and sample during indentation. Here we use again (Eq 19) to calculate the contact radius from the tip radius R = 10 nm (from fit in Figure 36 g). Thus, the mean pressure can be calculated using (Eq 16) and (Eq 20), with $F = F_{app} - k_{tip}d_{ind}$ and replacing the unknown d_{ind} with the measured d_{rem}. Furthermore the mean pressure p scales with the yield stress in a fully plastic regime by $p = 3Y$. $\bar{p} = 3\,Y.$ Combining the equations leads to

$$\frac{F_{app} - k_{tip}d_{rem}}{4\pi(10nm \bullet d_{rem})} = 3Y'_{RT}\left(\frac{T_S - T_{Pol}}{T_S - T_{RT}}\right) \tag{Eq 24}$$

Again, we assume that $k_{tip}*d_{rem}$ is small compared to F_{app} and can therefore be neglected. We can now use (Eq 24) to fit the data from the indentation experiment. We show the fit exemplarily for the data obtained on the unprotected PS sample (Figure 38).
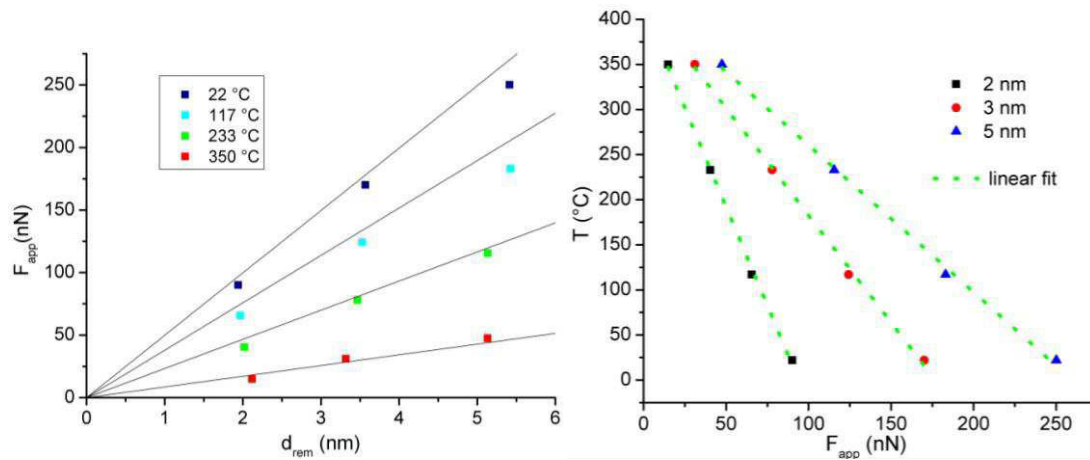

Figure 38: Fitting of the experimental data with a full elastic model (Eq 24). The quality of the fit is comparable to the model with elastic contribution.

Comparing the full plastic fit (Figure 38) and the fit with elastic contribution (Figure 36 e and f) shows that both models fit the data equally well. From the full plastic fits we obtain a Yield stress Y_{RT} of 131 MPa and a heater temperature of 418 °C, corresponding to a softening temperature T_S of 221 °C. While the softening temperature is almost identical with the one gained from the elastic model (T_{heater} = 417 °C, T_S = 221°), the plastic model results in a much lower Y (elastic model: 184 MPa, plastic model: 131 MPa). This difference results mainly from the different assumptions regarding the relationship between p and Y. For the elastic model we assumed $p = 2.5\ Y$, for the plastic one $p = 3\ Y$. Of course, this model can be used to obtain master curves for calculating the mean pressure p for each indent and plotting it against the heater temperature, too. The mean pressure p in the full plastic model is calculated using the normal load F_{app}, the tip radius R and the remnant indent depth d_{rem}

$$\overline{p} = \frac{F_{app}}{4\pi R d_{rem}}$$

(Eq 25)

The resulting master curve should be linear according to:

$$T_{Pol} = T_S - \frac{\overline{p} \bullet \left(T_S - T_{RT} \right)}{3 Y_{RT}}$$

(Eq 26)

These results show that the exact nature of the model or mechanism does not influence the resulting data beyond the systematic errors caused from force calibration and temperature dependence. Any model that describes the relationship between inner indent radius a and remnant indentation depth d_{rem} correctly can be used, because our analysis relies solely on the mean pressure beneath the tip.

An intriguing characteristic of the master curves (Figure 37) is the fact that the slopes for the layered samples are indistinguishable from the slope of the master curve for the unprotected polystyrene sample. On the other hand the slopes of the layered samples are very different from the slope of the master curve of the ppNb bulk sample. We take this as an indication that the plastic deformation in the layered samples is governed by yielding only in the polystyrene sublayer.

The top layer acts as an elastic skin, which screens part of the temperature and part of the pressure from the lower lying polystyrene layer (Figure 39). This assumption is supported by the fact that the bulk ppNb film has a much higher yield stress and softening temperature, which makes it unlikely that the thin layer of ppNb material would yield at the pressures and temperatures levels used in embossing the indents into the layered samples (Figure 39).
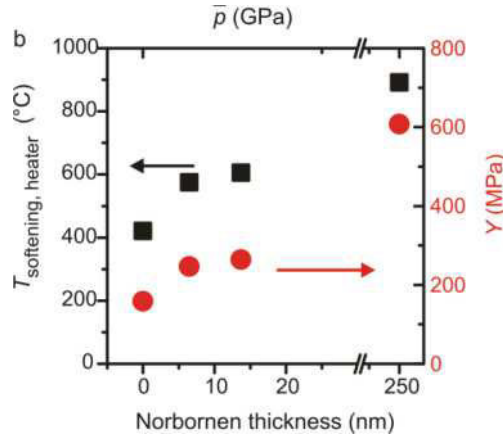
Figure 39: Comparison of the softening temperature T_S and the yield stress Y for unprotected PS, PS protected with 6.5 nm ppNb, PS protected with 13.7 nm ppNb and bulky ppNb. ppNb acts as isolating layer as well for the temperature as for the force acting on the PS layer.

Comparing softening temperatures and yield stresses of unprotected PS, layered stacks and bulky ppNb (Figure 39), shows a slight increase of both softening temperature and yield stress for the layered stacks. However, both stacks, PS with 6.5 nm ppNb and PS with 13.7 nm ppNb behave more like the pure PS than like the bulky ppNb.

The measured increase of the Y_{RT} yield stress is a consequence of a reduction of the force acting on the PS layer due to the stiffness of the protective layer, which acts as an additional restoring force against the applied electrostatic force actuating the cantilever. The observed increase of the softening temperature of the layered samples at zero applied force can be attributed to the thermal loss in the ppNb layer, which will be discussed in the following section.

Temperature profiles in the protection layer

The measured softening temperature T_s of the layered films is higher than the softening temperature T_s determined for the unprotected polystyrene sample. The increase in measured T_s is 78 K higher for the 6.5 nm ppNb protection layer and 93 K for the 13.7 nm ppNb protection layer. We assume that the plastic deformation during the indentation happens in the PS sublayer. Thus the ppNb protection layer acts as an additional thermal isolation layer. The temperature distribution is determined by the heater as the heat source at elevated temperature (T_{heater}) and the silicon substrate acting as the heat sink at room temperature (Figure 40 a). Only a part of the generated heat is transferred through the tip into the sample. The thermal resistance of the nanoscale tip is comparable to the thermal

resistance of the polymer film, so we assume that the temperature at the tip-polymer interface T_{tip} is approximately half of the heater temperature with respect to room temperature.
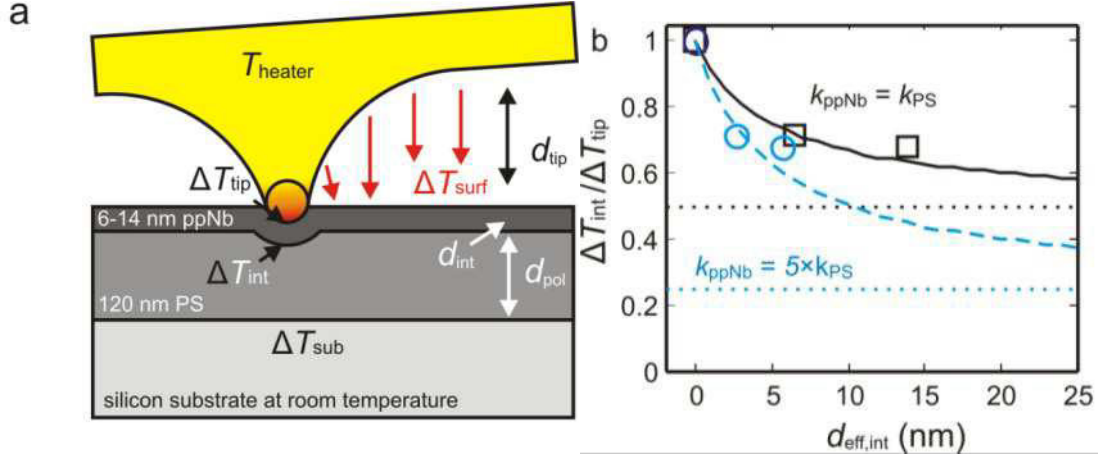

Figure 40: a) Illustration of the thermal model used. A tip is heated by a heater at temperature T_heater. The heat sink is a silicon substrate which is considered to be at room temperature at its backside. The heat path along the tip leads to a temperature increase of the tip-polymer interface *ΔT_tip*, and a temperature increase of the PS-ppNb interface *ΔT_int*. An additional heat path exists from the heater through the air to the ppNb surface, which leads to a temperature rise *ΔT_surf* underneath the heater area. b) Measured relative values of the temperature drop at the interface *ΔT_int/ΔT_tip* vs. the interface thickness. Solid lines are calculated temperature profiles in the polymer assuming a *ΔT_surf* of 50% and 25% of the *ΔT_tip*.

Heating via the air gap

Another part of the heat is transferred via the atmosphere from the heated cantilever to the sample surface (indicated by red arrows in Figure 40 a). We can calculate the increase of the surface temperature due to this unwanted heating. The thermal conductivity of air (0.03 W m^{-1}K^{-1}) is approximately 5 times lower than the conductivity of PS (0.17 W m^{-1}K^{-1}). The heated cantilever can be treated like a parallel plate heater positioned 500 nm above the 120 nm thick PS sample, which is placed on a silicon wafer. The Si wafer can be treated as a perfect heat sink because its thermal conductivity (139 W m^{-1}K^{-1}) is much higher than that of all other materials in the system. The temperature increase is calculated using $d_{pol}/d_{tip}*k_{air}/k_{PS}$, which amounts to 5 percent of the heater temperature. For heater temperatures of 450 - 600°C this means, that the surface is heated by 20 - 30 K via this heat transfer pathway. In addition to the polymer heating, the silicon substrate may be heated locally (ΔT_{sub}). Haeberle et al. have obtained a heating of a bare silicon substrate underneath a 440°C hot heater to be 20 K [36]. Therefore we estimate an upper limit for the polymer surface heating of 50 K through air.

Heating via the tip

To determine the temperature increase caused by the hot tip in contact with the polymer surface we assume a homogeneous thermal sample. This means, that the thermal conductivity of PS (k_{PS}) and the protective ppNb (k_{ppNb}) are the same. In this case the temperature scales approximately with r^{-1} into the film [29]. Taking into account a 5 nm tip radius r_{tip}, and the thicknesses d_{int} of 6.5 nm for the thinner and 13.7 nm for the thicker protection layer, we can calculate the expected increase in temperature ΔT_{int} at the interface between ppNb and PS using

$$\Delta T_{int} = \left(\frac{r_{tip}}{r_{tip} + d_{prot}} \right) \bullet \Delta T_{Pol} \qquad \text{(Eq 27)}$$

Here, ΔT_{pol} is the temperature rise of the polymer at the surface with respect to the polymer temperature ΔT_{surf} far from the tip contact ($\Delta T_{pol} = \Delta T_{tip} - \Delta T_{surf}$). The temperature of the polymer far from the tip might still be increased by up to 50 K due to the heat transfer from the heater to the surface via air.

Before, we found that the plastic deformation occurs in the material at the PS-ppNb interface. Therefore we can set the temperature of the interface ΔT_{int} to 221˚C, as the measurements on unprotected PS revealed this to be the softening temperature at the timescales of our experiment. However, for the protected PS we measured an increase in softening temperature to 299˚C and 314˚C, respectively (Figure 39). The measured increase indicate that only 72% and 68% of the temperature increase reach the ppNb-PS interface using room temperature (25˚C) as reference. This ratio ($\Delta T_{int}/\Delta T_{tip}$) is plotted vs. the protection layer thickness (Figure 40 b, black squares). A good fit for (Eq 27) requires a polymer background temperature ΔT_{surf} of approximately 0.5 times the tip-polymer temperature ΔT_{tip} (black dotted line in Figure 40 b), which amounts to 100-150 K. This increase is much higher than the estimated limit in surface temperature rise of 50 K calculated above, so the assumption of the same heat conductivity for PS and ppNb is wrong. As both materials should exhibit strong differences in the crosslinking density, differences in heat conductivity can be expected.

To take the different heat conductivities of the polymer layers λ_{PS} and λ_{ppNb} into account, we have to make some assumptions concerning the heat conductivity of ppNb. A higher heat conductivity of the ppNb layer leads to a proportionally reduced effective thickness for the heat transport, which would better fit (Eq 27). The heat conductivity of PS, $\lambda_{PS} = 0.17$ W·m^{-1}·K^{-1} is low compared to other polymers in the amorphous glassy state, hence λ_{ppNb} could be significantly higher (for example, polyethylene

has a heat conductivity λ_{PE} ranging from 0.33 to 0.57 W·m^{-1}·K^{-1} [124]). In addition, it is generally accepted that the heat conductivity in a polymer is 10 times higher along the backbone of the chains than between different chains. Therefore the highly cross-linked ppNb film should have a higher thermal conductivity value and indeed higher thermal conductivity of cross-linked polymers has been observed. Furthermore, the high compressive stress in the tip-sample contact region may enhance the heat conductivity further. Thus, a significantly higher heat conductivity for ppNb compared PS is reasonable. Assuming a 2.5 times higher heat conductivity of the ppNb film, we can replace the protection layer's thickness with a 2.5 times reduced thickness (Figure 40 b, blue circles). In this case the dotted blue line corresponds to a ΔT_{surf} of 0.25 times ΔT_{tip} corresponding to a surface temperature rise of 50 K, which would be in the limit of the estimated rise in surface temperature.

A similar argument can be put forward to explain the increase in yield strength of the samples with a protective ppNb layer. The highest stress in an indentation process occurs at a distance of ~ 0.8 a in the depth of the sample. For larger depths, the stress decreases approximately with 1/r. Therefore, we expect that the stress at the PS-ppNb interface would be approximated to be 1.4 and 3 times reduced in comparison to the blank PS film. In the experiment we observed an increase in yield stress by a factor of 1.5 and 1.7. The agreement is reasonable, especially when taking the higher elastic modulus of the ppNb film into account.

6.5 Influence of short time scale

In macroscopic experiments, amorphous PS with high molecular weight shows a well-defined glass transition at 100 °C followed by a small rubber plateau [89]. Since in amorphous polymers no crystalline domains are present, there is no defined melting point. However, for high molecular weight amorphous PS the rubber plateau ends at temperatures above 150 °C, where additional softening is observed [89]. These glass transition and softening temperatures were determined with macroscopic stress relaxation experiments which had a duration of 10 s.

With the nano-indentation experiments, we observed a softening temperature of high molecular weight amorphous PS of 221 °C. The softening temperature determined with nano-indentation is much higher than the glass transition and softening temperature determined with macroscopic stress relaxation experiments. The shift to higher temperatures observed here is due to a change in timescale: The macroscopic stress relaxation experiment probes the properties of PS at a 10 s time scale. Our nano-indentation experiments probe the properties of PS at a 10 µs time scale.

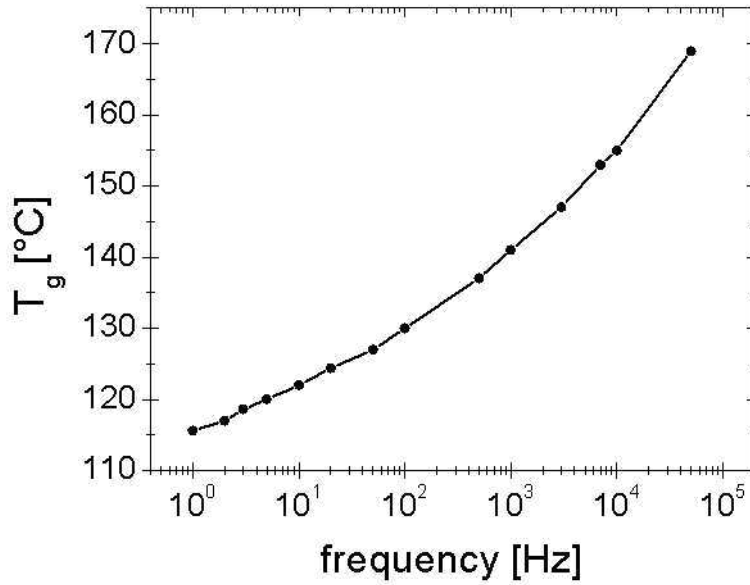For glass transition, a strong time dependence has been observed [125-127] (Figure 41).

Figure 41: Dependence of the glass transition temperature T_G of polystyrene on the attempt frequency

In the nano-indentation experiments, the attempt frequency was 1/10 µs = 100 kHz, therefore a shift to temperatures higher than 170 °C is expected (Figure 41), which is in accordance to our result of a softening temperature of 210 °C. With the experimental setup of high frequency nano-indentation used here, it is not possible to distinguish between glass transition and softening temperatures, as we are just sensitive towards changes of the polymer's yield strength which should occur both in the glass transition range and in the softening temperature range.

To achieve higher data transfer rates, higher attempt frequencies need to be used, which will further increase the needed temperature. Therefore, other polymers with even lower T_G could be used as a sublayer in the future, in order to keep the temperatures for writing as low as possible.

6.6   Application as data storage medium

The ppNb-PS samples which were nano-wear stable, i.e. 100 nm spincoated PS protected by ppNb deposited in continuous mode at 150 W were subsequently tested for their nano-indentation properties in terms of thermomechanical data storage applications. Therefore, the samples were prepared on highly doped, thus highly conductive silicon substrates. Two samples were investigated, which mainly differed in the thickness of the protection layer. The first sample consisted of 114 nm PS

protected with 6.5 nm ppNb, the second sample of 111 nm PS protected by 13.7 nm ppNb. The thermomechanical reading and writing tests were performed on the sample with the 6.5 nm ppNb protective layer which needs the lowest indentation force. Thermomechanical data writing was performed at a tip-heater temperature of 350°C, a normal force 80 nN and force and heater pulse durations of 10 μs (Figure 42). The mean indentation depth was between 2 nm and 4 nm. The indents were clearly imaged during reading. A logical one state was encoded by an indentation, a zero as no indentation.
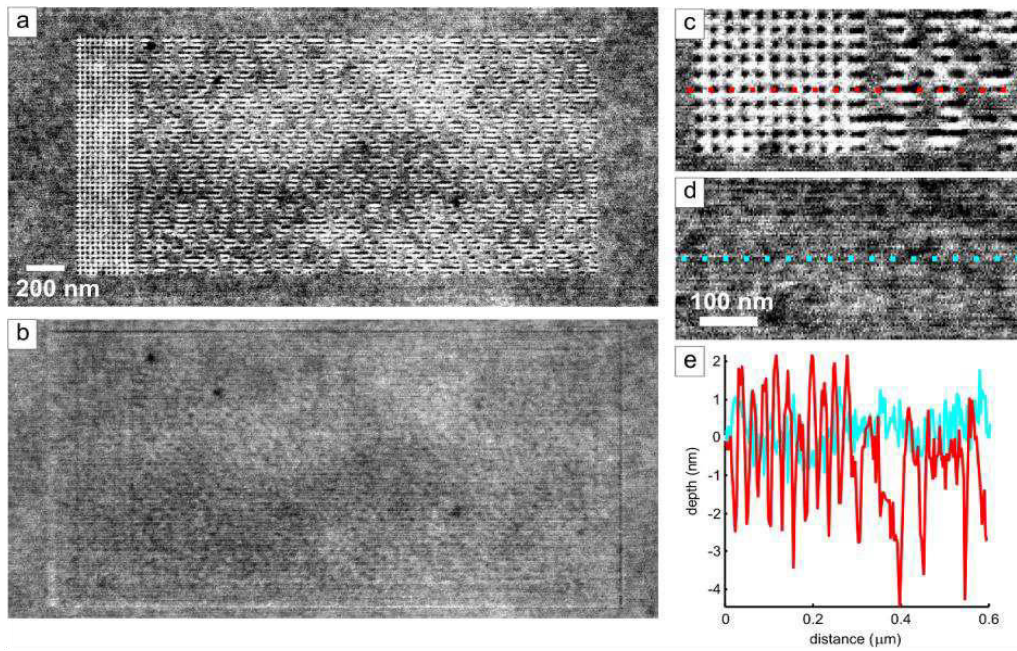

Figure 42: Thermomechanical writing and erasing of bit patterns. a) And c) bit field written in the layered media with the thinnest ppNb layer of 6.5 nm. The heater temperature and force for writing were 350˚C and 80 nN, respectively. A pulse duration of 10 μs for the force pulse and the heat pulse were used. b) And d) show the same areas as respectively displayed in panel a) and c) after performing an erase operation. The groove pattern is cleanly removed. e) Topography profiles along the line of grooves as depicted by the red dotted line in panel c). The depth of the grooves is between 2 and 4 nm (red line), whereas the erased surface (blue line) has a roughness of~ 2 nm peak to peak, similar to the roughness of a virgin surface.

The data field consisted of 48 lines of bits (tracks) with 200 bit positions in each line. The bits along each track were separated by 13.4 nm spacing, which was half the inter-track distance of 26.8 nm. The preamble consisting of 10 ones separated by 9 zeros at the left of each track was written clearly and the individual indents were well separated (Figure 42c). In the random bit field we observed that the indents of adjacent ones merged to form extended grooves, which enabled a closer packing of information in the same area. The physical areal density was $(25.4mm)^2/(26.8nm \times 13.4nm) = 1.8$

Tbit/in^2. For comparison, the perpendicular magnetic recording (PMR) technology introduced in 2006 for magnetic hard drives has a technical limit in data density of about 1 Tbit/in² due to the superparamagnetical limit. Usual hard drives used today reach data densities of 600 Gbit/in².

For the data storage application, the possibility to erase and overwrite the information is an important asset. We found that closely spaced indents interact in a non-linear fashion because of tensile stress components in an annular ring around a written indent which provides a restoring force [26, 27]. Thus, by writing a close series of bits, written data can be permanently erased. For the presented bilayered medium, the bit field was erased by writing two 10 percent larger bit fields consisting of only ones using an indent and track pitch of 13.4 nm (Figure 42 b). For erasing, the same operating conditions were used as for writing. The erased area was still visible by the dark lines on top and on the left of the erase area and the white border at the left and the bottom border. Those positions marked the writing of the last and the first indentations of the erase field. Within the erase field the indents encoding the data were well erased (Figure 42 b + d). The RMS roughness after erasing was 0.55 nm/µm², similar to the RMS roughness of 0.50 nm/µm² of the virgin surface (Figure 42 c and d). There was no indication that the protection layer was damaged during the writing, reading or erasing, nor was there any detectable nano-wear. Although the conditions for writing and erasing the bit field, 350˚C tip-heater temperature and 80 nN applied normal force, seem to be very high considering that PS usually has a T_G of 100 °C, one has to compare these conditions to the conditions used for other media. For example, too achieve a similar quality of writing in other proposed polymeric storage media, e.g. highly cross-linked polyaryletherketones (PAEKs), much higher temperatures of up to 500˚C at normal force values below 100 nN had to be applied [106, 128]. Thus the ppNb protected PS film exhibited excellent performance for data storage application.

6.7   Main findings

- Norbornene can be plasma deposited on silicon substrates and PS. The deposition parameters for nano-wear resistive ppNb layers depend strongly on the substrate. On different substrates, different mechanisms lead to the nano-wear. Strong crosslinking in the ppNb layer and binding between PS and ppNb are necessary to avoid any surface wear. ppNb layers as thin as 6.5 nm are still effective nano-wear protection layers.

- ppNb layer shields forces and temperature, thus the temperature and force needed for indentation of the PS sublayer scales with the ppNb layer thickness.

- The temperatures determined for softening of PS during the nano-indentation experiments are shifted to higher values compared to macroscopic experiments. This shift is due to the higher attempt frequencies used in nano-indentation (time-temperature superposition).

- Data recording experiments demonstrated that "soft" indentation properties, i.e. low tip temperatures and low applied pressures, compared to single layered, but crosslinked polymeric media can be achieved for the PS-ppNb stacks. In addition, the successful erasing mechanism indicates that the fundamental indentation mechanics is in essence the same as for an uncoated but cross-linked polymer film. This suggests that created indents are frozen in a metastable state stabilized by the elastic coating and that the yielding occurs in the soft PS layer.

- More generally, the bilayers feature a separation of the plastic deformation and the direct tip-sample contact. The indent is formed away from the tip-sample interface in the underlying polymer. Such a physical separation protects the tip from contamination and the sample from deformation induced by the scanning tip. Furthermore the protective coating should remove any surface induced lowering of the glass-transition temperature, which further stabilizes the system. In addition, a layered system can be independently optimized for the properties of the protective coating and the desired mechanical properties of the sublayer material. The latter can be tuned to find the optimal trade-off between softness and retention capabilities. As a general scheme, the protective coating allows the use of uncross-linked storage media, which dramatically enriches the choice of materials and the ease of implementation.

7.   Investigation of Redox-active polymers

Electrical switchable polymers are of interest for electronic applications due to several advantages: They can be processed from solution and their molecular properties can be tailored for different applications, for example the integration of stored information about the genuineness in expensive textiles. For data storage they would allow cheap and fast device fabrication, low power consumption and high data storage densities [129]. An electrical switchable polymer can be switched between two oxidation states with distinct different conductivity by applying a bias. The basic experiment for SPM based testing of the switching properties of electrical switchable polymers is to pattern a certain area of the polymer by applying a bias between conductive tip and conductive substrate (Figure 43 a). First, a writing bias V_W is used to change the oxidation state into the higher conductive state. Second an opposite erasing bias V_E between tip and sample on a smaller area in the center of the first pattern is applied, thus the oxidation state changes back to the less conductive state (Figure 43 b). Third, the surface is scanned with the reading bias V_R, which is lower than V_W and V_E in order to avoid additional writing or erasing (Figure 43 c). The local conductivity, measured by recording the current flow, should then show a high conducting square with a less conductive square in the center (Figure 43 d).
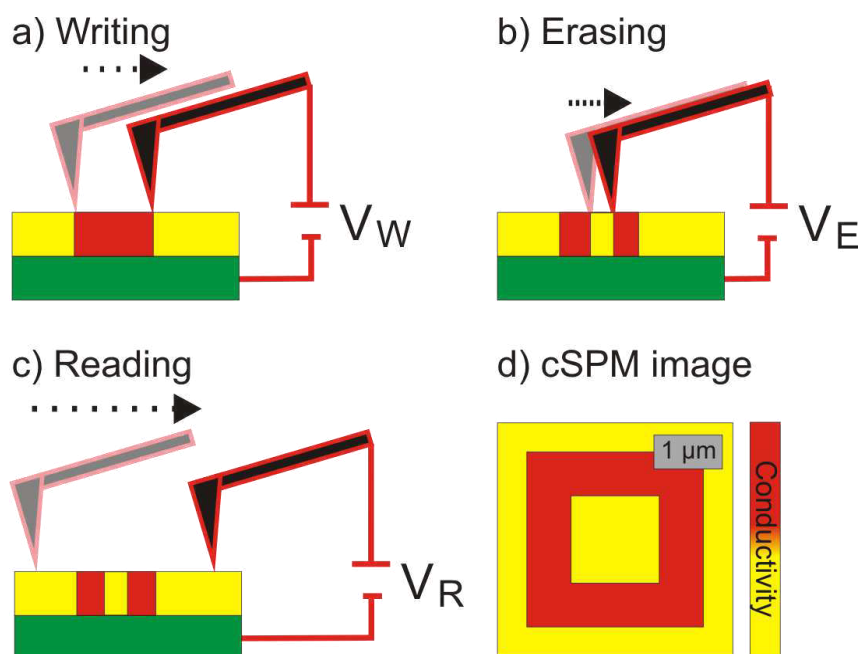

Figure 43: Basic idea of SPM based patterning of an electrical switchable polymer: a) By applying a writing voltage V_w the polymer is locally oxidized. b) By applying an opposed erasing voltage V_E, part of the oxidized polymer is locally reduced again c) By using c-SPM with an applied reading bias V_R the pattern is analyzed. d) Resulting c-SPM image showing the different conductivities of oxidized and reduced areas of the polymer.

As changes in conductivity are often caused by changes of the film thickness, the topography of the sample is recorded in the same experiment. An ideal redox-active polymer for data storage application should not show any change in topography in the patterned areas.

My work on electrical switchable polymers was conducted in collaboration with Ali Golriz (MPIP Mainz), Jochen Gutmann (University Duisburg-Essen) and the group of Prof. Ono (Tohuku University, Sendai, Japan). In our work, we wanted to use phenothiazine moieties. Phenothiazines are reported to be able to undergo an one electron redox reaction, resulting in a stable phenothiazine radical cation (Figure 44) [130]. The stability of this cation is of special interest for an electrical data storage application. The stored data, i.e. the redox state of the polymer, should not change with time, temperature, humidity or other environmental influences. The successful use of phenothiazine based material for memory applications was presented by Morishima et al., who demonstrated the successful reversible oxidation of poly(3-vinyl-10-methylphenothiazine) on platinum electrodes [131]. In their case, the oxidized polymer exhibited an increase in conductivity of about 5 to 6 orders of magnitude, although only a partial oxidation of 3 − 4 mol-% of the phenothiazine moieties had taken place [132]. In order to form thin, wear stable layers, the phenothiazine was used in the form of a phenothiazine containing polymer. For this polymer (Figure 44), 10-(4-vinylbenzyl)-10H-phenothiazine (VBPT) monomers were synthesized by A. Golriz. The VBPT monomer was polymerized using atom transfer radical polymerization (ATRP) leading to polymers with a molecular weight ranging from 5000 to 15000 g/mol by A. Golriz [18]. The SPM measurements were conducted on a polymer with a MW of 13400 g/mol and a molecular weight distribution of MW/Mn of 1.43.

Cyclovoltametric measurements showed that oxidation of PVBPT takes place in two steps, the first leading to a radical cation, the second resulting in stable dication [18]. Both oxidation steps are fully reversible.
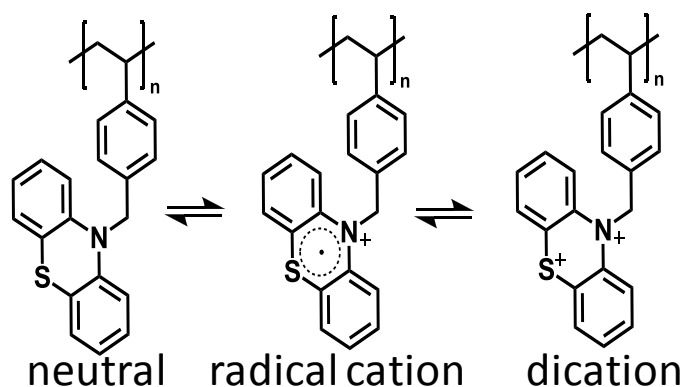

Figure 44: Structure of poly-10-(4-vinylbenzyl)-10H-phenothiazine (PVBPT) and its radical states

7.1 Surface stability

In order to test the mechanical stability of the polymer surfaces, which is here again an important criterion to judge the suitability of the material for data storage applications, I conducted SPM based nano wear tests. The tests followed the already described scheme: A 5 x 5 µm² area was imaged. Then a 3 x 3 µm area in the center was scanned for 100 times at a defined load and tip speed. Upon scanning with an applied load of 5 nN, no changes in topography occurred (Figure 45 a). The surface was intact and all surface features that were visible before the test were still visible afterwards. Comparing the root mean square roughness in the 3 µm x 3 µm wear test area before (RMS = 0.49 ±0.01 nm) and afterwards (RMS = 0.50 ± 0.01 nm) revealed no change of surface smoothness. Upon increasing the applied load to 10 nN (Figure 45 b), globular aggregates formed.
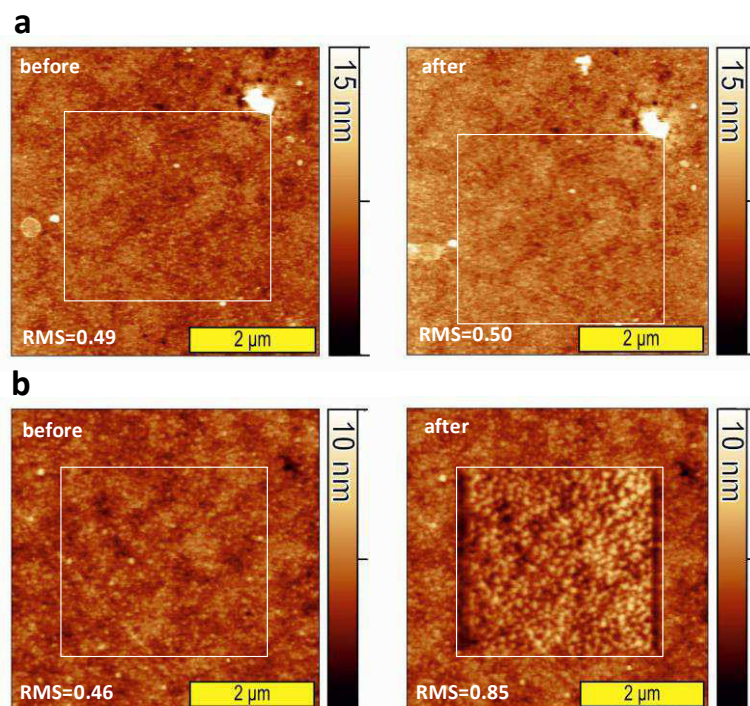
Figure 45: Wear test performed on PVBPT film. The rectangular area of 3 µm x 3 µm was raster scanned 100 times with a tip speed of 50 µm/s in contact mode. a) Using an applied load of 5 nN during the wear test resulted in an undamaged surface. b) Upon increasing the applied load to 10 nN, surface wear occurred. The PVBPT formed globular agglomerates. Shifts in position result from sample drift during the wear test experiment.

The observed wear patterns were not regular wavelike structures as they were observed for wear experiments on polystyrene or polynorbornene. The average height of the patterned areas was not

increased compared to the non-worn surrounding. This indicates that no delamination or crack propagation in the film took place. Material was moved by the tip over the surface and formed agglomerates which is in accordance with the described stick-slip or molecular broom effect [20]. Removal of material occurred in the ditches at the left and the right of the test area. Here, the cantilever turns its moving direction and moves to the next scan line which increased the wear in these zones. At 10 nN load, the wear is related to a doubling of the RMS roughness from 0.46 nm to 0.85 nm in the test area. Compared to other materials like polynorbornene (MW = 1.000.000 g/mol) or PS (MW = 100.000 g/mol), which both showed stronger wear, the PVBPT showed an acceptable mechanical stability.

As we found that it can be scanned for at least 100 times at a force of 5 nN without mechanically changing the surface, electrical patterning experiments can be conducted. All changes observed during these experiments should then be related to electrical effects, as long as the applied load on the cantilever is at 5 nN or smaller.

7.2 Writing and reading structures with different conductivity

Determining the writing voltage

In a first experiment, I tried to find out which writing voltage V_W is needed to reliably switch the oxidation states of the PVBPT on the surface. To show all the results in one image, I summarized several pre-experiments in a single experiment (Figure 46). V_W was increased in steps of +2 V from 0 V to +10 V, the maximum voltage which can be applied using the built-in power source of the Multimode TUNA TR instrument. During this patterning the current flow was recorded (Figure 46).

The areas patterned by applying a voltage and the spacers where the voltage was switched off can be clearly distinguished for V_W of +6 V and higher. For writing voltages of +4 V and +2 V a few brighter spots indicated, that very few current pathways occurred which were quite small (30 to 50 nm in diameter). For V_W = +2 V three conductive spots were found, while for V_W = +4 V already eleven spots appeared. Increasing the writing voltage to +6 V led to a clear increase in conductivity, despite the fact that still single conductive spots could be seen. For V_W = +6 V more than 50 spots were counted. Furthermore, the spots increased in their individual size. For higher voltages more and bigger conductive spots appeared. The mean profile along the slow scan axis (Figure 46 b) shows that for +2 V and +4 V writing voltages the mean current flowing during the writing was too small to be detected.

For +6V the average current flowing was 100 ± 50 fA. For +8 V the current increased to 420 ± 130 fA and finally for +10 V the mean current was 700 ± 380 fA with peak currents up to 1000 fA.
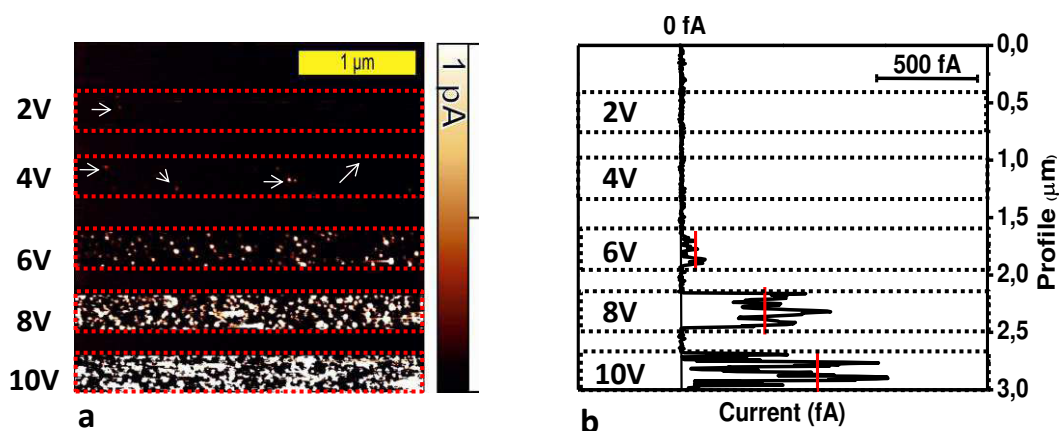

Figure 46: Patterning of PVBPT on gold using different writing voltages V_W ranging from 0 V to 10 V. Each voltage was applied for an area of 300 nm width. The different areas are separated by 300 nm stripes where no voltage was applied. The current amplifiers offset of +10 pA was corrected to 0 A. The sample was a ~45 nm thin PVBPT film on gold. The force acting on the cantilever was kept below 5 nN to avoid mechanical damage of the surface.

Cyclic voltammetry measurements conducted on a 0.1 M solution of PVBPT in dry DCM with 0.1 M tetrabutylammonium tetrafluoroborate revealed that the oxidation of the neutral PVBPT to the radical cation took place between +0.6 and +0.7 V. The further oxidation to the dication happened between +0.8 and +1 V [18]. Compared to these voltages, the bias needed in the SPM experiment is much higher. The differences may be due to different switching behavior of the PVBPT in solution and as a solid. Structural re-arrangements may occur much easier in solution than in the solid film. Another explanation arises from the small contact area between the tip and the PVBPT film. For an applied force F_N of 10 nN and a tip radius R of 10 nm, the contact radius a calculated using Hertz model for PS was ~ 3 nm. Here, the contact radius should be even lower due to the smaller applied force and the surface roughness of the PVBPT. A contact radius a of 3 nm corresponds to a contact area of 28 nm². This small contact area could result in an increased contact resistance R according to:

$$R = \rho \bullet \frac{l}{A} \qquad \text{(Eq 28)}$$

Following (Eq 28), the small contact area needs to be compensated by a very low film thickness l in order to keep the contact resistance R as low as possible.

In the solution the tetrabutylammonium tetrafluoroborate salt leads to a good conductivity between the two electrodes. In the SPM experiment the non-oxidized film is an isolating layer between the gold substrate and the conductive tip. Comparably high voltages needed for patterning were also observed for other systems like 2,2,6,6-tetramethylpiperidine-1-oxyl (TEMPO) based polymers, for which the writing and reading voltages were in the same magnitude for SPM based patterning and reading [61]. The huge difference between the voltages needed to change oxidation states in solution and in a thin film using a conductive tip is therefore not only an issue for the system investigated here, but for all other applications that deal with electrochemistry effects induced by c-SPM.

Determining the reading voltage

To check, which voltage is suitable for reading, i.e. imaging patterned areas, I performed several pre-experiments. First I patterned a 3 µm x 3 µm area using V_W = +10 V. As the oxidation of the PVBPT should lead to a permanent change in conductivity, the next experiment was to read the written squares. As voltages higher than +4 V led to a current flow on the neutral PVBPT (Figure 46) I used voltages below 4 V for the reading experiments, in order to avoid further oxidation. I scanned a 5 µm x 5 µm area starting with V_R = -6 V. When the 3 µm x 3 µm square with increased conductivity appeared I switched V_R off (V_R = 0) for approx. 300 nm. After this 300 nm I switched V_R to the first desired value for 300 nm. Again, V_R was switched to 0 V for 300 nm and so on (Figure 47).
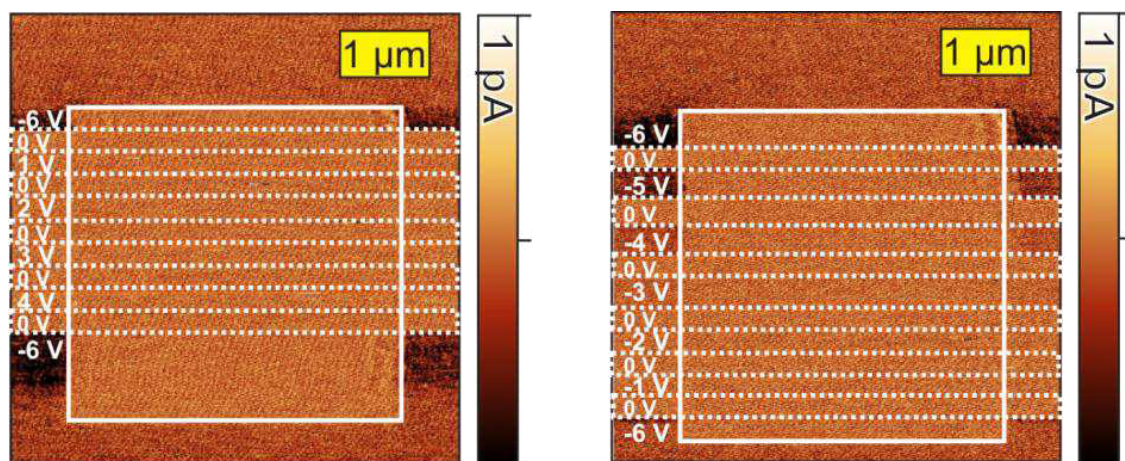
Figure 47: Different reading voltages V_R ranging from +4 V to -6 V. Prior to the reading a 3 µm x 3µm square was patterned using a V_W of + 10V. a) Positive reading bias, b) negative reading bias.

First (Figure 47 a), I demonstrated, that applying positive voltages from 0 V to 4 V did not lead to any detectable current flow. In the areas scanned with a V_R of -6 V, the patterned and the non-patterned part can be clearly distinguished. As expected, for 0 V there is no difference in the current image

between the patterned and the non-patterned part. Voltages above +4 V were not checked as they would lead to oxidation of the PVBPT, which would correspond to the writing process tested above.

Using a negative bias of V_R = -6 V and V_R = -5 V. (Figure 47 b) for imaging of the conductivity difference works well. The contrast between patterned and non-patterned areas scales with the reading voltage V_R (Figure 48). For V_R = +6 V, the current difference is 0.35 ± 0.1 pA. For V_R = -5 V, this difference is reduced to 0.2 ± 0.1 pA. For -4 V there is still a visible contrast of 0.1 ± 0.05 pA. Further reducing V_R to -3 V leads to a very weak contrast of 0.05 ± 0.05 pA between the patterned and non-patterned areas. Below -3V there is no measurable difference between the areas. The measured current for -2 V and -1 V is the same as when not applying any voltage at all, indicating that the flowing currents are too small to be detected by the instrument. From this results we concluded, that operating the c-SPM with a reading voltage of -6 V should lead to a stable imaging of structures written with a writing voltage of +4 V or higher.
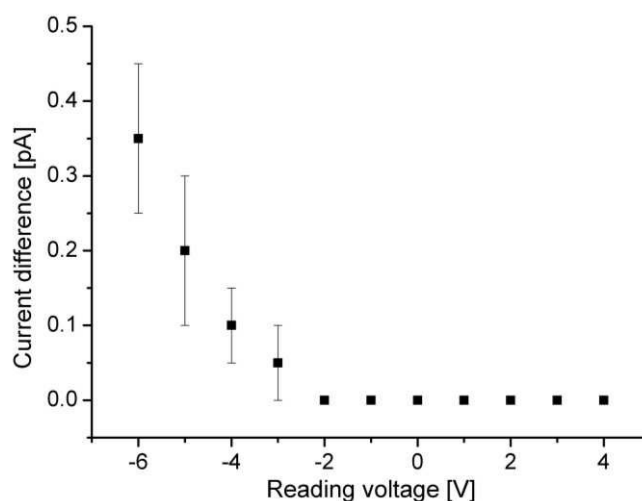
Figure 48: Scaling of the current difference (contrast) between patterned and non-patterned areas (V_W = + 10 V) with the reading voltage V_R. For voltages below 3 V no current difference is detected.

Imaging the patterned areas at -6 V worked reliably so this reading voltage was used for further experiments.

Influence of writing voltage

Imaging areas written at different writing voltages resulted in Figure 49 a and c. The stripes written with +10 V and plus +8 V can be clearly seen in the current image (Figure 49 a). For a writing voltage of +10 V, the topography was altered, too (Figure 49 c). As the mechanical load of the tip was too low

to cause mechanical damage this change in topography can be related to structural rearrangements of the PVBPT during the oxidation. In addition, joule heating in the thin film, which I expect to have a high resistance, can lead to topography changes due to expanding material. On the other hand, the expected electrostatic forces when applying a voltage of +10 V between tip and sample may lead to an unwanted increase in force, leading to some mechanical wear.
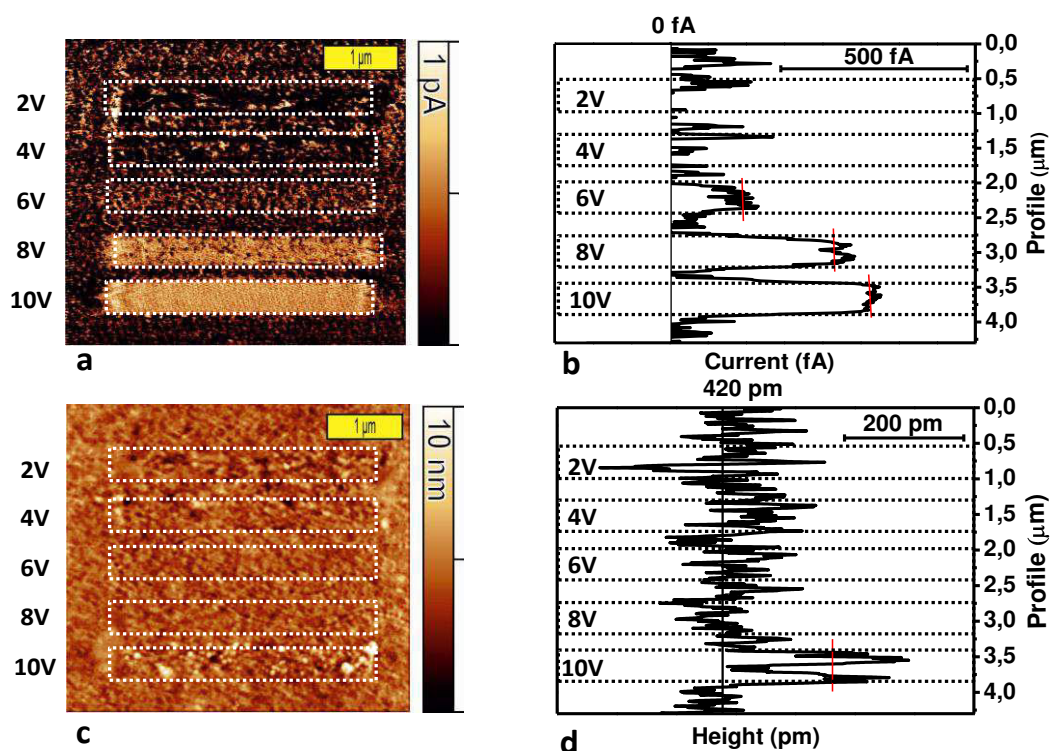
Figure 49: a) Current image recorded with V_R = -6 V. The stripes written with + 10 V, +8 V and +6 V are clearly visible. The stripes written with +4 V and +2 V are still visible, although the contrast between patterned and non-patterned areas is weak.

Comparing the cross-sections in slow scan axis through the conductivity and the topography images (Figure 49 b and d) reveals, that electrical patterning with V_W = +8 V leads to almost the same contrast in the conductivity between patterned and non-patterned areas as patterning with V_W = +10 V. However, the topography seems almost unchanged for the patterning with +8 V. Patterning with lower V_W of +6 V, +4 V or +2 V does not change the topography, but there is just weak contrast in conductivity. The best compromise between reaching a high contrast in conductivity without changing the topography is a patterning process at +8 V and a reading process with V_R = -6 V.

The area patterned with + 10 V is not only rougher than the non-patterned areas, also the average height is increased to about 170 ± 130 pm. Other groups reported increases in height of several

nanometers for thin polymer films [133, 134]. The height increase of thin films of poly(methylmethacrylate) (PMMA), poly[2-(N-carbazolyl)ethylmethacrylate-co-methacrylic acid] (PCEMMA)[135] or PTMA reached up to 38% of the original film thickness. For these films deposited on gold, the height increase has been explained by a water based ionic drift mechanism. Due to Joule heating of the sample, the segmental motion of the polymer chains is increased. Furthermore, dissociated ions from the water meniscus around the tip drift into the film forming conical shaped structures [134]. For the PVBPT investigated here, these processes are far less pronounced which can be explained by a better mechanical stability of the film, indicating a reduced mobility of the polymer chains.

For the PVBPT, writing bias potentials of above +4 V have to be applied in order to oxidize the moieties. There seems to be a threshold potential for this oxidation between +4 V and +6 V. Above +6 V enough moieties are oxidized to lead to a measurable conductivity contrast compared to non-oxidized PVBPT. Increasing the writing bias leads to a more homogeneous distribution of the current values in the patterned areas (Figure 49 b), indicating that more or larger conductive pathways are formed. This would be in agreement with the current flow measured during the writing (Figure 46). The same was found for poly(3-vinyl-10-methylphenothiazine) PVMPT, where the oxidations of only a few moieties leads to a measurable change in conductivity [131, 132].

Influence of tip velocity during writing

For data storage applications the transfer rate, i.e. the speed which with data can be written into the medium is of interest. For a simple test how fast the PVBPT responds to the applied bias, I patterned the PVBPT with constant voltage but different tip velocities. The stripes were written with tip velocities of 5 Hz decreasing down to 0.1 Hz (Figure 50 a). In the current image recorded during the writing no clear trend can be seen. All patterned areas showed a similar distribution of flowing current. Afterwards, I zoomed out and imaged a 5 μm x 5μm square with an applied V_R of -5 V (Figure 50 b). In contrast to the experiment with different writing voltages (Figure 46 a), the difference is not visible in the current image recorded during writing (Figure 50 a) but only in the current image recorded afterwards during reading (Figure 50 b). The current flow recorded during writing thus only depends on the applied voltage and not on the tip velocity. Upon exceeding a certain current threshold, which is given by the films resistance, a detectable current flowed between tip and substrate. The independence of recorded current flow during writing and tip velocity arises from the fact that the current flow during writing is not depending on formed current pathways in the film and thus not on the exact position of the tip.
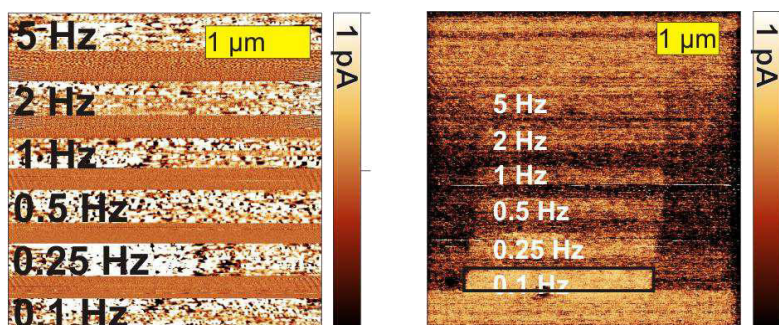
Figure 50: a) Current flow during writing stripes with V_W **= +10V. Each stripe is ~ 300 nm wide and separated from the next stripe by 200 nm during which the voltage was switched off. The upper stripe was patterned with a tip velocity of 5 Hz. The speed was then reduced to 2 Hz, 1 Hz, 0.5 Hz, 0.25 Hz and 1 Hz. b) resulting current image recorded with** V_R **= -5 V. The contrast between patterned and non-patterned areas increased with decreasing tip velocity.**

Time stability of written areas

For a good storage medium, the time stability of written data is of utmost importance. In the case of the PVBPT this means, that written patterns should not change over time. The stability of the radical polymer (PVBPT*)$^+$ BF$_4^-$ was examined via X-band ESR measurements [18]. From this measurements we concluded, that formed PVBPT radicals should be stable for at least several month under ambient conditions. In an additional experiment, I checked the long term stability of the PVBPT oxidized using c-SPM, in order to compare the stability of the written structures with the stability expected from ESR measurements. I wrote patterns with different voltages and imaged the patterns directly afterwards by scanning a larger area (Figure 51 a). After this measurement the tip was retracted from the surface and the sample was kept in the microscope overnight. After 16 h the tip was engaged and the surface was mapped again. The recorded image (Figure 51 a) showed, that all three stripes were still clearly visible. To compare the structures measured directly after writing and after 16 h, a current profile over the marked area patterned with +10 V was taken. These profiles (Figure 51 b) showed a current difference of 583 ± 62 fA at the first scan and 575 ± 84 fA after 16 h, respectively. The patterned areas remained stable for at least 16 h, so the results from this experiment concerning the stability of the conducting state of PVBPT agrees well with the data obtained from x-band ESR measurements for (PVBPT*)$^+$ BF$_4^-$ [18].
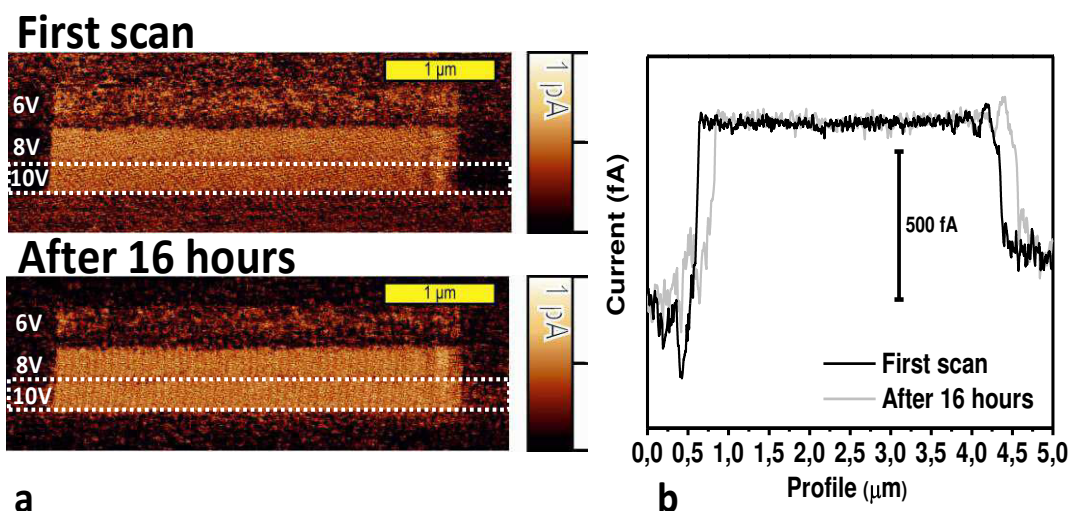
Figure 51: Patterns in PVBPT after writing with V_W = +6 V, +8 V and +10 V with tip velocity 0.3µm/s. Reading the patterns was done at V_R = -6 V. a) (top) directly after patterning, (down) after 16 h at ambient conditions. b) Profiles measured across the stripes written with +10 V.

7.3 Erasing of written data

A typical storage medium has the ability to be deleted in order to remove unwanted or unnecessary data. The SPM erase experiment is based on applying a erase bias V_E which is reverse to V_W on parts of an already patterned area (Figure 43 b).After successfully patterning an area (Figure 52, left side)., I tried to erase the central part by scanning it with an applied erasing bias V_E = -10 V. However, imaging the whole area again at a V_R of -6 V revealed, that the initial pattern was unchanged (Figure 52, right side). Repeating the process three times did not lead to any change in the measured current. Thus, erasing was not possible. Similar erasing attempts of written structures for poly(3-vinyl-10methylphenothiazine) (PMPT) were reported to be unsuccessful as well. The thin PMPT films were still highly conductive after reducing them [136, 137]. For other materials like poly(2,2,6,6-tetramethylpiperidin-1-oxyl methacrylate) (PTMA), the patterning was investigated using c-SPM on thin films on gold [61], too. Although the CV measurements of this material indicated a full reversibility of the oxidation step, the reversible oxidation, thus the erasing step, was not reported for this material, indicating that it was possibly not successful.
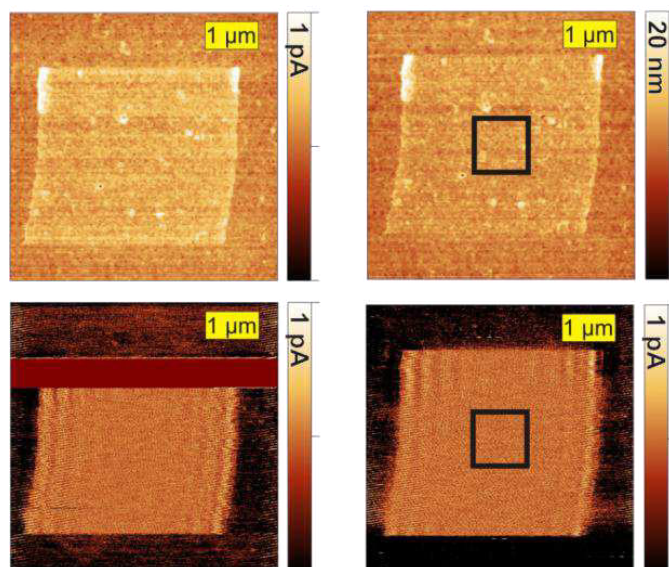
Figure 52: 4 μm x 4 μm patterns (V_W = +10 V= imaged (V_R = -6 V) before (left) and after erasing (right) a 1 μm x 1 μm square (indicated black squares) in the middle of the patterned area (erasing bias V_E = -10 V).

One explanation for this irreversible behavior is based on the molecular orientation of the redox active phenothiazine moieties. The oxidation of PVBPT leads to a planarization of the phenothiazine rings, which may lead to an intermolecular π – stacking [138]. The formation of the π-stacked rings is supported by XRR measurements of neutral PVBPT and precipitated stable salts formed form oxidized PVBPT and BF_4^- ($PVBPT^+ BF_4^-$). For neutral PVBPT we found two broad peaks at the diffraction angle 2 θ = 12.53° (7.06 Å) and 19.89° (4.46 Å), which were related to the formation of the side stacking (bridging of the benzene rings) [139]) and π-stacking of the bent phenothiazine rings [140], respectively (Figure 53, black curve, structures 1 and 2). In the oxidized PVBPT (($PVBPT^*)^+ BF_4^-$), we found a single broad peak at 2 θ = 21.75 ° (4.09 Å), which can be explained with the formation of π stacked structures. This π stacking of the phenothiazine moieties can only occur when the side chains are oxidized (Figure 53, red curve, structure 3). The planar, π stacked ring structures are very stable and cannot simple be separated again. For this reason, the segmental motion of the bulky moieties in the amorphous polymer matrix is restricted. Upon reducing, these stable structures would need to be destroyed again. As this structural rearrangement would need a lot of energy, only a partial reduction of the side chains takes place upon raster scanning the written patterns with an applied erasing bias V_E = -10 V. The remaining oxidized moieties still maintain a conducting state and are sufficient enough to provide the same conductivity as measured before the erasing step. We interpret that especially for PVBPT, the bulky moieties are hindered to interact with each other, since they have to rotate within the polymer matrix. After the oxidation, the original state can therefore not be restored applying a tip sample bias potential of -10 V. Thus, the conductive state is maintained.
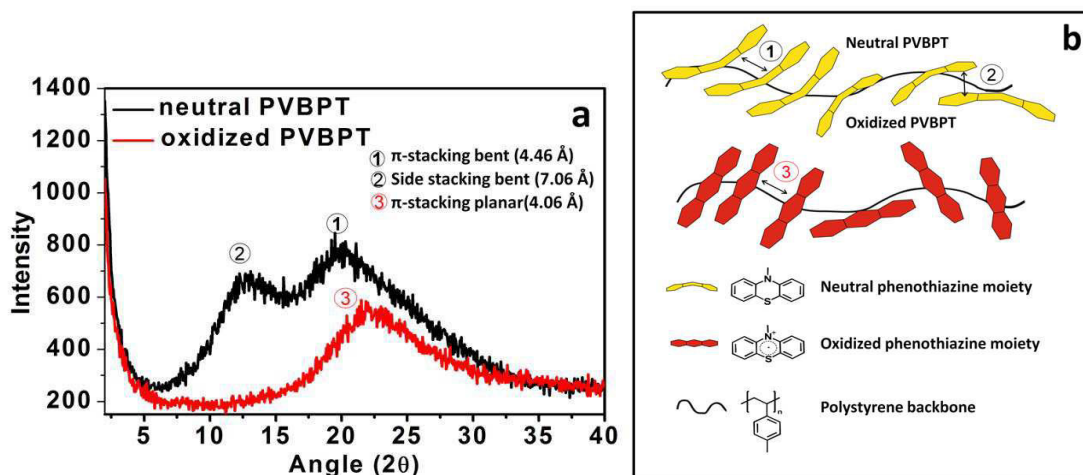
Figure 53: XRD data of neutral PVBPT and the oxidized PVBPT*+ BF4-. Data were recorded from powdered material. The peak positions are assigned to the formation of π-stacking (2) and side stacking (1) of the bent phenothiazine moieties for the neutral state and to the formation of π-stacking of the planar phenothiazine moieties in the oxidized state (3). b) Schematic overview of the PVBPT in the neutral and oxidized state indicating the stacking possibilities according to the XRD data [18]. Image is taken from [18]

We thus assume that the irreversibility of the patterning process arises from π-stacking, which cannot be reversed due to the low mobility of the polymeric chains. We investigated whether an increased mobility would allow erasing of patterns. To increase the mobility I used the heatable stage to heat the PVBPT films to 70 °C and 90 °C after the first successful patterning. At the elevated temperatures, I applied an erasing bias V_E of -10 V to the inner part of the patterned rectangular in order to reduce the PVBPT locally. Afterwards, I checked the conductivity again by imaging with V_R = -6 V. As in the erasing experiments at ambient conditions, no distinct decrease in conductivity was found for erasing neither at 70 °C nor at 90 °C.

7.4 Influence of temperature and humidity

As the PVBPT's phenothiazine moieties become charged during the oxidation, some counter ions have to be present in the oxidized state. As there are no potential counter ions provided by the PVBPT molecules themselves, we assume that water provides the required ions. Thus, patterning should not be possible in the absence of water. To investigate the influence of humidity the sample was heated using a heatable stage to 90 °C while flushing the whole microscope in a glove bag with dry nitrogen, in order to remove most of the water from the surface. Then a pattern was written and the success of the writing was investigated by imaging the area using V_R. The images of the patterning at 90 °C and

under dry nitrogen flushing in a glove bag, resulting in a relative humidity below 2% revealed no change in topography and only a very low difference (50 ± 80 fA) between the conductivity inside and outside the patterned area (Figure 54 middle). Instead of a homogenous patterned area like the one resulting from patterning at ambient conditions, only very few single pathways formed.
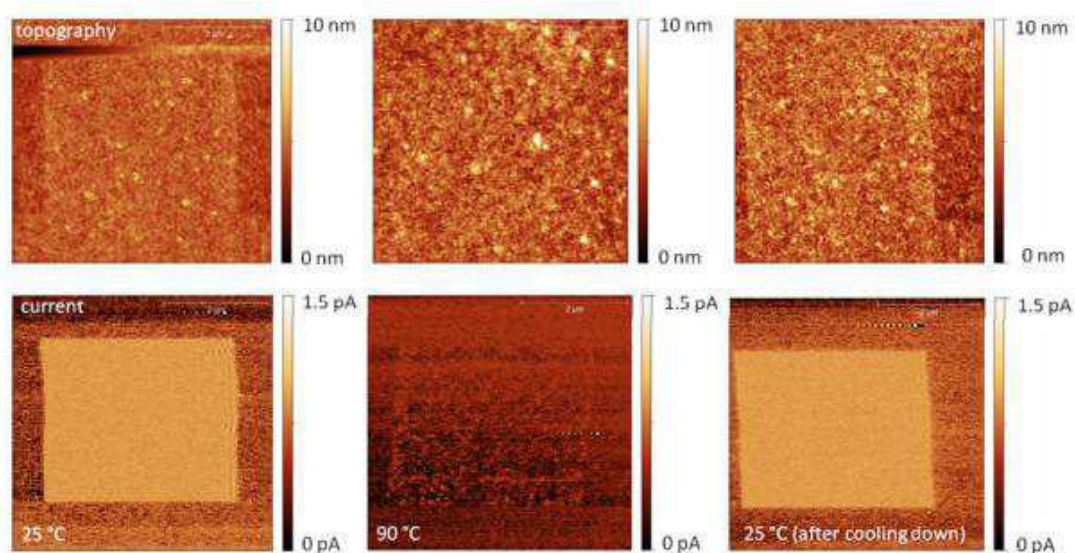

Figure 54: Patterning experiments at different conditions. All patterns were written using V_W = +10 V, tip velocity of 0.3 µm/s and at room temperature. Read out was done using V_W = -6 V under ambient conditions. Left: Results from patterning at ambient conditions. Middle: Results of patterning after heating the sample to 90°C in dry nitrogen in a glove bag. The Patterning was done after cooling to room temperature but in dry nitrogen atmosphere. Right: Results from patterning at ambient conditions after opening the glove bag.

In order to make sure that neither tip nor sample were destroyed during the drying and the experiment, a control experiment was conducted before and after under ambient conditions. The topography and the current images recorded before the main experiments (Figure 54 left) showed that the patterning at ambient conditions was successful. There is only very little change in topography, but a clear contrast (500 ± 65 fA) in conductivity. The control experiment after the main experiment showed a slight increase in topography and distinct contrast in the current image (520 ± 75 fA) (Figure 54 right). The conductivity contrast resulting from both control experiments are almost identical, indicating that neither tip nor sample have changed their properties during the heating and drying. Under dry conditions no patterning was possible, thus we conclude, that the water meniscus forming around the tip and between tip and sample during the c-SPM experiment is a prerequisite for the oxidation of PVBPT. Most probably the water is needed to form counter ions for the formed charged PVBPT species.

7.5   Main findings

- Local patterning of PVBPT using c-SPM was demonstrated successfully. The SPM experiments showed that the synthesis of PVBPT was successful with respect to the materials abilities to be oxidized locally at voltages above + 6 V.

- The increase of conductivity in the patterned areas depended on the applied V_W and the tip velocity. Higher voltages and lower writing speed led to a higher increase in conductivity, because more phenothiazine groups were oxidized.

- The patterns were stable for at least 16 h, in agreement with macroscopic X-band ESR measurements. In addition, the PVBPT was quite stable towards nanomechanical wear, which is an important issue for SPM based storage or lithography processes.

- The presence of water was mandatory for successful patterning, because water provided the required counter ions

- The voltages needed for c-SPM patterning were higher than the voltages observed in cyclovoltametric measurements. Most probably, the higher bias was needed because of the high contact resistance arising from the small contact area between the conductive tip and the material. The thin film formed an isolating layer between the gold substrate and the tip, whereas in solution present ions led to a good conductivity between the electrodes.

- In solution both oxidation steps were fully reversible. In the thin films, oxidation was not reversible although erasing was tried with at V_E down to − 10 V. The irreversibility of the c-SPM oxidized PVBPT can be explained with π-stacking of the phenothiazine moieties which become planar upon oxidation. These planar rings form well-ordered structures which cannot be easily destroyed. In solution this ordering does not occur.

- The achieved On/Off ratio, which was the conductivity contrast between patterned and non-patterned areas reached only 5 to 10, which is low compared to other proposed polymeric materials like polyimides. This issue may be caused by the low molecular order within the polymer.

8.   Triggered shell rupture of polymeric nanocapsules

Reducing the length scale of materials, especially functional materials, arises the question, how such materials can be analyzed and how the results are related to macroscopical determined properties. One example for functional materials are capsules which can be triggered to release their content [83]. I wanted to investigate nanograms of capsules or even single capsules to compare the results from nanoscale experiments with macroscopic results. The comparison of macroscopic and nanoscale experiments allows to identify how time- and length scale of the experiment influence the measured values.

8.1   Introduction

State of the art

Capsules with a size of few 100 nm (nano-capsules) can, for example, deliver drugs through the blood or even through membranes to a target location in a living organism. Delivering the drugs only at this specific location, e.g. inside a cancer cell could help minimizing adverse reactions [141]. In self-healing materials, nanocapsules with triggered release option could react to an external stimulus in order to release agents which repair small damages of the material [83]. Fertilizers encapsulated in capsules with triggered release capability could be distributed on a field during winter, but will only be released when the soil temperature is high enough for the crops to sprout [83]. Thus, no fertilizer is washed away, which avoids contamination of lakes, rivers and ground water, and the fertilizer is exactly released, when the crop plant needs the nutrition. In all applications involving triggered release, the main idea is to release the encapsulated beneficial agents "just in time" or exactly at the wanted location. This allows the use of fewer agents and a precise control of the affected location both in place and time.

Regardless of the application, it is important to know exactly upon which level of stimulus the release is triggered. The release itself can be realized without destruction of the nanocapsule, e.g. by diffusion of the encapsulated substance through the capsules shell [142] or by destruction of the shell, either by decomposition of the shell's material [143, 144] or by structural degradation [141]. As the release mechanism is important for the time scale in which the content of the capsule is released, investigating this mechanism is of great interest. Release taking place via a weakening of the capsules shell, which then allows diffusion of the content, will be limited by the diffusion coefficient of the

content through the shell. For release taking place via shell destruction, the amount of destruction (total fragmentation or single rupture) will determine the rate at which the content leaks from the capsule. Of course, the trigger and the release mechanism are related and have to fit the desired application of the nanocapsule. Some examples for release mechanisms are UV induced degradation of a capsules shell, pH value controlled diffusion through the shell, or thermal decomposition of a gas generating agent in the shell, which results in an overpressure destroying the shell's structure [83]. Using a thermally triggered gas generator to destroy the capsules shell with pressure (Figure 55) was successfully demonstrated for microcapsules [145].
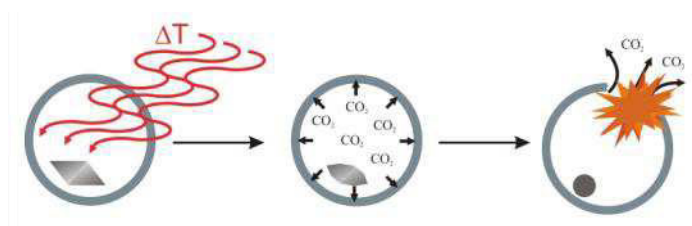
Figure 55: Schematic representation of the rupturing capsule caused by the gas generated during the decomposition of the gas generating agent

Goals of capsule analysis

For a scientist trying to use the same release approach using gas generators to induce a pressure which destroys the capsule's shell for nanocapsules (capsules with sizes below 1 µm), three questions have to be answered:

The first question is at which temperature the agent decomposes. The decomposition temperature can be determined by macroscopic TGA analysis of µg of the nanocapsules, but analyzing explosive materials can be dangerous for the analysis instrument and the scientist. Residues from the gas generator might lead to contamination of the instrument. Generally, for dangerous, very expensive or hard to prepare samples, reducing the amount of material needed for an analysis of the thermal properties is of interest. The second question is then, whether the pressure built up by the gas generator is sufficient to destroy the capsules shell. The third question is how exactly the generated pressure destroys the capsule's shell.

Capsule synthesis and analysis

The capsules and the incorporated gas generators were synthesized by Anika Hamberger and Katharina Landfester (MPIP Mainz). The capsules I worked with consisted of a polyurethane shell with

a diameter of ~500 nm and silver azide (AgN_3) as a gas generating agent. Silver azide is a primary explosive, which decomposes violently upon heating to 160 °C to 260 °C [81] forming metallic silver and gaseous nitrogen (Figure 56). The big range of measured decomposition temperatures is caused by impurities in silver azide crystallites, which have a big influence on the decomposition temperature.

$$2\,AgN_3 \xrightarrow{\Delta T} 2\,Ag \downarrow + 3\,N_2 \uparrow$$

Figure 56: Reaction equation of the silver azide decomposition. Silver azide decomposes upon between 160 °C and 260 °C [81] forming metallic silver and gaseous nitrogen.

The amount of silver azide needed to cause a rupture of this shell can be estimated by calculating how much silver azide needs to be decomposed in order to cause a pressure inside the capsule which exceeds the tensile strength of polyurethane. The tensile strength of polyurethane can range from 1 MPa to 69 MPa at break [146]. A pressure inside the nanocapsule of 70 MPa should therefore be sufficient to cause rupture of the shell. The amount of nitrogen needed to cause this pressure can be calculated solving the ideal gas equation or the van-der-Waals equation.

$$nRT = \left(p + \frac{n^2 a}{V^2} \right)\left(V - nb \right) \tag{Eq 29}$$

In (Eq 29), n is the number of molecules in the capsule, R is the universal gas constant, T the temperature, p the pressure, V the volume of the confinement, a is a measure for the attraction between molecules and b is the volume excluded by a mole of molecules. a and b are tabled values which can be gained from literature. However, using (Eq 29) can only provide a rough estimation as the results can only be qualitative and are by no means exact.

The average diameter of a capsule is 500 nm, the resulting capsule's volume V is then ~0.5 μm³. A pressure p = 70 MPa is needed to destroy the capsule. The temperature T will range between 300 K (Room temperature) and 530 K (upper decomposition temperature of silver azide) during the experiment. For nitrogen, a is 140 (kPa*dm⁶)/mol² and b is 0.0391 dm³/mol. Using these values to calculate n from (Eq 29) results in 80 fmol (femto mol) for a temperature of 300 K and in 56 fmol for a temperature of 530 K. From the reaction equation of the silver azide decomposition (Figure 56) we know, that we need 2 mol of silver azide to generate 3 mol of nitrogen. Therefore 2/3 of the calculated number of nitrogen molecules is the number of needed silver azide molecules. Combining this

number with the molecular weight of silver azide (150 g/mol) results in a mass of 5.6 pg to 8 pg (depending on the assumed temperature of the gas phase) of silver azide needed in one capsule to cause a shell rupture upon thermal decomposition. The exact decomposition temperature can be determined using thermogravimetrical analysis (TGA). In a TGA experiment, the sample mass is monitored, while the sample is heated. When reaching the decomposition temperature of the silver azide the gaseous N_2 is released, thus causing a mass loss. The resulting mass loss for one capsule during decomposition should be ~1.5 pg, calculated from the mass difference of 54 fmol silverazide before decomposition and the 54 fmol silver remaining afterwards. When analyzing few or even single capsules, the mass detection system has to be able to detect these picogram mass changes.

My approach to reduce the required sample mass was the use of micromechanical cantilevers as ultrasensitive balances [30]. In addition, micromechanical cantilevers with integrated joule heaters allow to heat samples in a controlled way [32, 147]. By monitoring the cantilever's resonant frequency upon heating, nanogram mass changes of the sample can be measured. Considering the expected mass change for a single capsule of 1.5 pg, 1000 capsules are enough sample material to cause a mass change in the nanogram regime which can be detected by monitoring the cantilever's resonant frequency. By monitoring the resonant frequency upon heating, the decomposition temperature can be determined as a sudden increase of resonant frequency (Figure 57 left).
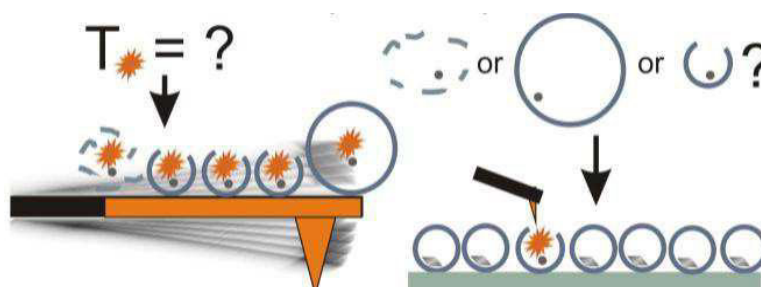
Figure 57: Left: Utilization of a heatable micromechanical cantilever as a nano thermogravimetric analysis instrument by measuring the change of resonant frequency during heating. Right: Using the heatable cantilever to probe the decomposition temperature of single capsules by recording its deflection upon heating. In addition I imaged single capsules before and after heating them locally with the same cantilever to clarify the release mechanism.

Placing single capsules on top of the cantilever is difficult, in addition, the mass loss caused by the decomposition of a single capsule might be too small to be detected using the vibrating cantilever as a balance. To investigate decomposition temperature of single capsules, thus further decreasing the amount of sample needed, I therefore analyzed single capsules using the heatable cantilever in

another SPM experiment. The tip was placed on top of a capsule and was heated. Upon reaching the silver azide's decomposition temperature nitrogen is generated which causes the capsule to inflate, to fragment or to rupture. Shell inflation, fragmentation or rupturing all lead to a change in the capsules size. By monitoring the deflection during the heating, the changes in capsules size, which happen at the decomposition temperature of silver azide can be detected (Figure 57 right). The decomposition temperature of the silver azide in the capsule is then determined as the temperature at which the capsules size changed.

The decomposition temperatures I determined with the two nanoscale experiments were compared with each other and with the temperature expected from literature to investigate how the small crystallite size and the nanoscale measurement influence the results. In addition, I imaged single capsules before and after heating them with the heatable tip. Comparing the recorded images allowed me to investigate the release mechanism (Figure 57 right).

8.2 Rupture temperature and rupture mechanism

8.2.1 Nano-thermogravimetric analysis

For the nano-thermogravimetric analysis (nano-TGA) experiment the resonant frequency of a heatable micromechanical cantilever was determined. A small amount of freeze dried samples was loaded on the cantilever and the resonant frequency was determined again. From the different resonant frequencies f_1 before and f_2 after loading, the mass change Δm of cantilever and thus the mass of the loaded capsules can be calculated:

$$\Delta m = \left(\frac{k}{4\pi} \right) \bullet \left(\frac{1}{f_1^2} - \frac{1}{f_2^2} \right)$$

(Eq 30)

Here, k is the spring constant of the used cantilever. The resonant frequency before f_1 loading was determined to be 79.848 ± 0.015 kHz. After loading, the resonant frequency f_2 was 69.684 ± 0.015 kHz. The spring constant of the used probe ranges between 0.5 and 3 N/m, so the loaded mass will range between 73 µg and 440 µg according to (Eq 30). Considering the calculations of the expected mass loss (> 1.5 pg per capsules) in this chapter's introduction (Eq 29) it is obvious, that enough capsules are on the probe to cause a clear shift of the resonant frequency upon thermal decomposition The calculation of the mass uptake shows the main source of uncertainty in this

approach: The mass determination depends strongly on the exact determination of the cantilevers spring constant. Usually, the spring constant is determined using the thermal tune method [43]. However, even when the spring constant is determined using thermal tune, there is a certain error in this value. For an exact mass loss, I would have to consider the change of the spring constant with the increasing temperature during the experiment. For the calculation of the total mass loss, the spring constant should be the same as the cantilever is cooled to room temperature after the experiment. For the determination of the decomposition temperature it is sufficient to determine the temperature at which an abrupt rise of the resonant frequency occurs. However, the spring constant can be removed from (Eq 31) by calculating relative mass changes as it is done in conventional TGA measurements. To determine the relative mass change *M[%]*, I used:

$$M[\%] = \frac{mass_T}{mass_{ini}} \bullet 100 = \frac{\left(\dfrac{k}{4\pi}\right) \bullet \left(\dfrac{1}{f_3^2} - \dfrac{1}{f_2^2}\right)}{\left(\dfrac{k}{4\pi}\right) \bullet \left(\dfrac{1}{f_1^2} - \dfrac{1}{f_2^2}\right)} \bullet 100 = \frac{\left(\dfrac{1}{f_3^2} - \dfrac{1}{f_2^2}\right)}{\left(\dfrac{1}{f_1^2} - \dfrac{1}{f_2^2}\right)} \bullet 100 \qquad \text{(Eq 31)}$$

The relative mass change *M[%]* is calculated as the quotient of the mass at a given temperature T *mass$_T$* and the initial mass *mass$_{Ini}$* multiplied by 100. The initial mass *mass$_{Ini}$* is calculated using the shift from resonant frequency before loading *f$_1$* to resonant frequency *f$_2$* after loading. The mass at the given temperature is calculated from the shift of resonant frequency at the given temperature *f$_3$* and *f$_2$*. For both mass calculations the spring constant *k* is used, which cancels out in the division. For this simple equation (Eq 31), I assumed that the spring constant is constant at all temperatures, which is certainly not the case. But again, for determination of the decomposition temperature I don't need absolute values for the mass change.

A record of the resonant frequency of a cantilever loaded with AgN$_3$ filled capsules upon increasing temperature shows a distinct increase of the resonant frequency at temperatures between 180 °C and 225 °C (Figure 58). Consequently, the calculated mass loss is about 80 % at temperatures between 180 °C and 225 °C. The observed range of decomposition temperatures between 180 °C and 225 °C is in agreement with literature giving a decomposition temperature for AgN$_3$ of 160 °C to 260 °C [81]. The slow mass loss above 225 °C is associated with the slow thermal decomposition of the polyurethane shell, which starts in this temperature range.
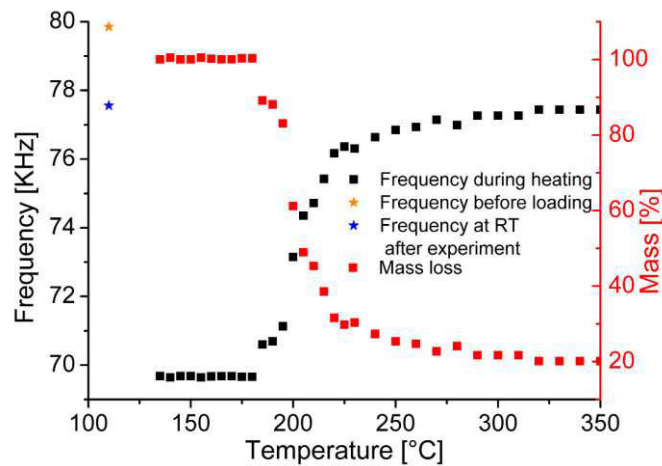
Figure 58: Frequency and calculated relative mass loss of a cantilever loaded with silver azide filled nanocapsules. The mass loss occurs over a broad temperature range and starts at~ 180°C.

The broad range of AgN$_3$ decomposition temperatures in literature is associated with impurities of AgN$_3$ crystallites. However, in my experimental setup another explanation for the broad distribution of decomposition temperature is an unequal temperature distribution on the cantilever. The capsules on the cantilever are not only placed only on the heater area but also next to it (Figure 59 left and middle).
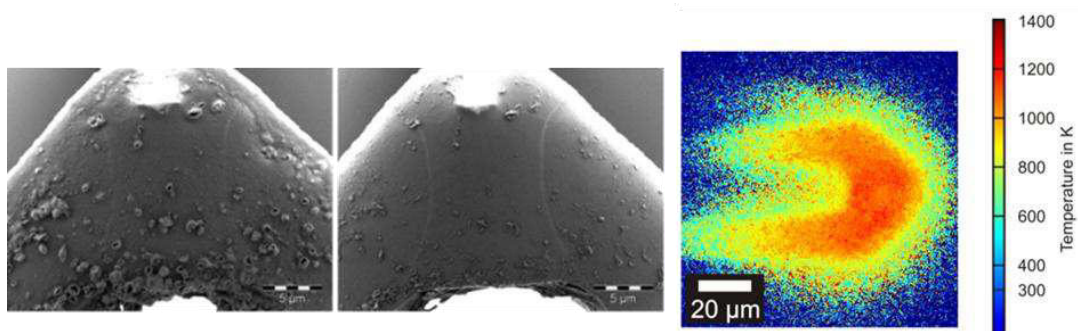
Figure 59: Left: SEM image of a cantilever loaded with nanocapsules before and after heating to 300°C for 5 minutes. Before heating, several capsules can be seen. Middle: After heating only little residue material is remaining. The trapeze shaped structure surrounded by thin white lines in the center of the cantilever is the less doped area which is joule heated by applying a voltage. Right: Image of the heat distribution of an operated heatable cantilever. The image was computed by taking images at different wavelength with single-photon camera and calculating the temperature using Planck's law [148]. Besides the temperature distribution in the cantilever, the heating of surrounding air is clearly visible.

To measure the temperature distribution on the cantilever, Ralf Kappes imaged them using a single photon camera at different wavelengths [148]. From the images taken at the different wavelength,

the temperature at each pixel can be calculated using Planck's law. The resulting temperature image (Figure 59 right) was recorded in air at the maximum applicable heating voltage of 10 V. The temperate image shows a reduction of temperature with the distance from the heater. Analyzing the temperature distribution revealed temperature differences of ~ 500 °C on the heater (Figure 60). The main reason for the huge differences is that the setup is not sensitive for the z-Position of each pixel, but just for temperature. Therefore, the heated air above the cantilever, which has a lower temperature than the cantilever, is included in the measurement. The measured distribution of temperatures on the heater area at a heating voltage of + 10 V is not equal to the distribution of temperature during the analysis of the capsules. For the capsule analysis, much lower temperatures were required, so the applied voltages were below 5 V.
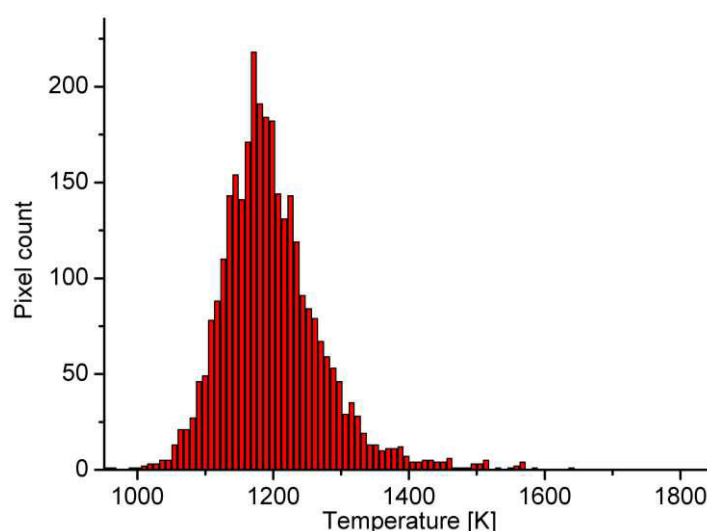
Figure 60: Distribution of the temperature on the heater area of the heatable probes from the temperature image (Figure 59 right). By applying a voltage of 10 V, most pixels corresponded to a temperature of 1200 K (930 °C). The temperatures measured on the heater ranged from 1000 K (730 °C) to 1500 K (1230 °C).

However, the thermal image of the probe shows that the temperature on the probe is not equal at all positions at a given heating voltage. Even for temperature distributions narrower than calculated from the temperature image at + 10 V heating voltage, capsules located at different positions can decompose at different applied voltages. For nano-TGA measurements, the finding of temperature disparity on the cantilever means, that the temperature measurements is always error-prone. The error depends on the temperature distribution on the cantilever.

To reduce the error in temperature measurement all sample material should be placed within as little area as possible and directly on the heater to avoid temperature differences arising from different

distances of capsules from the heater. Even on small areas considerable temperature differences may occur, so additional experiments should be performed in the future with samples having a well-defined decomposition temperature. Using a sample with well-defined decomposition temperature would allow investigating the influence of the temperature disparity. For example, for copper sulfate pentahydrate, could be used. Berger et. al. recorded nano-TGA curves of copper sulfate pentahydrate which showed mass losses due to dehydration occurring during a small temperature window [32].

The observed shift in resonant frequency, corresponding to a loss of material on the probe, was very distinct and indicated that in the expected temperature range ~80 % of the capsules mass were lost. As the achieved temperatures are below the decomposition temperature of polyurethane, I attribute the mass loss to an explosive decomposition of the silver azide, followed by an overpressure inside the capsule which violently flings the shells material from the vibrating probe. This assumption was strengthened by SEM images of a capsule loaded probe before and after heating to 300 °C. Before the heating several capsules could be seen. Afterwards only few residuals are found on the probe. The remaining material should be composed of metallic silver generated during the decomposition and remains of the polymeric shell.

In summary, the nano-TGA experiment in combination with the SEM images therefore gave the answer for two of the three questions I expressed in this chapters introduction: Silver azide filled polyurethane nanocapsules decompose at temperatures between 180 °C and 225 °C. A part of question three, how exactly the capsules decompose is answered, too. As there is a massive mass loss, and SEM images did not show any enlarged capsules after heating, it is safe to say, that the capsules are not inflated by the generated N_2.

8.2.2 Nano-thermal analysis

In order to clarify how exactly the capsule shell is destroyed by the N_2 formed during the decomposition of AgN_3 in the capsule and to analyze single capsules I used the heatable cantilever as a conventional SPM probe. I localized a single capsule, placed the probe on top of it and recorded the probes deflection during heating. The nano-thermal analysis (nTA) was performed in vacuum, in order to avoid heat transfer through the air from the probe to the capsule. Instead of measuring the mass of the capsules during heating like before, nTA measures the height of a capsule during heating. I recorded deflections curves on different capsules while heating the tip (Figure 61). In the beginning, the deflection curves on all capsules increased due to thermal expansion with almost the same slope which was recorded for heating a cantilever of the same type on bare silicon (Figure 61, black curve).

At the decomposition temperature, the capsule's size changed, because of the shell getting ruptured by the generated internal pressure. As I already excluded inflation of the capsules upon the silver azide decomposition, I expected a sudden decrease of capsules size upon decomposition, which was observed.
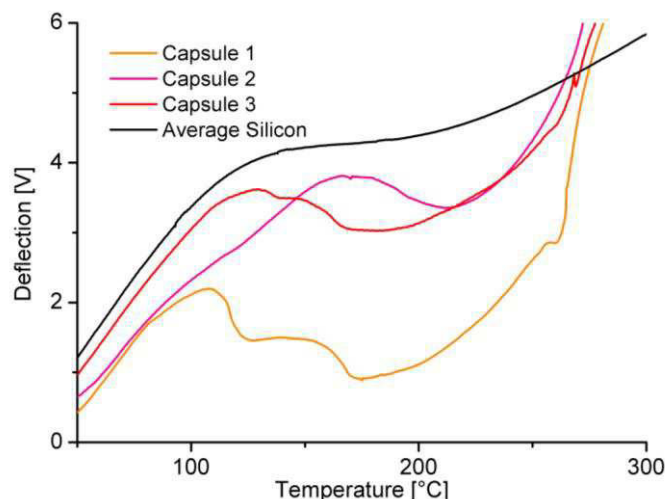

Figure 61: Deflection recorded on three different capsules during heating. For comparison, the deflection signal measured on bare silicon is again plotted (chapter 4). Please note that the capsules were measured with the same cantilever, while the silicon curve was recorded using a different one. Capsule 1 showed a first decreases at 110 °C and a second decrease at 150 °C. Capsule 2 showed a broad and slow decrease at 170 °C. Capsule 3 had again two decreases at 130 °C and at 150 °C. The slopes of the deflection curves on the capsules are in the beginning almost the same as the slope recorded on silicon. After the decreases, the slopes of the curves recorded on the capsules are much steeper.

Capsule 1 showed a first decrease in deflection at 110 °C and a second decrease at 150 °C. Afterwards, the deflection increased steadily but with a higher slope than observed on bare silicon (Figure 61). Almost the same behavior was observed for capsule 3. Here the two decreases took place at 130 °C and at 150 °C. Capsule 3 showed the same behavior in the beginning but had only one broad decrease at 170 °C before the steep increase was observed. For all three capsules, the increase observed at the end was much steeper than the one recorded on silicon.

The main difference between the nTA (Figure 61) and the discussed nano-TGA (Figure 58) results is that nTA revealed two different decomposition temperatures. My own nano-TGA measurements and the literature state that the silver azide decomposes between 160 °C and 260 °C. Therefore, only the second decrease of deflection on capsule 1 and 3 at 150 °C and the decrease of deflection on capsule 2 at 170 °C can be explained with the silver azide decomposition.

The first decrease, which was not observed in the nano-TGA measurements, can be explained by the different sample preparations used for the experiments. For the nano-TGA experiment I used freeze dried capsules, which can be placed on the probe using a micromanipulator. For the nTA experiment, I used the capsules directly from solution. Although they were dried by air blowing and the experiment was performed in vacuum, the capsules investigated with nTA might still contain water and cyclohexane. This different capsule preparation can be the reason for the observed first deflection decrease for capsule 1 and 3 at 110 °C and 130 °C respectively. At these temperatures residual water and cyclohexene could be removed from the capsule causing shrinkage. As the capsules used for nano-TGA were freeze dried, no water or cyclohexane was present, thus no signal was observed before AgN_3 decomposition.

The differences in measured decomposition temperatures can be caused by the tip's position on the capsule. I calculated the temperature from the applied heating voltage, thus the recorded temperature is the temperature of the tip and not the temperature reached at the silver azide. Different distances between the tip and the silver azide in the capsule cause the measurement of different decomposition temperatures. However, the measured temperatures are at the lower limit or even below the broad range of reported decomposition temperatures. An explanation based on the silver azide properties can be offered recalling that on a macroscopic scale silver azide is known to explode upon touching it. If the same is true for the small crystallites in the capsules, then the pressure induced by the expanding probe could be sufficient to initiate the decomposition, which then could start at temperatures below the expected 160 ° to 180 °C.

The steeper slope measured on capsules compared to the slope measured on silicon can be explained analogous to chapter 4. Polymer and silicon have different thermal expansion coefficients. Polyurethane expands more than silicon, thus a steeper slope is observed. Also, the polymer acts as a thermal isolation layer leading to higher temperatures in the tip and the cantilever, thus more bending of the cantilever is expected. The steeper slope therefore showed that the tip was still resting on the remains of the capsules shell.

In order to clarify the release mechanism, I recorded images of the capsules before and after the nTA. The recorded images showed a single rupture on each of the three investigated capsules (Figure 62). All capsules were ruptured at a sharp corner (on the left of the capsule in Figure 62 a and f, on the down side on Figure 62 d). It is obvious that all ruptures occurred horizontal, parallel to the probes long axis. One explanation is that at elevated temperature, the tip penetrates the capsules shell, because of the force generated by expanding. The polyurethane becomes softer at elevated

temperature. The combination of increasing force and softening of the shell allows the probe to sink into the capsule. This penetration into the upper shell caused the observed first decrease of deflection. Due to the resulting lower resting position the pressure beneath the probes tip is reduced. Upon further thermal expansion the pressure increases causing the probe to penetrate the bottom shell as well, causing the second decrease of deflection. However, the steep slopes after the deflection decreases observed in the nTA experiments indicate, that still some polyurethane has to be present beneath the tip.
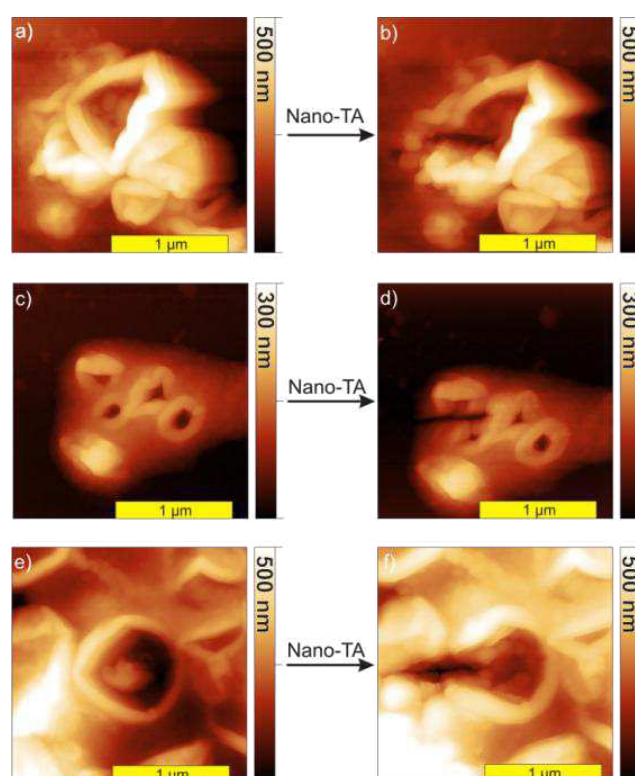
Figure 62: Three nano capsules before and after the nano-TA experiment. The shells did not explode but exhibit a single rupture at their weakest point. On the image in e) the silver crystallite in the capsule can be seen. The observed rupture can be caused by either the pressure generated by the silver azide decomposition or by the probes tip penetrating the capsules shell at elevated temperatures.

Assuming that the observed ruptures (dark marks in Figure 62) are caused by the tip explains the different temperatures measured with the two techniques. They are different, because they are related to different mechanisms. Nano-TGA probed the thermal decomposition of silver azide (180 °C – 225 °C) and nTA probed the softening temperature of polyurethane (110 °C – 170 °C) under the applied pressure. When the tip already caused a rupture of the capsule, then the decomposition of

silver azide cannot cause any additional damage, as the generated gas is easily released from the ruptured capsule.

Tip induced rupture of the capsules during the nTA experiment would also explain why the capsules are still present after the experiment. When looking at the SEM image of the capsule loaded probe (Figure 59) after heating the probe to 300 °C, almost no capsules were left. However, at temperatures above 225 °C, the polyurethane itself starts to decompose. In the nano-TGA experiment this temperature was applied to the whole capsule via the heated cantilever. In the nTA experiment, the heat was distributed only to a very small area via the tip. Therefore, complete decomposition of the shell is more likely for the nano-TGA experiment than for the nTA experiment.

8.3 Main findings

- Nano-TGA experiments with freeze dried polyurethane capsules containing silver azide showed decomposition temperatures of silver azide between 180 °C and 225 °C. These temperatures were in the expected range, so no time- or length scale effects were observed

- SEM images of the cantilever before and after the nano-TGA revealed that almost all capsules were destroyed or even removed completely. This was explained by violent shell rupture caused by the generated N_2 or by thermal decomposition of the polyurethane shell.

- Investigations of the heatable probe itself showed that the temperature distribution on the probe is not equal. The temperature scaled with the distance from the heater zone. On the heater zone there were comparably large fluctuations in the temperature (up to 20% difference at~1000 °C). The temperature disparity on the cantilever limits the precision of the nano-TGA method.

- Using the heatable probes for the nTA of single capsules dropcoated from solution revealed two temperatures at which the deflection changed, one between 110 °C and 130 °C and one between 150 °C and 170 °C. Only two of the three investigated capsules showed signals at both temperatures.

- Two different models can explain the nTA results. In model one, the first decrease was caused by evaporation of water and cyclohexane. The second decrease was caused by a collapse of the shell due to pressure induced rupture by the generated N_2. In model two, the first

decrease was caused by the hot tip penetrating the top shell of the capsule due to increasing force and softening of polyurethane. The second decrease would then be attributed to the tip penetrating the bottom shell. However, the steep slope of the nTA curves after the second deflection decrease indicated the presence of remaining polyurethane beneath the tip.

- SPM images of the nTA investigated capsules were recorded before and after the thermal analysis. All three images showed a single shell rupture which was parallel to the long axis of the used probe. The rupture in direction of the expanding cantilever indicated, that the shell rupture was caused by model 2, thus the deflection decreases observed with nTA are caused by the tip penetrating the polyurethane shell.

9.   Conclusion and Outlook

Within my thesis I investigated polymers at micro-second time and nanometer size scales using scanning probe methods. With heatable probes, the thermomechanical properties of polymers become accessible at microsecond time and nanometer size scales.

Due to the better heat conductivity of inorganic substrates (e.g. λ_{Si} = 150 W·m^{-1}·K^{-1}, λ_{Au} = 314 W·m^{-1}·K^{-1}) compared to polystyrene (λ_{PS} = 0.17 W·m^{-1}·K^{-1}), the influence of the substrate on heat dissipation increases with decreasing film thicknesses. This has tremendous impact on analysing thin polymers as the temperature in the film will drastically reduce with distance from the heated probe. Thermomechanical measurements on thin ppNb films on top of thick PS showed that the temperature at the ppNb-PS interface is only 50% to 70% of the probe's temperature. For thin films on top of good heat conductors this thermal gradient is even steeper. Thus the heat conductivity in the underlying substrate contributes significantly to the thermal gradient and the temperature reached in thin polymer films.

Temperature-deflection curves recorded on thick polymer films show a distinct signal when the tip sinks into the polymer. Thus, the softening temperature of the polymer can be determined. For thick polymer samples, deflection signals in the order of several 100 nm are obtained. However, the signal decreases with film thickness due to the limited distance that the tip can travel into the polymer. Additional changes in deflections caused by expanding and bending of the cantilever and expanding substrate are independent of the film thickness. For thin films, signals caused by cantilever and substrate overlay the small signals caused by the polymer. In order to study thermomechanical effects on thin films, I improved the conventional nTA analysis by subtracting the signals caused by cantilever and substrate. This novel approach extends the film thicknesses suitable for nTA analysis to films as thin as 60 nm. Furthermore, by subtracting the background more signals in the TD curves could be identified: glass transition, the rubber plateau and the further softening of PS at the end of the rubber plateau. With little more experimental time, more precise and more detailed analysis is possible with the improved approach.

Even for films as thin as 35 nm, the tip does not penetrate through the film during temperature deflection measurements. Thus, even for such thin films, the experiment should probe the thermomechanical properties of the polymer and not of the substrate. However, in thin polymer films with thicknesses in the range of the polymer's radius of gyration, single polymer chains are probed

instead of huge ensembles of chains. Single chains cannot be compressed or yielded in the same way as the bulk material. Therefore, for films with lateral length scales in the size of the polymer's radius of gyration, experiments based on deforming the material will fail.

In the future, the fast temperature transport through thin polymer films to a good heat conducting substrate could also be used for film thickness determination: The probe is heated with a constant voltage to a temperature expected to be well below any softening temperature of the polymer. Then the surface is raster scanned in a usual contact mode experiment while the resistivity of the probes heater is recorded, like for thermal imaging of the local heat conductivity. For a homogenous material, the recorded resistivity should then be directly related to the film's thickness at each position.

As the heat applied to a thin film is dissipated in the substrate, the tip temperature needed for manipulation depends on the film's thickness. The effective heat sink provided by the substrate is here of advantage as it allows high lateral resolution: The heat is preferably dissipated in the better heat conducting substrate and not laterally in the film so the formed structures can be in the size of the used SPM tip. Thus, I tried to pattern conductive structures into a thin polymer film by inducing a reaction in the precursor film. The tip temperature is limited by two factors: First, the temperature at which reaction takes place must be reached at the film substrate interface. Second, the tip must not exceed the softening or sublimation temperature of the formed product to avoid destruction of the formed structures. These prerequisites limit both the film thickness, and thus the height of achievable structures, and the choice of potential materials. Only precursors which react at temperatures well below the softening or sublimation temperature of the desired product can be used.

I investigated, 13,6-N-Sulfinylacetamidopentacene forming pentacene upon heating, met both requirements. The patterning led to a decreased film thickness due to the decomposition and an increased conductivity in the patterns due to the formation of pentacene. However, the removal of the precursor leaving freestanding structures was not successful. In all experiments both precursor and pentacene were removed, which can be explained in two ways. First, the temperature reached at the precursor substrate interface was not high enough to cause decomposition. Thus a thin layer of precursor remained between formed pentacene and substrate. This precursor layer was dissolved during washing, so the formed pentacene floated away. Second, the adhesion between pentacene and precursor was not strong enough to prevent washing away.

Consequently, in order to make sure, that the complete film reacts, I propose to heat the substrate to a temperature slight below the decomposition temperature in future. Thus, the temperature drop at the precursor-substrate interface is smaller and the decomposition temperature should be reached. I already conducted some pre-experiments showing that heating the precursor film to 100 °C can be done without causing decomposition at the timescale of patterning.

For nano-thermal lithography, the conclusion is that the substrate should have the same thermal conductivity as the precursor film in order to avoid substrate cooling effects, although this might lead to larger structures due to heat distribution in the film. Therefore, several different substrates should be used in future; especially substrates which are less heat conducting and promise better adhesion two pentacene. Polymers with T_G or T_M above the decomposition temperature of the precursor could be promising candidates.

In addition to be patterned at high velocities on a very small length scale, storage media must be stable against nanoscale wear. I developed a new approach to combine easily indentable bulk properties with wear resistive surface properties: Bilayered stacks. The sublayer governs the indentation properties and the protection layer governs the wear resistivity. Bilayers have the great advantage that storage layer and protection layer can be optimized for their specific requirements independently. The wear resistive layer can be used for other applications like microelectronic mechanical systems (MEMS), which require a wear resistive surface without altering the bulk properties of a material as well. The medium I designed consisted of a soft polystyrene sublayer a wear resistive protection layer consisting of plasma polymerized norbornene. I found that the wear resistivity of the ppNb layers depended strongly on the substrate. The different behavior of ppNb layers on top of different substrates can be explained with different wear mechanisms

The protection layer has not only to be wear resistive itself but also needs a strong bonding to the sublayer. Using plasma deposition, this bonding can be achieved by increasing plasma power and plasma time in order to generate more radicals which directly react with the surface. However, this "harsher" plasma conditions lead to an increased sputtering of the surface, thus the interfacial roughness is increased. For thermomechanical data storage we demonstrated that such plasma polymerized layers add the needed resistivity towards nanoscale wear to the sublayer, while still allowing the indentation of this sublayer.

The thickness of the protection layer is the important length scale in this system, as the temperature transport to the sublayer is important for the indentation properties. Even thin ppNb layers of 6.5 nm

thickness increased the temperature of the probe needed to soften the PS sublayer. Comparing indentation experiments on bulk PS, bulk ppNb and the stacks revealed a temperature gradient of 50% to 70% within 10 nm of the ppNb layer. However, we showed that the indentation process itself was completely governed by the PS. The protection layer only shielded part of the applied force and temperature, thus shifting the required force and temperature towards higher values but not influencing the indentation behavior.

The short contact times of 10 µs in the indentation experiments led to an increase of the measured softening temperature of PS compared to macroscopic experiments. Instead of the expected glass transition at 100 °C or the end of the rubber plateau at 150 °C to 160 °C we measured a softening temperature of 221°C The shift can be explained by time-temperature superposition. For faster thermomechanical data storage systems this implies an upper limit in writing speed: Decreasing contact time between probe and medium leads to higher required probe temperatures for indentation. Upon further reducing the contact time, the required temperature will eventually exceed the maximum temperature of the probe. The maximum temperature of the probes is given by their resistance turnaround, the temperature at which the scaling of resistance with temperature changes from positive to negative. For the probes used here, the turnaround takes place at around 400 °C. Assuming a roughly linear scaling of the glass transition temperature with attempt frequencies at high frequencies (Figure 41), 400 °C would correspond to an attempt frequency of 700 kHz. 700 kHz would correspond to a contact time of 1.4 µs. Thus, high parallelization is needed for a thermomechanical SPM based data storage device to compete with conventional storage systems in the data transfer rates.

Another way to store data in a polymeric media is to locally change the conductivity of the polymer. For redox-active polymers like the PVBPT I investigated in my work, this change in conductivity can be induced by applying a voltage between tip and surface. The advantage of such a system is that the tip is not heated and pulled into the material which should allow faster writing speeds. The voltages needed for oxidation were higher than for macroscopic experiments. Due to the small contact area, the contact resistivity of the tip sample contact is higher than for both macroscopic measurements on films and measurements in solution. The same is true for the contact times which are much shorter in the SPM based patterning than in the macroscopic experiments. Another difference between the SPM based patterning and experiments in solution is the absence of an electrolyte. The electrons have to travel from the tip to the conducting substrate through a film, which is isolating before oxidation. Also, there is no direct source of counter ions present. Consequently, I found that water

needs to be present for successful patterning as it provides the required counter ions. Although the oxidation of the PVBPT should be reversible I was not able to demonstrate erasing on the thin films. We attributed this irreversibility of the oxidation with a structural rearrangement of the film which is not reversible in solid state.

Final concluding remarks

My work demonstrated how SPM can be used to investigate and change material properties at small length scales, short time scales or both. The results of such investigations as well as the conditions needed to change properties may well differ from the results or expectations gained from macroscopic experiments. Fascinatingly, many of the nanoscale results can well be explained with existing theories. Effects that don't have to be considered in macroscopic experiments, like the substrate's properties overlapping a film's properties, suddenly become prominent in nanoscopic experiments. As nanotechnologies are still an emerging field, identifying effects that influence nanoscale measurements, separating such effects from sample properties, the improvement of existing and development of new technologies for nanoscale analysis and manipulation will be a "hot topic" in the future.

10. Literature

1. Binnig, G., C.F. Quate, and C. Gerber, *Atomic Force Microscope.* Physical Review Letters, 1986. **56**(9): p. 930-933.

2. Nelson, B.A. and W.P. King, *Measuring material softening with nanoscale spatial resolution using heated silicon probes.* Rev. Sci. Instrum., 2007. **78**(2): p. 023702.

3. Pires, D., et al., *Direct write 3-dimensional nanopatterning using probes*. Vol. 7637. 2010: SPIE. 76371E.

4. Pires, D., et al., *Nanoscale Three-Dimensional Patterning of Molecular Resists by Scanning Probes.* Science, 2010. **328**(5979): p. 732-735.

5. Jaschke, M. and H.-J. Butt, *Deposition of Organic Material by the Tip of a Scanning Force Microscope.* LANGMUIR, 1995. **11**(4): p. 1061-1064.

6. Chung, S., et al., *Temperature-dependence of ink transport during thermal dip-pen nanolithography.* Applied Physics Letters, 2011. **99**(19): p. 193101-3.

7. Mamin, H., et al., *High-density data storage based on the atomic force microscope.* Proceedings of the IEEE, 1999. **87**(6): p. 1014-1027.

8. Bhushan, B., ed. *Springer Handbook of Nano-technology*. 2nd ed. 2007, Springer: Berlin, Heidelberg, New York.

9. Bhushan, B., *Nanotribology and nanomechanics of AFM probe-based data recording technology.* Journal of Physics: Condensed Matter, 2008. **20**(36): p. 365207.

10. Jo, A., et al., *Ultrahigh-density phase-change data storage without the use of heating.* Nat Nano, 2009. **4**(11): p. 727-731.

11. Vettiger, P., et al., *The "Millipede" - More than one thousand tips for future AFM data storage.* IBM J. Res. Develop., 2000. **44**(3): p. 323-340.

12. Vettiger, P., et al., *The "Millipede" - nanotechnology entering data storage.* Nanotechnology, IEEE Transactions on, 2002. **1**(1): p. 39-55.

13. Binnig, G., et al., *Ultrahigh-density atomic force microscopy data storage with erase capability.* Applied Physics Letters, 1999. **74**(9): p. 1329-1331.

14. Cho, Y., et al., *Realization of 10 Tbit/in² memory density and subnanosecond domain switching time in ferroelectric data storage.* Applied Physics Letters, 2005. **87**(23).

15. Cho, Y., S. Kazuta, and K. Matsuura, *Scanning nonlinear dielectric microscopy with nanometer resolution.* Applied Physics Letters, 1999. **75**(18): p. 2833-2835.

16.   Cho, Y., et al., *Tbit/in² ferroelectric data storage based on scanning nonlinear dielectric microscopy.* Applied Physics Letters, 2002. **81**(23): p. 4401-4403.

17.   Ono, T., S. Yoshida, and M. Esashi, *Electrical modification of a conductive polymer using a scanning probe microscope.* Nanotechnology, 2003. **14**(9).

18.   Golriz, A.A., et al., *Redox active polymers with phenothiazine moieties for nanoscale patterning via conductive scanning force microscopy.* Nanoscale, 2011. **3**(12).

19.   Yoshida, S., et al., *Reversible electrical modification on conductive polymer for proximity probe data storage.* Nanotechnology, 2005. **16**(11).

20.   Lea, A.S., et al., *Manipulation of proteins on mica by atomic force microscopy.* LANGMUIR, 1992. **8**(1): p. 68-73.

21.   Hamada, E. and R. Kaneko, *Micro-tribological evaluations of a polymer surface by atomic force microscopes.* Ultramicroscopy, 1992. **42–44, Part 1**(0): p. 184-190.

22.   Berger, R., et al., *Nanowear on Polymer Films of Different Architecture.* Langmuir, 2007. **23**(6): p. 3150-3156.

23.   Elkaakour, Z., et al., *Bundle Formation of Polymers with an Atomic Force Microscope in Contract Mode: A Friction Versus Peeling Process.* Physical Review Letters, 1994. **73**(24): p. 3231-3234.

24.   Leung, O.M. and M.C. Goh, *Orientational Ordering of Polymers by Atomic Force Microscope Tip-Surface Interaction.* Science, 1992. **255**(5040): p. 64-66.

25.   Schmidt, R.H., G. Haugstad, and W.L. Gladfelter, *Scan-induced patterning and the glass transition in polymer films: Temperature and rate dependence of plastic deformation at the nanometer length scale.* LANGMUIR, 2003. **19**(24): p. 10390-10398.

26.   Altebaeumer, T., et al., *Self-similarity and finite-size effects in nano-indentation of highly cross-linked polymers.* Nanotechnology, 2008. **19**(47).

27.   Altebaeumer, T., et al., *Nanoscale Shape-Memory Function in Highly Cross-Linked Polymers.* Nano Letters, 2008. **8**(12): p. 4398-4403.

28.   Gotsmann, B., et al., *Exploiting chemical switching in a Diels-Alder polymer for nanoscale probe lithography and data storage.* ADVANCED FUNCTIONAL MATERIALS, 2006. **16**(11): p. 1499-1505.

29.   Duvigneau, J., H. Schönherr, and G.J. Vancso, *Nanoscale Thermal AFM of Polymers: Transient Heat Flow Effects.* ACS Nano, 2010. **4**(11): p. 6932-6940.

30.   Boisen, A. and et al., *Cantilever-like micromechanical sensors.* Reports on Progress in Physics, 2011. **74**(3): p. 036101.

31.   Boonliang, B. and et al., *A focused-ion-beam-fabricated micro-paddle resonator for mass detection.* Journal of Micromechanics and Microengineering, 2008. **18**(1): p. 015021.

32.   Berger, R., et al., *Micromechanical thermogravimetry.* Chemical Physics Letters, 1998. **294**: p. 363-369.

33.   Garcia, R. and R. Perez, *Dynamic atomic force microscopy methods.* Surface Science Report, 2002. **47**: p. 197-301.

34.   Fumagalli, L., et al., *Probing Electrical Transport Properties at the Nanoscale by Current-Sensing Atomic Force Microscopy*, in *Applied Scanning Probe Methods VIII*, B. Bhushan, H. Fuchs, and M. Tomitori, Editors. 2008, Springer Berlin Heidelberg. p. 421-450.

35.   Berger, R., et al., *Electrical Modes in Scanning Probe Microscopy.* Macromolecular Rapid Communications, 2009. **30**(14): p. 1167-1178.

36.   Haeberle, W., M. Pantea, and J.K.H. Hoerber, *Nanometer-scale heat-conductivity measurements on biological samples.* Ultramicroscopy, 2006. **106**(8–9): p. 678-686.

37.   Giessibl, F.J., *Atomic Resolution of the Silicon (111)-(7x7) Surface by Atomic Force Microscopy.* Science, 1995. **267**(5194): p. 68-71.

38.   Jarvis, S.P., J.E. Sader, and T. Fukuma, *Frequency Modulation Atomic Force Microscopy in Liquids*, in *Applied Scanning Probe Methods VIII*, B. Bhushan, H. Fuchs, and M. Tomitori, Editors. 2008, Springer Berlin Heidelberg. p. 315-350.

39.   Butt, H.-J., B. Cappella, and M. Kappl, *Force measurements with the atomic force microscope: Technique, interpretation and applications.* Surface Science Reports, 2005. **59**(1-6): p. 1-152.

40.   Bloo, M.L., H. Haitjema, and W.O. Pril, *Deformation and wear of pyramidal, silicon-nitride AFM tips scanning micrometre-size features in contact mode.* Measurement, 1999. **25**(3): p. 203-211.

41.   Blackman, G.S., L. Lin, and R.R. Matheson, *Micro- and Nano-Wear of Polymeric Materials*, in *Microstructure and Microtribology of Polymer Surfaces*1999, American Chemical Society. p. 258-269.

42.   Martin, Y., C.C. Williams, and H.K. Wickramasinghe, *Atomic force microscope - force mapping and profiling on a sub 100-Å scale.* Journal of Applied Physics, 1987. **61**(10): p. 4723-4729.

43.   Hutter, J.L. and J. Bechhoefer, *Calibration of atomic-force microscope tips.* Review of Scientific Instruments, 1993. **64**(7): p. 1868-1873.

44.   Hertz, H., Journal für Reine und Angewandte Mathematik, 1882. **92**: p. 156.

45.   Johnson, K.L., K. Kendall, and A.D. Roberts, *Surface Energy and the Contact of Elastic Solids.* Proceedings of the Royal Society of London. Series A, Mathematical and Physical Sciences, 1971. **324**(1558): p. 301-313.

46.   Derjaguin, B.V., V.M. Muller, and Y.P. Toporov, *Effect of contact deformations on the adhesion of particles.* Journal of Colloid and Interface Science, 1975. **53**(2): p. 314-326.

47. Meyers, G.F., B.M. DeKoven, and J.T. Seitz, *Is the molecular surface of polystyrene really glassy?* LANGMUIR, 1992. **8**(9): p. 2330-2335.

48. Woodland, D.D. and W.N. Unertl, *Initial wear in nanometer-scale contacts on polystyrene.* Wear, 1997. **203–204**(0): p. 685-691.

49. Schmidt, R.H., G. Haugstad, and W.L. Gladfelter, *Correlation of Nanowear Patterns to Viscoelastic Response in a Thin Polystyrene Melt.* LANGMUIR, 1998. **15**(2): p. 317-321.

50. Sills, S. and R.M. Overney, *Creeping Friction Dynamics and Molecular Dissipation Mechanisms in Glassy Polymers.* Physical Review Letters, 2003. **91**(9): p. 095501.

51. Jing, J., et al., *An atomic force microscopy study of polyester surfaces.* Journal of Materials Science, 1995. **30**(22): p. 5700-5704.

52. Iwata, F., T. Matsumoto, and A. Sasaki, *Local elasticity imaging of nano bundle structure of polycarbonate surface using atomic force microscopy.* Nanotechnology, 2000. **11**(1): p. 10-15.

53. Kaneko, R. and E. Hamada, *Microwear processes of polymer surfaces.* Wear, 1993. **162–164, Part A**(0): p. 370-377.

54. Khurshudov, A. and K. Kato, *Volume increase phenomena in reciprocal scratching of polycarbonate studied by atomic force microscopy.* Journal of Vacuum Science & Technology B: Microelectronics and Nanometer Structures, 1995. **13**(5): p. 1938-1944.

55. Schmidt, R.H., G. Haugstad, and W.L. Gladfelter, *Scan-Induced Patterning in Glassy Polymer Films: Using Scanning Force Microscopy To Study Plastic Deformation at the Nanometer Length Scale.* LANGMUIR, 2003. **19**(3): p. 898-909.

56. King, W.P., et al., *Nanoscale Thermal Analysis of an Energetic Material.* Nano Letters, 2006. **6**(9): p. 2145-2149.

57. Somnath, S., E.A. Corbin, and W.P. King, *Improved Nanotopography Sensing via Temperature Control of a Heated Atomic Force Microscope Cantilever.* Sensors Journal, IEEE, 2011. **11**(11): p. 2664-2670.

58. Chui, B.W., et al., *Low-stiffness silicon cantilevers with integrated heaters and piezoresistive sensors for high-density AFM thermomechanical data storage.* Microelectromechanical Systems, Journal of, 1998. **7**(1): p. 69-78.

59. Murrell, M.P., et al., *Spatially resolved electrical measurements of SiO[sub 2] gate oxides using atomic force microscopy.* Applied Physics Letters, 1993. **62**(7): p. 786-788.

60. Dai, H., E.W. Wong, and C.M. Lieber, *Probing Electrical Transport in Nanomaterials: Conductivity of Individual Carbon Nanotubes.* Science, 1996. **272**(5261): p. 523-526.

61. Oyaizu, K., et al., *Redox-active polyimide/carbon nanocomposite electrodes for reversible charge storage at negative potentials: expanding the functional horizon of polyimides.* Journal of Materials Chemistry, 2010. **20**(26).

62.   Yasuda, H., *Glow discharge polymerization.* Journal of Polymer Science: Macromolecular Reviews, 1981. **16**(1): p. 199-293.

63.   Hansen, R.H. and H. Schonhorn, *A new technique for preparing low surface energy polymers for adhesive bonding.* Journal of Polymer Science Part B: Polymer Letters, 1966. **4**(3): p. 203-209.

64.   Klages, C.P., et al., *Deposition and properties of carbon-based amorphous protective coatings.* Surface and Coatings Technology, 1996. **80**(1-2): p. 121-128.

65.   Chifen, A.N., et al., *Adhesion improvement of plasma-polymerized maleic anhydride films on gold using HMDSO/O-2 adhesion layers.* Plasma Processes and Polymers, 2007. **4**(9): p. 815-822.

66.   Zajíčková, L., et al., *Deposition of protective coatings in rf organosilicon discharges.* Plasma Sources Science and Technology, 2007. **16**(1): p. S123.

67.   Yamamoto, T., et al., *Improvement on Hydrophilic and Hydrophobic Properties of Glass Surface Treated by Nonthermal Plasma Induced by Silent Corona Discharge.* Plasma Chemistry and Plasma Processing, 2004. **24**(1): p. 1-12.

68.   Samanta, K.K. and et al., *Atmospheric pressure plasma polymerization of 1,3-butadiene for hydrophobic finishing of textile substrates.* Journal of Physics: Conference Series, 2010. **208**(1): p. 012098.

69.   Lin, Y. and H. Yasuda, *Effect of plasma polymer deposition methods on copper corrosion protection.* Journal of Applied Polymer Science, 1996. **60**(4): p. 543-555.

70.   Kudoyarova, V.K., et al., *Study of diamond-like carbon films for protective coatings.* Surface and Coatings Technology, 1998. **100-101**: p. 192-195.

71.   Moser, E.M., et al., *Hydrocarbon films inhibit oxygen permeation through plastic packaging material.* Thin Solid Films, 1998. **317**(1-2): p. 388-392.

72.   Favre-Quattropani, L., et al., *The protection of metallic archaeological objects using plasma polymer coatings.* Surface and Coatings Technology, 2000. **125**(1-3): p. 377-382.

73.   Norrman, K., A. Ghanbari-Siahkali, and N.B. Larsen, *6 Studies of spin-coated polymer films.* Annual Reports Section "C" (Physical Chemistry), 2005. **101**: p. 174-201.

74.   Zhang, Y., et al., *Interface roughness of plasma deposited polymer layers.* Journal of Colloid and Interface Science, 2010. **In Press, Corrected Proof**.

75.   Förch, R., Z. Zhang, and W. Knoll, *Soft Plasma Treated Surfaces: Tailoring of Structure and Properties for Biomaterial Applications.* Plasma Processes and Polymers, 2005. **2**(5): p. 351-372.

76.   Chu, L.-Q., W. Knoll, and R. Förch, *Stabilization of Plasma-Polymerized Allylamine Films by Ethanol Extraction.* LANGMUIR, 2006. **22**(13): p. 5548-5551.

77.   *MSDS of norbornene, 99%*, 2007, Acros organic.

78.   Beake, B.D., G.J. Leggett, and M.R. Alexander, *Scanning force microscopy of plasma polymerised hexane: information on the mechanical properties of thin films from tip-induced wear.* Polymer, 2001. **42**(6): p. 2647-2653.

79.   Dinelli, F., G.J. Leggett, and M.R. Alexander, *Nanowear in scanning force microscopy: Information on deposits formed in and downstream of a hexane plasma.* Journal of Applied Physics, 2002. **91**(6): p. 3841-3846.

80.   Crespy, D., et al., *Polymeric Nanoreactors for Hydrophilic Reagents Synthesized by Interfacial Polycondensation on Miniemulsion Droplets.* Macromolecules, 2007. **40**(9): p. 3122-3135.

81.   Bartlett, B.E., F.C. Tompkins, and D.A. Young, *The Decomposition of Silver Azide.* Proceedings of the Royal Society of London, Series A: Mathematical and Physical Sciences, 1958. **246**(1245): p. 206-216.

82.   Hamberger, A., in *Dissertation in der Fakultät Naturwissenschaften* 2011, Ulm University: Ulm.

83.   Esser-Kahn, A.P., et al., *Triggered Release from Polymer Capsules.* Macromolecules, 2011. **44**(14): p. 5539-5553.

84.   Yow, H.N. and A.F. Routh, *Formation of liquid core-polymer shell microcapsules.* Soft Matter, 2006. **2**(11): p. 940-949.

85.   Parratt, L.G., *Surface Studies of Solids by Total Reflection of X-Rays.* Physical Review, 1954. **95**(2): p. 359.

86.   Nevot, L. and P. Croce, *Characterization of surfaces by grazing X-Ray reflection - Application to study of polisging of some silicate - glasses.* Revue De Physique Appliquee, 1980. **15**(3): p. 761-779.

87.   Li, Y., et al., *Contact Angle of Water on Polystyrene Thin Films: Effects of CO2 Environment and Film Thickness.* LANGMUIR, 2007. **23**(19): p. 9785-9793.

88.   Berron, B.J., P.A. Payne, and G.K. Jennings, *Sulfonation of Surface-Initiated Polynorbornene Films.* Industrial & Engineering Chemistry Research, 2008. **47**(20): p. 7707-7714.

89.   Gedde, U.W., *Polymer physics* 1996 London [u.a.] Chapman & Hall

90.   Konishi, T., et al., *Mean-square radius of gyration of oligo- and polystyrenes in dilute solutions.* Macromolecules, 1990. **23**(1): p. 290-297.

91.   Zeng, H., et al., *Adhesion and Friction of Polystyrene Surfaces around Tg.* Macromolecules, 2006. **39**(6): p. 2350-2363.

92.   Kaliappan, S.K. and B. Cappella, *Temperature dependent elastic–plastic behaviour of polystyrene studied using AFM force–distance curves.* Polymer, 2005. **46**(25): p. 11416-11423.

93. Domke, J. and M. Radmacher, *Measuring the Elastic Properties of Thin Polymer Films with the Atomic Force Microscope.* LANGMUIR, 1998. **14**(12): p. 3320-3325.

94. Afzali, A., C.D. Dimitrakopoulos, and T.L. Breen, *High-Performance, Solution-Processed Organic Thin Film Transistors from a Novel Pentacene Precursor.* Journal of the American Chemical Society, 2002. **124**(30): p. 8812-8813.

95. Sigma-Aldrich. *13,6-N-Sulfinylacetamidopentacene*. 2012 [cited 2012 09.05.2012]; Description of 13,6-N-Sulfinylacetamidopentacene]. Available from: http://www.sigmaaldrich.com/catalog/product/aldrich/666025?lang=de&region=DE.

96. García, R. and A. San Paulo, *Attractive and repulsive tip-sample interaction regimes in tapping-mode atomic force microscopy.* Physical Review B, 1999. **60**(7): p. 4961-4967.

97. Rosa, L.G. and J. Liang, *Atomic force microscope nanolithography: dip-pen, nanoshaving, nanografting, tapping mode, electrochemical and thermal nanolithography.* Journal of Physics: Condensed Matter, 2009. **21**(48): p. 483001.

98. Wiesmann, D., et al., *Multi Tbit/in² Storage Densities with Thermomechanical Probes.* Nano Letters, 2009. **9**(9): p. 3171-3176.

99. Krim, J., *Resource Letter: FMMLS-1: Friction at macroscopic and microscopic length scales.* American Journal of Physics, 2002. **70**(9): p. 890-897.

100. Bhushan, B., J.N. Israelachvili, and U. Landman, *Nanotribology: friction, wear and lubrication at the atomic scale.* Nature, 1995. **374**(6523): p. 607-616.

101. Eleftheriou, E., *IBM Zurich Research Laboratory Probe Storage Millipede*, 2012, IBM Zurich Research Laboratory: Zurich. p. Website of the Millipede project.

102. Farshchi-Tabrizia, M., et al., *Influence of Humidity on Adhesion: An Atomic Force Microscope Study.* Journal of Adhesion Science and Technology, 2008. **22**: p. 181-203.

103. Surtchev, M. and e. al., *The initial stages of the wearing process of thin polystyrene films studied by atomic force microscopy.* Nanotechnology, 2005. **16**(8).

104. Gotsmann, B. and U. Dürig, *Thermally Activated Nanowear Modes of a Polymer Surface Induced by a Heated Tip.* LANGMUIR, 2004. **20**(4): p. 1495-1500.

105. Gotsmann, B., et al., *Controlling Nanowear in a Polymer by Confining Segmental Relaxation.* Nano Letters, 2006. **6**(2): p. 296-300.

106. Gotsmann, B., et al., *Designing Polymers to Enable Nanoscale Thermomechanical Data Storage.* Advanced Functional Materials, 2010. **20**(8): p. 1276-1284.

107. Dongfeng, D. and K. Koji, *Interface yield map of a hard coating under sliding contact.* Thin Solid Films, 1994. **245**(1-2): p. 115-121.

108. Knoll, A., et al., *Relaxation Kinetics of Nanoscale Indents in a Polymer Glass.* Physical Review Letters, 2009. **102**(11): p. 117801.

109. Aoike, T., et al., *Comparison of Macro- and Nanotribological Behavior with Surface Plastic Deformation of Polystyrene.* Langmuir, 2001. **17**(7): p. 2153-2159.

110. Fu, J., B. Li, and Y. Han, *Molecular motions of different scales at thin polystyrene film surface by lateral force microscopy.* The Journal of Chemical Physics, 2005. **123**(6): p. 064713.

111. Dinelli, F., G.J. Leggett, and P.H. Shipway, *Nanowear of polystyrene surfaces: molecular entanglement and bundle formation.* Nanotechnology, 2005. **16**(6).

112. Esteruelas, M.A., et al., *Thermal properties of polynorbornene (cis- and trans-) and hydrogenated polynorbornene.* Polymer Bulletin, 2007. **58**(5): p. 923-931.

113. Rui, M., et al., *Recent Progress in the Vinylic Polymerization and Copolymerization of Norbornene Catalyzed by Transition Metal Catalysts.* Polymer Reviews, 2009. **49**(3): p. 249-287.

114. Mindlin, R.D. and H. Deresiewicz, *Elastic spheres in contact under varying oblique forces.* Journal of Applied Mechanics-Transactions of the Asme, 1953. **20**(3): p. 327-344.

115. Breakspear, S., et al., *Friction coefficient mapping using the atomic force microscope.* Surface and Interface Analysis, 2004. **36**(9): p. 1330-1334.

116. Bickford, M.E. and W.C. Hall, *Collateral projections of predorsal bundle cells of the superior colliculus in the rat.* Journal of Comparative Neurology, 1989. **283**(1): p. 86-106.

117. Schallamach, A., *How does rubber slide?* Wear, 1971. **17**(4): p. 301-312.

118. Pozidis, H., et al., *Demonstration of thermomechanical recording at 641 Gbit/in(2).* Ieee Transactions on Magnetics, 2004. **40**(4): p. 2531-2536.

119. Sze, S.M. and K.K. Ng, *Physics of Semiconductor Devices*. Physics of Semiconductor Devices2006: John Wiley & Sons, Inc.

120. Gotsmann, B., et al., *Nanoprobes*, in *Nanotechnology*, H. Fuchs, Editor 2009, VCH: Weinheim. p. 121-169.

121. Robertson, R.E., *Theory for the Plasticity of Glassy Polymers.* The Journal of Chemical Physics, 1966. **44**(10): p. 3950-3956.

122. Rottler, J. and M.O. Robbins, *Shear yielding of amorphous glassy solids: Effect of temperature and strain rate.* Physical Review E, 2003. **68**(1): p. 011507.

123. Johnson, K.L., *Contact mechanics* 1. paperback ed1994 Cambridge {[u.a.]: Cambridge Univ. Press. XI, 452 S.

124. Czichos, H. and H. Akademischer Verein, *Die Grundlagen der Ingenieurwissenschaften mit 337 Tabellen*2000, Berlin; Heidelberg; New York; Barcelona; Hongkong; London; Mailand; Paris; Singapur; Tokio: Springer.

125. Ferry, J.D., *Viscoelastic properties of polymers* 1980 New York: Wiley.

126.   Doi, M. and S.F. Edwards, *The theory of polymer dynamics* 1986, Oxford: Clarendon Press.

127.   Rubinstein, M. and R.H. Colby, *Polymer physics* 2003 Oxford; New York: Oxford University Press.

128.   Knoll, A., et al., *Probe Based Surface Modification of Polymers Below 30 nm Pitch.* Journal of Nanoscience and Nanotechnology, 2010. **10**: p. 4538-4542.

129.   Ling, Q.-D., et al., *Polymer electronic memories: Materials, devices and mechanisms.* Progress in Polymer Science, 2008. **33**(10): p. 917-978.

130.   Sackett, P.H. and R.L. McCreery, *Effect of structure on phenothiazine cation radical reactions in aqueous buffers.* Journal of Medicinal Chemistry, 1979. **22**(12): p. 1447-1453.

131.   Morishima, Y., Y. Itoh, and A. Koyagi, *Electrochemical electron-transfer process of polymers containing N-methylphenothiazine.* Journal of Polymer Science: Polymer Chemistry Edition, 1983. **21**(4): p. 953-960.

132.   Morishima, Y., I. Akihara, and S.-I. Nozakura, *Electrical conductivity of partially oxidized poly(3-vinyl-10-methylphenothiazine) films.* Journal of Polymer Science: Polymer Letters Edition, 1985. **23**(12): p. 651-653.

133.   Majumdar, A., et al., *Nanometer-scale lithography using the atomic force microscope.* Applied Physics Letters, 1992. **61**(19): p. 2293-2295.

134.   Xie, X.N., et al., *Water-Bridge-Assisted Ionic Conduction in Probe-Induced Conical Polymer Pattern Formation.* Advanced Materials, 2005. **17**(11): p. 1386-1390.

135.   Huang, C., G. Jiang, and R. Advincula, *Electrochemical Cross-Linking and Patterning of Nanostructured Polyelectrolyte–Carbazole Precursor Ultrathin Films.* Macromolecules, 2008. **41**(13): p. 4661-4670.

136.   Morishima, Y., et al., *Electron transport in poly(3-vinyl-10-methylphenothiazine) films.* Macromolecules, 1987. **20**(5): p. 978-983.

137.   Morishima, Y., I. Akihara, and N. Shun-Ichi, *Electrical Conductivity of Partially Oxidized Poly(3-vinyl-10-methylphenothiazine) Films.* Journal of Polymer Science: Polymer Letters Edition, 1985. **23**: p. 3.

138.   Uchida, T., M. Ito, and K. Kozawa, *Crystal-structure and related properties of Phenothiazine cation radical Hexachloroantimonate - Monoclinic (I) form.* Bulletin of the Chemical Society of Japan, 1983. **56**(2): p. 577-582.

139.   Zhou, Z., *Phenothiazine, thiazolium and sulfonic acid functionalized hybrid materials and their applications in electronics, optics and catalysis*, 2009, Technische Universität Kaiserslautern.

140.   Sailer, M., *Elektronische Kommunikation auf molekularer Ebene: Aufbau und Untersuchung höherer Phenothiazin-Oligomere und -Polymere*, 2006, Ruprecht-Karls-Universität.

141.   De Geest, B.G., et al., *Self-exploding capsules.* Polymer Chemistry, 2010. **1**(2): p. 137-148.

142. Dowding, P.J., et al., *Oil Core-Polymer Shell Microcapsules Prepared by Internal Phase Separation from Emulsion Droplets. I. Characterization and Release Rates for Microcapsules with Polystyrene Shells.* Langmuir, 2004. **20**(26): p. 11374-11379.

143. Nuyken, O., J. Dauth, and W. Pekruhn, *Thermosensitive microcapsules, II. New azomonomers, homo- and cocondensation, microencapsulation, release measurements, size distribution and thermo-printing.* Die Angewandte Makromolekulare Chemie, 1991. **190**(1): p. 81-98.

144. Rosenbauer, E.M., et al., *Controlled Release from Polyurethane Nanocapsules via pH-, UV-Light- or Temperature-Induced Stimuli.* Macromolecules, 2010. **43**(11): p. 5083-5093.

145. E. Mathiowitz, et al., *Photochemical rupture of microcapsules: A model system.* Journal of Applied Polymer Science, 1981. **26**(3): p. 809-822.

146. eFunda, I. *Polyurethane.* [cited 2012 24.08.2012]; Available from: http://www.efunda.com/materials/polymers/properties/polymer_datasheet.cfm?MajorID=PU&MinorID=1.

147. Lee, J., *Microthermogravimetry using a microcantilever hot plate with integrated temperature-compensated piezoresistive strain sensors.* Rev. Sci. Instrum., 2008. **79**(5): p. 054901.

148. Kappes, R.S. and et al., *Time-resolved, local temperature measurements during pulsed laser heating.* New Journal of Physics, 2010. **12**(8): p. 083011.

11.   Acknowledgments

At the end of three years of scientific work ending with this thesis, there are of course numerous people, whom I would like to thank for their contribution

My Doktorvater **Prof. Hans-Jürgen Butt** gave valuable input and brought up a lot of interesting questions which extended the scope of the work. As a chemist, I'm especially grateful for your help with the topic of polymer physics. Also, I want to thank you for the freedom in research I had under your supervision.

The most important contributor was my direct supervisor **Dr. Rüdiger Berger**. From Rüdiger I always got a lot of constructive feedback, not only on the direct scientific work, but also on talks, posters and papers. The german saying "Nicht für die Schule sondern für das Leben lernen wir" came absolutely true in the lunch breaks, where you and your fellow project leaders provided me with a lot of insight in topics like raising children, buying houses or gardening.

I want to thank **Prof. Angelika Kühnle** for being my second supervisor. Thanks for your valuable input to my work and for the supervision of my "Lehrschein" in physical chemistry.

A big thank-you goes to my cooperation partners from IBM, **Dr. Armin Knoll**, **Dr. Bernd Gotsmann** and **Dr. Urs Dürig**, especially for the nanoindentation experiments with the Millipede setup. For good and fruitful cooperation on redox active polymers for SPM based patterning I am very grateful to **Prof. Jochen Gutmann** and **Ali Golriz** and our Japanese colleagues from the group of **Prof. Ono,** as well as **Dr. Masaya Toda** and **Prof. Akiko Itakura.** For the cooperation on the analysis of nanocapsules my thanks go to **Anika Hamberger** and **Prof. Katharina Landfester**.

For all help with plasma polymerization and in the plasma laboratory, I want to thank **Dr. Renate Förch, Jennifer Kroth, Mark Bedrich, Alexander Lotz** and **Sascha Pihan,** who helped me getting started.

Without a lot of technical support from **Uwe Rietzler**, **Helma Burg**, **Maren Müller** and **Andreas Best** my work would have been much harder. Thanks for all the help and also for the warm and friendly atmosphere in our office. And thanks, **Uwe**, for all the stories about the fun of having children!

My work on analyzing thin polymer films was greatly supported by two summer internship students from Thailand, **Weerin Chanteroj** and **Nitchan Piromsawat** whom I want to thank for recording and analyzing thousands of force-distance curves.

For proof-reading, commenting and correcting I'll be grateful for ever to **Prof. Yvonne Joseph**, **Esha Sengupta**, **Rabea Keller** and **Daniela Fell.**

Numerous people made it a pleasure for me to come to the institute every day: **Maria Untch, Esha Sengupta, Huong Thi Nguyen, Anna Domanski, Stefan Weber, Dominik Pilat, Thomas Nick, Marcin Makowski, Tomas Corrales, Ralf Kappes, Marjan Zakerin, Rabea Keller, Daniela Fell, Jennifer Wenzl, Tim Still** and **all the other colleagues** from the coffee corner. Sorry to all persons I possibly forgot to mention by name and thanks for three wonderful years!

Last but not least I want to thank my parents **Brigitte and Giselher Kaule** and my **grandmother Dorothea Schmid** for all the support they gave me during my studies. Finally, I want to thank **Monika Scharf** for a long list of things, which would exceed the scope of the acknowledgment.

12.   Curriculum Vitae and Publications

Franz Albert Giselher <u>Tassilo</u> Kaule

Date of birth: April 30th, 1982

Place of birth: Stuttgart, Germany

Nationality: German

Dissertation

06/2009 – 11/2012

PhD thesis "Polymer surfaces on small length- and short time-scales" at the Max Planck Institute for Polymer Research in the group of Prof. Dr. Hans-Jürgen Butt (Project leader: Rüdiger Berger)

Diploma thesis

12/2008 – 05/2009

Diploma thesis "Direct liquefaction of coal" at the Institute for Technical Chemistry, University Stuttgart in the group of Prof. Dr. Jens Weitkamp (Supervision PD Dr. Yvonne Traa)

Study

10/2001 – 05/2009

Study of "Chemistry" at the University Stuttgart. Major fields of study: Technical and Physical chemistry. Degree obtained "Diplom Chemie", grade "Sehr gut"

School Education

1992 -2000

Karlsgymnasium Stuttgart, Germany. Degree obtained "Abitur", grade: 1.4 ("sehr gut")

Publications in reviewed journals

- A. A. Golriz, **T.   Kaule**, J. Heller, M. B. Untch, P. Schattling, P. Theato, M. Toda, S. Yoshida, T. Ono, H.-J. Butt, J. S. Gutmann, R. Berger, „Redox active polymers with phenothiazine moieties for nanoscale patterning via conductive scanning force microscopy", *Nanoscale,* 2011, accepted. DOI: 10.1039/c1nr10917k

- **T. Kaule**, S. Pihan, S. G. J. Emmerling, Y. Zhang, R. Förch. J. S. Gutmann, H.-J. Butt, R. Berger, D. Pires, A. Knoll, B. Gotsmann, U. T. Dürig, „Influence of hyper-thin wear protection layers on nano-mechanical properties", *ACS Nano*, submitted

- **T. Kaule**, S. Pihan, S. G. J. Emmerling, Y. Zhang, R. Förch. J. S. Gutmann, H.-J. Butt, R. Berger, D. Pires, A. Knoll, B. Gotsmann, U. T. Dürig, „The mechanical stability of plasma deposited protection layers made from norbornene", in preparation

- **T. Kaule**, A. Hamberger, Y. Zhang, K. Landfester, H.-J. Butt, R. Berger, „Thermal properties of nanocapsules measured by scanning force microscopy methods", *MEE, 97, 223-226, 2011*, DOI: 10.1016/j.mee.2012.03.011

- Y. Zhang, J. Arfsten, S.A. Pihan, **T. Kaule,** R. Förch, R. Berger, „Interface roughness of plasma deposited polymer layers", *JCIS,* 351, 2, 532-536, *2010.* DOI: 10.1016/j.jcis.2010.07.051

- A. A. Golriz, **T. Kaule**, M. B. Untch, R. Berger, J.S. Gutmann, "Nanowear stable redox active polymer brushes with phenothiazine moieties", in preparation

Poster presentations at international conferences

- **T. Kaule**, S. Pihan, S. G. J. Emmerling, Y. Zhang, R. Förch. J. S. Gutmann, H.-J. Butt, R. Berger, D. Pires, A. Knoll, B. Gotsmann, U. T. Dürig, „Wear of thin polymer sandwich layers", *7th Zsigmondy Colloquium 2011,* (Poster 2)

- **T. Kaule**, S. Pihan, S. G. J. Emmerling, Y. Zhang, R. Förch. J. S. Gutmann, H.-J. Butt, R. Berger, D. Pires, A. Knoll, B. Gotsmann, U. T. Dürig, „Characterization of polymer media for high density scanning probe based data storage", *ISPAC 2010,* (P7)

- **T. Kaule**, S. Pihan, S. G. J. Emmerling, Y. Zhang, R. Förch. J. S. Gutmann, H.-J. Butt, R. Berger, D. Pires, A. Knoll, B. Gotsmann, U. T. Dürig, „Ultra-thin plasma polymerized films as protection layers for high-density data storage media", *Polychar18 2010*

Talks at international conferences

- **T. Kaule**, A. Hamberger, Y. Zhang, K. Landfester, H.-J. Butt, R. Berger, „Analysing Nanobombs for Potential Drug Release", *MNE 2011,* (O-MEMS-06)

- **T. Kaule**, S. Pihan, S. G. J. Emmerling, Y. Zhang, R. Förch. J. S. Gutmann, H.-J. Butt, R. Berger, D. Pires, A. Knoll, B. Gotsmann, U. T. Dürig, „Ultra-thin films as wear resistive coatings", *DPG Spring Meeting 2010,* (O 75.8)